Summer 2018

Functionalized nanoporous carbon scaffolds for hydrogen storage applications

Christopher L. Carr

Department: Physics

FUNCTIONALIZED NANOPOROUS CARBON SCAFFOLDS FOR HYDROGEN STORAGE APPLICATIONS

by

CHRISTOPHER LEE CARR

A DISSERTATION

Presented to the Faculty of the Graduate School of the

MISSOURI UNIVERSITY OF SCIENCE AND TECHNOLOGY

and

UNIVERSITY OF MISSOURI – ST. LOUIS

In Partial Fulfillment of the Requirements for the Degree

DOCTOR OF PHILOSOPHY

in

PHYSICS

2018

Approved
Eric H. Majzoub, Advisor
Alexey Yamilov, Co-Advisor
Philip Fraundorf
Stephen M. Holmes
Julia E. Medvedeva

DISSERTATION PUBLICATION OPTION

A portion of this dissertation has been prepared in publication format.

Paper I, Pages: 32-64, "Surface-Functionalized Nanoporous Carbons for Kinetically Stabilized Complex Hydrides through Lewis Acid-Lewis Base Chemistry" Carr C. L.; Majzoub, E. H. has been published previously: *J. Phys. Chem. C,* 2016, *120*, 11426-11432.

Paper II, Pages: 65-101, "Anomalous H_2 Desorption Rate of $NaAlH_4$ Confined in Nitrogen-Doped Nanoporous Carbon Frameworks" Carr C. L.; Jayawardana, W.; Zou, H.; White, J. L.; El Gabaly, F.; Conradi, M. S.; Stavila, V.; Allendorf, M. D.; Majzoub, E. H. has been accepted for publication in the journal *Chemistry of Materials*: DOI: 10.1021/acs.chemmater.8b00305

ABSTRACT

Recent efforts have demonstrated confinement in porous scaffolds at the nanoscale can alter the hydrogen sorption properties of metal hydrides, though not to an extent feasible for use in onboard hydrogen storage applications, proposing the need for a method allowing further modifications. The work presented here explores how the functionalization of nanoporous carbon scaffold surfaces with heteroatoms can modify the hydrogen sorption properties of confined metal hydrides in relation to non-functionalized scaffolds (FS). Investigations of nanoconfined $LiBH_4$ and $NaAlH_4$ indicate functionalizing the carbon scaffold surface with nitrogen can shift the activation energy of hydrogen desorption in excess of 20 kJ/mol from the activation energy decrease of ≥ 40 kJ/mol obtained from confinement in non-FS. XPS measurements indicate a significant fraction of the nitrogen contained in the carbon scaffolds is pyridinic, suggesting interactions of the available lone electron pair with the confined hydride and decomposition products strongly influences the hydrogen sorption processes. TPD experiments demonstrate nitrogen-FS can stabilize the release of diborane by ~30 °C, and kinetically stabilize $LiBH_4$ against decomposition to higher temperatures. Increased reorientational activation energies measured for the systems with nitrogen-FS using quasielastic neutron scattering support the observed stabilization of $LiBH_4$ is connected with the surface chemistry of the scaffold. Peak rates of hydrogen release occur at higher temperature from $NaAlH_4$ in nitrogen-FS despite the lower measured activation energy, indicating the existence of a rate-limiting step that may be related to the level of scaffold nitrogen doping and the onset of $NaAlH_4$ melting.

ACKNOWLEDGMENTS

Completion of this dissertation represents the culmination of my work over the last ten years since deciding to pursue the study of science. Along the way there have been countless individuals that have provided their assistance and shared insights that have aided me during my time as a student. Dr. Eric Majzoub has been instrumental in my development as a scientist, for which I am grateful. Having a dedicated advisor always available to offer assistance, encouragement, and share their knowledge as a respected scientist made a difficult endeavor much easier to see through to the finish. I would like to express my thanks to the members of my committee, Dr. Philip Fraundorf, Dr. Stephen Holmes, Dr. Julia Medvedeva, and Dr. Alexey Yamilov for taking their time to not only serve on the committee, but also share unique perspectives about the work. This work would not have been possible without the generous financial support I have received at different times along the way from the NASA Missouri Space Grant Consortium, the NSF IGERT fellowship administered through the University of Missouri in Columbia, and a dissertation fellowship from the University of Missouri St. Louis Graduate School that was integral to completion of this dissertation.

During my tenure as a graduate student I have had the pleasure to work with an outstanding group of people and as a result develop many friendships. In particular, the machine shop lunch crew consisting of Bruce Burkeen, Jerry Bennett, and Joe Kramer always provided me with a laugh and needed distractions. Bruce was an exceptional machinist, and I thank him for dedicating hours of his time to fabricate numerous components I utilized in this work. Additionally, I always enjoyed the spirited morning conversations about anything and everything with Alice Canavan, Dr. Ricardo Flores, Dr. David Osborne, and Joe Kramer.

Last and most importantly I express my love and gratitude to my wife Jessica, for always supporting me throughout our last 16 years together, and my daughter Carah who along this journey brought and continues to bring immense joy into my life. Thank you both for your patience, understanding, and sacrifices.

TABLE OF CONTENTS

LIST OF ILLUSTRATIONS

LIST OF TABLES

1. INTRODUCTION

1.1. A CLEAN ENERGY ECONOMY FOR THE FUTURE

At present the majority of the world's energy market is dominated by sources derived from traditional fossil fuels such as petroleum, coal and natural gas, which accounted for approximately 85% of the total energy supplied globally in 2015 [1]. The demand for energy is predicted to increase by 30%, despite gains in energy efficiency, due to emerging world economies and population growth [1]. In the face of climate change, environmental concerns, and the decline of easily accessible fossil fuel reserves much attention has been focused on developing an alternative renewable energy economy [2-5]. Unfortunately renewable energy technologies capable of generating substantial energy, such as solar arrays and wind farms, suffer from their intermittent nature leading to difficulties associated with matching output to grid demand. In turn, grid power management is often complicated by incorporation of these renewable arrays. The main issue stems from the inability to effectively store the energy produced by the renewable arrays for later use. Proper storage could eliminate intermittence concerns by storing excess energy provided at times of peak operation for use during low output periods, resulting in a more constant power supply over time. Many methods exist to store energy, including batteries, super capacitors, flywheels, and hydrogen storage. Of these options using hydrogen produced from renewable sources as a key energy carrier together with electricity has the potential to provide a clean energy economy for the future by eliminating the environmental impact of the energy sector.

1.2. USING HYDROGEN AS AN ENERGY CARRIER

The suitability of hydrogen (H_2) as an energy carrier is the result of two properties, that is a high specific energy density per unit mass in relation to other fuels and an oxidation process whereby environmentally benign water is the only byproduct produced. Thus, hydrogen has the potential to be a zero carbon emission fuel if it can be produced locally using renewable energy resources [2]. Currently, the largest roadblock to the realization of a vibrant hydrogen economy is the lack of a method to adequately

store hydrogen for energy applications. Though many different forms of hydrogen storage exist, none has been able to meet the requirements set forth by the U.S. Department of Energy (DOE) [6].

The following subsections provide a brief introduction to some of the different hydrogen generation and storage methods currently being investigated as viable options for use in a hydrogen based energy economy. Though hydrogen can be produced from fossil fuels, here we consider only renewable generation methods. In addition, the final subsection provides a more in depth discussion detailing the advantages and challenges of using complex metal hydrides in hydrogen storage applications, which is the focus of this work.

1.2.1. Hydrogen Generation Methods. Hydrogen can mainly be produced from three sources: water, biomass and fossil fuels. Production of hydrogen from fossil fuels is not considered a viable method for a clean hydrogen energy economy due to the non-renewable nature of fossil fuels and generation of CO_2 as a byproduct during processing. In this introduction we consider only methods capable of generating green hydrogen from biomass and water. Naturally, production methods utilizing water as the hydrogen source would be most advantageous considering the readily available supply of water on earth, which covers approximately 70% of the earth's surface.

In order to extract hydrogen gas from water energy must be supplied to the compound. The energy needed for this process can be supplied from an array of renewable energy sources such as solar arrays, wind farms, hydroelectric, geothermal, ocean tides, and ocean currents. Additionally, waste heat from industrial processes and nuclear energy can be utilized in green hydrogen production. Each energy source can be leveraged in a variety of ways to produce hydrogen from water and/or biomass.

Generated electrical energy can be used directly in electrolysis, where electrical energy is supplied to liquid water to produce hydrogen and oxygen [3]:

$$H_2O_{(\ell)} \rightarrow H_{2(g)} + \frac{1}{2}O_{2(g)} \qquad \Delta V = -1.23\ V \tag{1}$$

The overall process shown in eq.1 is the result of oxidation and reduction reactions occurring at the respective electrodes. A variety of electrolysers are currently available based on the different types of electrolyte employed to facilitate the necessary conduction of ions between the electrodes, including polymer electrolyte membrane, alkaline for low temperature electrolysis (LTE), and solid oxide electrolysers used in high temperature electrolysis (HTE) [5,7,8].

Thermal energy generated by nuclear reactions, focused solar energy, geothermal, and industrial waste heat can facilitate hydrogen generation through the process of thermolysis, where water thermally dissociates into hydrogen and oxygen. In this process water is heated into steam at high temperatures in excess of 2500 K to achieve reasonable dissociation [7]. Hybrid processes exist that use both thermal and electrical energy together in the hydrogen generation process. One example is high temperature electrolysis where thermal energy is used to heat water to a high temperature steam, followed by dissociation of the gaseous water via the electrolysis process. Electrolysis efficiency increases with temperature resulting in a lower electrical energy requirement than low temperature electrolysis [3,8]. In this process all the components of the electrolyser cell must be able to operate and withstand the elevated temperatures of the heated steam. In practice the biggest challenges associated with this process have stemmed from finding materials that can adequately resist degradation in a highly oxidizing/reducing environment at increased temperatures [3].

Most of the solar radiation spectrum impinging on the Earth each day is not utilized fully in current photovoltaic (PV) renewable energy applications. Currently the majority of commercially available solar panels make use of only the visible light spectrum to generate electricity. The unused portions of the solar spectrum, namely infrared and ultraviolet wavelengths, negatively impact the solar panel through heating, in turn decreasing the generating efficiency of the unit [9]. In order to better use the complete solar spectrum it is possible to split the incoming spectrum into respective portions best suited for certain generation methods. In this design high-energy photons present in the UV portion of the solar spectrum are used to generate hydrogen by driving photo-electrochemical and photo-catalytic reactions. Infrared photons can be used with

the Rankine cycle to produce electricity [9,10]. Including multi-functionality into a single solar panel not only makes the technology more attractive from an investor standpoint, but also simultaneously allows increased electrical generation efficiency by utilizing the IR spectrum and avoiding panel heating from both the IR and UV.

There are numerous hydrogen generation methods based on using the photonic energy of the solar spectrum. PV electrolysis generates electricity from PV cells that is subsequently used in hydrogen generation through electrolysis. Commercially available silicon based solar panels currently operate with a solar-to-electricity efficiency of up to ~15 % [7], but methods focusing on converting the entire solar spectrum solely for electrical production via PV panels and thermoelectrics expect to increase conversion efficiency to near 50 % [10], allowing an increased availability of electricity from solar applications for any consequent electrolysis operation. Photo-catalytic hydrogen generation utilizing the high-energy UV portion of the solar spectrum proceeds by the interaction of a UV photon with a photo-catalyst, such as TiO_2 [3,5,7], creating an electron-hole pair. The electric charge resulting from this process is used to dissociate water molecules through the processes of photo-oxidation or photo-reduction [3,5,7]:

$$\text{Photo-oxidation: } 2H_2O \xrightarrow{h\nu} O_2 + 4H^+ + 4e^- \tag{2}$$

$$\text{Photo-reduction: } 2H_2O + 2e^- \xrightarrow{h\nu} H_2 + 2OH^- \tag{3}$$

It is important to note that photo-catalysis is a process capable of directly converting photonic energy to chemical energy. Currently, most of the known photo-catalysts can only make use of about 4% of the available solar spectrum corresponding mostly to the UV region [3], making generation systems relying exclusively on this technology impractical at the moment. The photo-catalytic principle has found use in photo-electrolysis applications, where photo-catalysts applied to one or both electrodes are exposed to light. In addition, an external source supplies electrical energy to the electrodes as in standard electrolysis cells. Here the required electrical energy needed for electrolysis is reduced due to the photonic energy harvested by the photo-catalysts [7].

Photo-electrochemical cells combine electrolysis and photo-catalysis into a single compact unit containing a photo-cathode and/or photo-anode, where at minimum the system contains one semiconductor electrode [3]. Since the semiconductor electrode works in an analogous fashion to a PV cell no external power supply is needed.

Biochemical energy contained within organic material can be used by microorganisms to produce hydrogen with or without the aid of light [3]. Dark fermentation can produce hydrogen from wastewater and other organic waste that is readily available, in turn reducing the potential for contamination of the environment by these materials [3,7]. Additionally, through bio-photolysis, micro-algae have been shown to produce hydrogen from water at standard temperature and pressure, though this process is not yet commercially viable [7].

The hydrogen generation methods presented in this section demonstrated a number of viable supply options that are available to support a clean energy hydrogen economy. Producing hydrogen in sufficient quantities to meet economic demand in a cost effective manner is only one component of the clean energy challenge. To fully realize the potential of a clean hydrogen economy adequate methods to safely store and transport hydrogen in sufficient quantities must first be developed.

1.2.2. Hydrogen Storage Methods. Two classifications of hydrogen storage exist, specifically those methods based on the storage of hydrogen in its physical form as a liquid or gas and material based methods, such as the adsorption of hydrogen in porous substrates or solid state storage of hydrogen within chemical compounds. Each type of application presents different acceptable parameters required from the hydrogen storage system. In this subsection we survey some of the different storage options available and describe some of the advantages/challenges associated with each.

1.2.2.1 Physical hydrogen storage. Storage of hydrogen in physical form is applicable in either the liquid or gaseous states. Hydrogen in gaseous form is usually stored in high-pressure tanks, with pressures of 700 bar commonly used in fuel cell vehicle applications. At standard pressure the volumetric energy density of hydrogen is 3000 times less than gasoline [11,12], facilitating the need for high pressures to achieve storage at capacities sufficient enough to allow a reasonable vehicle driving distance from a

single tank of fuel. The use of high-pressure tanks containing explosive fuel raises significant safety concerns in the event of a crash. Traditional metal storage cylinders capable of safely holding the required capacity of hydrogen at pressures of 700 bar are often heavy and bulky. In an attempt to make the tanks lighter carbon fiber composites have been successfully implemented, but the cost of the material is restrictive, accounting for about 65% of the compressed gas system cost [12]. In addition the isothermal filling of a compressed gas cylinder from 1 to 800 bar comes with an energy penalty of 2.2 kWh/kg [13]. Storing hydrogen as a simple gas is advantageous for fuel cell applications, where hydrogen can be used directly in stored form, allowing a simplified storage/fuel cell design. To maximize energy efficiency in vehicular fuel cell applications, component weight and space requirements are primary design considerations. The large footprint of compressed gas tanks and associated weight (or material cost) make gaseous storage of hydrogen less than desirable for onboard applications.

If instead hydrogen is stored in liquid form it is possible to reach volumetric energy densities in excess of 1.5 times greater than those obtained from compressed gas storage at 700 bar [11-13], though still one fourth that of gasoline [11]. Unfortunately, liquid phase storage at standard pressure requires temperatures below 20 K, the boiling point of hydrogen [11,12]. During liquefaction, an energy input equal to ~35% of the energy stored within the hydrogen is required to complete the process [11,13]. In comparison, compressing hydrogen to 690 bar requires only one third the energy [11]. Additionally, the required cryogenic system temperature for liquid storage increases the affinity of the system to absorb heat from the ambient environment, making it difficult to adequately insulate the system, resulting in hydrogen boil-off. Typical losses from a double-walled, vacuum insulated 100 m^3 dewar are on the order of .2% per day [13]. Gaseous hydrogen resulting from boil-off must be vented to prevent excessive pressure buildup in the storage system, which causes safety concerns for onboard applications when vehicles are parked in confined areas [12]. As an attempt to circumvent some of the issues discussed with physical storage of hydrogen as a compressed gas or liquid, cryo-compression, an alternative approach utilizing aspects of both methods is being investigated.

Cryo-compression utilizes two physical aspects of hydrogen, namely the increase in density of hydrogen gas as temperature is decreased, and the small compressibility of liquid hydrogen at 21 K [14]. Storage systems based on the cryo-compression technique include, cooled-compressed hydrogen gas, compressed liquid hydrogen, or a multiple phase system where hydrogen vapor exists in the tank space above the compressed liquid hydrogen phase [14]. Lowering the temperature of a compressed hydrogen gas system to 77 K allows 3 times more hydrogen to be stored in the same volume [11], without the entire energy penalty associated with cooling the gas to 21 K with liquid phase storage, although as a result of the required thermal insulation at reduced temperature, the tank weight increases. Compressing liquid hydrogen to 240 bar increases the volumetric energy density to 87 g/L, compared to 76 g/L obtained at 1 bar [14]. Moreover, the design accommodates venting at higher temperatures, allowing the tank to better cope with heat absorption issues and increasing the tank dormancy period [14]. Recently, a cryo-compressed tank demonstrated the ability to meet the DOE ultimate target for gravimetric capacity, but was unable to satisfy a number of other DOE benchmarks [14].

1.2.2.2 Materials based hydrogen storage. In contrast to physical storage, material based methods rely on chemical bonding mechanisms to facilitate the storage of hydrogen. As a result, these methods are generally considered safer alternatives to liquid or gaseous storage, as the input of energy is required to sever chemicals bonds before hydrogen can be released. Three main categories of material storage being investigated are adsorption of hydrogen in porous substrates, metallic hydrides, and complex metal hydrides. In this subsection adsorption and metallic hydride storage are surveyed, while complex metal hydrides are discussed separately in the following subsection.

Adsorption is concerned with the interactions of an adsorbate at the surface of an adsorbent material. In the case of hydrogen storage, a representative example is molecular hydrogen acting as the adsorbate, interacting with the surface of a porous carbon substrate acting as the adsorbent. Typically adsorption can occur through the processes of physisorption or chemisorption. The former is characteristic of interactions mediated by weak Van der Waals forces, while the latter occurs at higher adsorption energies than physisorption, often involving valence forces between adsorbate and

adsorbent typical of chemical compound formation [15]. Microporous activated carbon is one of the substrates being investigated for hydrogen adsorption applications. This material exhibits surface area up to 3000 m^2/g [16], significant micropore volume, and pores usually less than 1 nm in diameter [16]. The most important contributions to facilitating gas storage have been found to be total available surface area and micro-porosity [16,17]. Of the surface area accessible to hydrogen, the portion from the smallest pores contributes the most to adsorption [16,17]. The storage of hydrogen through adsorption on activated carbon offers a cheap, safe and simple design. The system is nearly fully reversible and shows fast hydrogen kinetics [18]. One of the major disadvantages associated with physisorption results from the weak interaction energies, whereby low system temperatures are required to effectively store a significant amount of hydrogen [13]. In an attempt to increase storage capacity at pressures below 100 bar, there have been attempts to incorporate metal and/or nitrogen atoms into the carbon frameworks. The addition of metal catalysts such as Pt, Ru, and Pd to the carbon substrate is thought to increase adsorption through a chemisorptive process called the hydrogen spillover effect, where molecular hydrogen dissociates through chemical adsorption on the metal catalysts, resulting in the diffusion (spillover) of atomic hydrogen onto the surface of the carbon support [17,19]. This process has been reported to increase hydrogen adsorption at room temperature below 100 bar [19,20]. Nitrogen atom addition to the substrate increases the interactions of hydrogen molecules with the substrate, leading to increased adsorption, up to 18% in some cases [21]. Metal organic frameworks (MOF's) and carbon nanotubes are additional examples of porous substrates that have been used for adsorptive hydrogen storage [11-13,20].

Certain metals such as Mg can absorb hydrogen to form metal hydrides (ex. MgH_2). When hydrogen molecules interact with the metal at the surface they are dissociated and subsequently diffuse into the bulk of the metal lattice, where the hydrogen metal atoms occupy the interstitial sites [13,22]. For this reason, the class of hydrides formed in this manner are aptly named interstitial metal hydrides. An example demonstrating some of the benefits and challenges associated with metallic hydrides is given by magnesium hydride (MgH_2), which offers the possibility of obtaining a

hydrogen storage capacity up to 7.6 wt.% for onboard applications [23-25]. The relatively inexpensive cost and lightweight of magnesium [24,25], combined with its theoretical storage capacity have attracted much attention, but the system still has challenges. During absorption a hydride layer forms at the metal's surface creating a barrier dissociated hydrogen on the surface must diffuse through to reach the lattice interior, limiting the rate of reaction [24,25]. The chemical stability of MgH_2 causes the temperature of desorption to exceed 300 °C [24,25], which is too high for on-board automotive applications. A further complication exists due to magnesium's high reactivity with oxygen to form MgO at the surface of the metal inhibiting the absorption/desorption rate of hydrogen [26].

To address the high temperature of desorption and slow kinetics resulting from hydride layer formation at the surface, the ball milling of MgH_2 powders has been investigated. Mechanical milling is thought to increase the number of surfaces available for interactions and reduce the particle size, decreasing hydrogen diffusion paths, resulting in improved absorption and desorption kinetics [23,24]. A second class of interstitial metal hydrides can be formed from intermetallic compounds. In general the intermetallic compound is comprised of two distinct elements, with one having a high affinity and one a low affinity for hydrogen [13]. Careful selection of the elements allows the properties of the resulting hydrides to be tailored to some extent [13]. Intermetallic hydrides have displayed the ability to reversibly store hydrogen at moderate conditions, although the demonstrated reversible capacities up to ~2 wt% [27] fail to meet DOE targets for onboard storage [6].

1.2.3. Complex Metal Hydrides. The complex hydride group consists of compounds that become ionic or covalent in nature after the absorption of hydrogen [13]. These complexes generally contain a metal cation (e.g. Na, Li, Mg) and anion consisting of hydrogen covalently bound around a light metal center (e.g. $[AlH_4]^-$**,** $[BH_4]^-$**).** High gravimetric and volumetric hydrogen densities make the complex hydrides attractive for onboard hydrogen storage applications, but the presence of ionic/covalent bonding mechanisms provides inherent stability, often requiring high pressures and temperatures for re/dehydriding. Despite these challenges, reversible storage under moderate conditions was achieved with the complex metal hydride $NaAlH_4$ by doping the bulk

compound with Ti in a series of experiments by Bogdanović and co-workers [28, 29]. In the initial work by Dymova, decomposition of $NaAlH_4$ to NaH and Al metal was determined to proceed in two steps [30], where 5.6 wt% hydrogen is released during the process:

$$NaAlH_4 \rightarrow \frac{1}{3}Na_3AlH_6 + \frac{2}{3}Al + H_{2(g)} \rightarrow NaH + Al + \frac{3}{2}H_{2(g)} \quad (4)$$

Though $NaAlH_4$ was previously formed in the melt from Na and Al metal under hydrogen pressure [31], it was Bogdanović who first showed these reactions were indeed reversible under moderate conditions and could proceed at rates sufficient for use in hydrogen storage applications when doped with Ti [28,29]. This discovery generated immense interest in complex metal hydride based hydrogen storage. Considerable studies were undertaken to identify other possible doping catalysts and to determine how the dopants act to achieve the improvement of reaction kinetics [32-36].

Additionally, much work was concerned with investigating other complex metal hydrides with attractive gravimetric hydrogen densities, such as $LiBH_4$ [37-44]. Containing 18.5 wt% H_2 [38], $LiBH_4$ would be an ideal hydrogen storage media if it were reversible under moderate conditions. Early work [45] indicated thermal decomposition of $LiBH_4$ could occur via two different pathways:

$$LiBH_4 \rightarrow Li + B + 2H_2 \quad (5)$$

$$LiBH_4 \rightarrow LiH + B + \frac{3}{2}H_2 \quad (6)$$

More recent work identified the presence of diborane (B_2H_6) in the decomposition products of both catalyzed and bulk $LiBH_4$ [43,46-49], while other investigations indicated the formation of $Li_2B_{12}H_{12}$ as a stable intermediate [50-52]. In studies on the bulk compound, temperatures in excess of 400 °C were required to evolve significant amounts of hydrogen gas [37,38,41,43-49]. Attempts at rehydriding bulk $LiBH_4$ at high

temperature and at pressures above 70 bar demonstrated only partial reversibility [44,49]. Slow reaction kinetics as a result of poor boron mobility makes complete regeneration a challenge [49]. Addition of catalysts and additives to $LiBH_4$ resulted in only modest gains toward hydrogen cycling under moderate conditions compared to the bulk compound [37,38,40,41,43,46,49]. Investigations of the modified systems identified degrading hydrogen capacities during cycling to be in part a consequence of boron consumption during dehydriding due to the formation of diborane [46,49].

As suitable catalysts and additives failed to yield the desired cycling efficiency of $LiBH_4$ and other complex metal hydrides of interest, research has been focused on metal hydrides at the nanoscale, where materials are often observed to display physical properties markedly different from the bulk phases. One method used to produce nanoscale complex metal hydride clusters consists of confining the hydride in nanoporous frameworks. The following section outlining nanoconfinement is provided as an introduction to the technique, which is used extensively throughout the work to be presented here.

1.3. NANOCONFINEMENT

The possible benefits of using complex metal hydrides as a hydrogen storage media have made finding solutions to the challenge of producing a system with the ability to cycle under the moderate conditions imposed by fuel cells in on board applications a top priority. In turn, many studies have focused on examining the hydrogen storage properties of metal hydrides at the nanoscale, observing some combination of enhanced kinetics, lower desorption temperatures, and the existence or improvement of reversibility for metal hydrides incorporated in nanoporous frameworks [47,48,53-59]. Following a brief overview of the frameworks used for nanoconfinement, the methods most widely used to infiltrate the open volumes of nano-frameworks with metal hydrides are discussed. Finally, as a primer to the central ideas in the work to be presented, the effects of nanoconfinement on metal hydride hydrogenation properties are addressed, considering not only the effects induced by nano-sizing the hydride, but also the impact

that may result from the chemical makeup and physical properties of the nano-framework.

1.3.1. Development of Nanoporous Frameworks. Materials possessing highly ordered nanopores were first popularized after researchers from the Mobil corporation demonstrated the ability to synthesize ordered silica based nanoporous substrates using templates composed of micelle structures formed from amphiphilic surfactant molecules [60,61]. The work demonstrated the underlying pore size and structure is closely linked to the properties of the surfactant molecules used as organic templates [60,61]. Subsequent studies of ordered silicate composites confirmed the formation proceeded via the self-assembly of the organic micelles and inorganic species in solution [62,63]. Interactions of amphiphilic template molecules via hydrogen bonding, electrostatic and van der Waals forces were found to be the driving actions behind self-assembly [63-65]. Through the proper selection of a structure directing organic template with a chemical makeup that facilitates interactions with the target chemical species selected to comprise the final framework, the self-assembly mechanism can be extended to include organic-organic and hybrid self-assembly processes [66]. In this regard, Meng and co-workers developed a method to synthesize ordered mesoporous carbon frameworks with multiple geometries through the evaporation induced organic-organic self-assembly of tri-block copolymers and phenolic resin precursors [66]. The resulting framework geometry was found to be directly related to the ratio of hydrophilic to hydrophobic segments of the copolymer template chosen for the synthesis [66]. Hybrid methods consisting of inorganic-organic and organic-organic self-assembly within the same process were demonstrated as means of attaining carbon scaffolds with increased surface area/pore volume and/or surfaces functionalized with boron or nitrogen [67-70].

Mesoporous carbon scaffolds with functionalized/non-functionalized surfaces have also been produced through a nano-casting approach using previously discovered ordered silicate templates, such as SBA-15 [71-76]. In this approach the pore volume of the silicate template material is filled with a partially polymerized mixture of the precursor materials. After heat treatments and subsequent carbonization at high temperatures, the composite silica/carbon material undergoes an etching process to

remove the silicate template, producing a mesoporous carbon scaffold that is a reverse replica of the initial silicate template.

Nanoporous scaffolds produced using the outlined synthesis methods often display total surface areas in excess of 1000 m^2/g and pore volumes up to 2 cm^3/g [71-76]. The large available pore volumes and ordered nanopores provide an ideal structure to produce regular nano-sized samples of any material successfully infiltrated within the pores of the scaffold.

1.3.2. Infiltration of Metal Hydrides. Commonly two methods are used to infiltrate metal hydrides into the pores of nanoporous scaffolds, namely solution impregnation and melt infiltration. Solution impregnation processes consist of mixing the scaffold material with a solvent containing dissolved metal hydrides. In the mixing process the solution enters the pore volume of the scaffold and remains deposited inside the pores upon evaporation of the solvent. Pore loading is limited by the solubility of the metal hydride in the chosen solvent, often resulting in the need to repeat the process multiple times to obtain significant loading. Additionally, complete removal of all solvent traces is often difficult, complicating experimental results. Melt infiltration is an alternative technique that can produce significantly high pore volume loadings of metal hydrides [47,48,53,55-59]. Metal hydrides and the scaffold material are first physically mixed together, usually by hand grinding with a mortar and pestle. The resultant mixture is then heated to a temperature just above the melting point of the metal hydride under a hydrogen over pressure adequate to prevent decomposition of the hydride. While in the liquid phase, it is possible for the hydride to enter the pores of the scaffold if pore wetting is energetically favorable. Subsequent cooling of the material below the melting point under pressure produces the desired nanoconfined metal hydride if the pores were successfully wet. The melt infiltration method is limited by the wettability of the chosen scaffold by the hydride and the ability to reach the hydrogen over pressures required to prevent decomposition.

1.3.3. Altering Hydriding Processes Through Nanoconfinement. Before confinement, powder samples of bulk metal hydrides are composed of crystalline granules on the order of several microns, but ball milling bulk hydride samples has been successful in

reducing particle sizes down to 150 nm (.15 microns) [77,54]. Substrates possessing nanopores down to ~2 nm have allowed the preparation of metal hydride nanoparticles of this order through confinement via infiltration [47,48,54,57,58]. X-ray diffraction measurements of the confined hydrides showed the absence of any Bragg peaks for confinement in pores below ~10 nm, indicating the confined hydride is amorphous [47,48,57-59]. As the radius of a metal hydride particle is reduced, the surface area to volume ratio increases as 1/r considering an idealized spherical nanoparticle, facilitating a larger number of exposed hydrogen desorption/surface nucleation sites [54]. Decreased metal hydride particle size through nanoconfinement has been correlated with a decrease in hydrogen desorption temperature [47,48,53-59], lowered activation energies [53,54], and changes in equilibrium hydrogen pressure during de/rehydriding [57], indicating a modification of the kinetics and/or thermodynamics describing the decomposition pathways of the bulk metal hydrides. Physically constraining hydrides through nanoconfinement is thought to effectively reduce the diffusion distances for mobile species during dehydrogenation improving desorption kinetics [78,79] and limit phase segregation resulting in improved rehydrogention parameters with respect to the bulk hydride [78,79]. While physical aspects of nanoconfinement play a large role in the modification of hydriding processes for confined hydrides, the chemical aspect resulting from the interaction of the hydride with the chemical species comprising the substrate may be as significant. The effect of chemical interactions of the metal hydride with the substrate pore wall is manifested in a modification of the system surface energy, which could shift the reversible hydriding reaction to the left or right depending on the magnitude the surface energy is altered [78]. A previous study [80] indicated the incorporation of boron at the surface of carbon substrates from the partial decomposition of $LiBH_4$ during the infiltration process results in a favorable hydride/substrate system energy for $LiBH_4$ to successfully wet the carbon nanopores, providing insight into the significance of hydride/substrate interactions.

1.4. OUTLINE OF WORK

The work to be presented here was undertaken with intent to determine the extent to which pore wall/metal hydride interactions impact the hydriding properties observed in nanoconfined metal hydride systems. In particular, the effect of functionalizing the carbon scaffold surface with nitrogen atoms was investigated.

In section 2 an introduction to the carbon scaffolds used in this work is provided. An overview of the different preparation methods employed and a description of the chemical processes occurring as part of each synthesis process are discussed. Section 3 provides experimental details for the measurements performed in this work. Additionally, step-by-step synthesis procedures for each scaffold are presented.

Specific studies of $LiBH_4$ and $NaAlH_4$ confined in nitrogen-functionalized carbon scaffolds are considered in Papers I and II respectively. Each of these previously published studies is self contained, complete with characterization of the particular carbon scaffolds used in that study. Neutron scattering measurements of the confined $LiBH_4$ system taken subsequent to the initial study comprising Paper I appear in Section 4 and focus on the differences of the observed dynamics from $LiBH_4$ confined in nitrogen-functionalized scaffolds with respect to a non-functionalized system. Finally, the results from a supplementary examination of impurity-induced effects on the solid solubility of metal hydrides are given in Section 5, followed in Section 6 by a summary of the conclusions that can be derived from this work in entirety.

2. NANOPOROUS CARBON SCAFFOLD PREPARATION TECHNIQUES

In this work nanoporous carbon scaffolds were prepared from published methods [66-69,71,73,74] via (1) the soft templating process, utilizing the evaporation induced self-assembly (EISA) of phenolic resins with tri-block copolymers [66-69] as the carbon source and structure directing agent respectively, and (2) the nanocasting process using SBA-15 hard templates impregnated with carbon precursors [71,73,74]. In the following sections each preparation technique will be discussed, providing insight into the relevant assembly mechanisms, interactions of the precursor materials, and the necessary process modifications to incorporate nitrogen within the resulting scaffolds. Detailed preparation processes will be presented in the following chapter.

2.1. THE SOFT TEMPLATING METHOD

Producing ordered nanoporous carbon scaffolds from a soft templated solution process requires a scheme that facilitates the arrangement of the carbon precursor materials in the desired geometrical configuration, and subsequently, the formation of C-C covalent bonds to ensure the stability of the final assembled carbon structure after removal of the template material. Meng and coworkers [66] demonstrated is was possible to synthesize ordered mesoporous polymers and carbon frameworks of 2D hexagonal, 3D cubic, 3D bicontinuous, and lamellar structures using block copolymer surfactant templates as the structure directing agent (SDA), with phenolic resin precursors as a carbon source in a solution based process. Block copolymers are formed through the polymerization of different chemical blocks, each consisting of polymerized monomers of a single type. When in solution above the critical micelle concentration (CMC), the differing chemical properties of each block (hydrophilic/hydrophobic nature) result in the formation of micelles in order to minimize the energy of the system [81,82]. Block lengths and ordering act to determine the resulting curvature of the structures formed [66,81,82]. Pluronic F-127 tri-block copolymer poly(ethylene oxide)-b-poly(propylene oxide)-b-poly(ethylene oxide) (EO_{106} –PO_{70} – EO_{106}) was used exclusively in the work to be presented.

2.1.1. Organic-Organic Evaporation Induced Self-Assembly. Assembly of organic F-127 copolymer molecules dissolved in ethanol is driven by the evaporation of solvent molecules. As the ethanol content is decreased the CMC is approached, marking the onset of micelle formation. To produce nanoporous polymer or carbon structures it is necessary to provide precursor material that is soluble in solution and has the ability to interact strongly with the copolymer template molecules. Resol (resin) precursors produced in a base catalyzed partial polymerization of phenol and formaldehyde consist of tri and tetra substituted benzene rings with the presence of phenol hydroxyl and benzyl hydroxyl groups [66]. In solution, the hydroxyl groups of the resol precursors interact strongly with the hydroxyl groups present in the PEO blocks of the F-127 copolymer template via hydrogen bonding, allowing their incorporation with the template formed structure [66]. To remain soluble and avoid macrophase separation, the mass of the resol precursors must remain low, requiring the rate and degree of polymerization to be controlled throughout the assembly process [66]. In this regard, the resol precursors are brought to and maintained at a neutral pH following the initial partial polymerization to the desired state. As ethanol evaporation procedes, the F-127 with resol precursors incorporated form micelles, sequestering the solvophobic PPO blocks toward the micelle interior. In this work, F-127 was used in the correct proportion to produce cylindrical micelles packed in a 2D hexagonal mesostructure [66], providing large ordered cylindrical pores for metal hydride infiltration.

2.1.2. Inorganic-(Organic-Organic) Evaporation Induced Self-Assembly. A modification of the organic-organic assembly mechanism can be implemented to obtain a mesoporous structure of the same 2D hexagonal arrangement, but with silica reinforced pore walls to reduce pore shrinking during the carbonization procedure [67]. The modified process depends on the co-assembly of silicate oligomers, obtained from the acid catalyzed hydrolysis of tetraethyl orthosilicate (TEOS), with the organic resol precursors and F-127 block copolymers previously described. Obtaining ordered silica-polymer-surfactant nanocomposites requires achieving a delicate balance between the competing chemical interactions of constituent species [67]. Silicate oligomers derived from TEOS contain OH groups enabling hydrogen bonding with both resol and surfactant

molecules [67]. Here, the hybrid process is the culmination of two individual competing processes previously discussed: 1) the self-assembly of silicate oligomers with copolymer surfactant templates into ordered silicate nanostructures, as pioneered by the Mobil corporation [60,61], and 2) the organic-organic self-assembly of resol precursors with copolymer templates. As the evaporation of ethanol drives the assembly of the F-127 surfactant into micelles, silicate oligomers and resol precursors incorporate with the PEO block. Cooperatively, silicate oligomers crosslink, and condense into tetrahedral networks around resol molecules to form an interpenetrating reinforcing framework [67] that will resist structure collapse during thermopolymerization, and reduce pore shrinkage during the carbonization procedure up to 20% [67].

2.1.3. Nitrogen Functionalization. The soft templating process can allow the incorporation of nitrogen within the final structure through the addition of a nitrogen-containing precursor with the ability to interact strongly with resol molecules during the assembly process [68,69]. Dicyandiamide (DCDA) molecules ($C_2H_4N_4$), composed of two amine and one nitrile group, have a nitrogen content of 66.7% by mass. PEO-PPO-PEO Pluronic copolymers interact only weakly with DCDA during the direct assembly of the two components, producing poor mesostructure assemblies that are known to collapse during pyrolysis, resulting in disordered, porous carbon nitride of low surface area [83]. Resol precursors have the ability to bridge Pluronic F-127 copolymer and DCDA via hydrogen bonding and electrostatic interactions [68,69]. As the assembly process proceeds, the abundant hydroxyl groups of the resol precursors interact with the F-127 through hydrogen bonding as previously noted, though now amine groups present in DCDA molecules can capture H^+ ions of the resol hydroxyl groups, facilitating an electrostatic interaction between the partially positive charged DCDA molecule and negatively charged resol, which allows inclusion of the DCDA molecule in the resol network, and prevents phase segregation [68,69]. Assembly continues in the same manner as described in the non-functionalized process, resulting in cylindrical micelles that further pack into a 2D hexagonal geometry.

Nitrogen functionalized carbon has been successfully synthesized with and without the addition of TEOS to the assembly process [68,69]. As the ratio of DCDA is

increased, mesostructure degeneration occurs as a result of expansion [69]. Excess DCDA can form nanoparticles within the resol matrix, resulting in a broad distribution of pore sizes [69]. Even when well-dispersed, the presence of DCDA affects the quality of the mesostructure obtained for nitrogen-functionalized carbon synthesized without utilizing TEOS, as evidenced by the decreased surface area, and wide pore distribution of the functionalized scaffold [69] in relation to the base non-functionalized scaffold [66]. The addition of TEOS provides a reinforcing framework within the resol matrix [67], allowing ordered nitrogen-functionalized carbon with high surface area to be produced, with nitrogen content up to ~6 atomic % [68].

2.1.4. Thermopolymerization. At the completion of evaporation induced self-assembly the material consists of a uniform, flexible transparent film composed of resol precursors incorporated around the outside of copolymer formed cylindrical micelles that have packed into a 2D hexagonal geometry. Additionally, if TEOS was added, an interpenetrating silica framework is present around the resol molecules. In the case of nitrogen functionalization, DCDA has been incorporated with the resol precursors. Since the assembly takes place near room temperature, and the resol precursors are brought to a nearly neutral pH after the initial synthesis, the polymerization rate is significantly decreased during the assembly process [66]. Retaining the mesostructure formed during the assembly process is accomplished by forming a 3-D covalently bonded resin framework through a thermopolymerization process [66]. Heating the assembled material at a low temperature (100 °C) facilitates the cross-linking of the resol precursors at a slow rate, avoiding structure deformation [66]. A sufficiently long period of treatment (~24 hours) ensures complete cross-linkage [66]. With an integral resin network in place after thermopolymerization the templating material can now be removed from the composite samples to produce the desired porous material.

2.1.5. Carbonization /Template Removal. Heat treatment of nanocomposites synthesized using the soft-templating process facilitates both the removal of the soft-template material in addition to converting the polymer to carbon. Decomposition of the Pluronic F-127 co-polymer template in the nanocomposites occurs in the temperature range of 350 to 400 °C [66-69]. Meng and co-workers found adding a small amount of

oxygen (>2.4%) in the (nitrogen or argon) feed gas during the heating process results in carbon scaffolds with a larger pore volume, and higher surface area, due to a more complete removal of the copolymer template and residual decomposition products [66]. As the material is heated to 350 °C further cross-linkage of the phenolic resin occurs, resulting in a nearly ideal phenolic resin polymer framework [66,67]. A continuous framework shrinkage occurs at temperatures above 350 °C, due to the on-going cross-linking of the phenolic resin after template removal, and the gradual transition of mesoporous polymer to carbon through dehydrogenation as the temperature nears 600 °C [66]. Incorporation of TEOS during the assembly stage of the nanocomposites reduces framework contraction during carbonization by providing a hard reinforcing framework after the soft template has been removed [67]. Additional heating to higher temperature can reduce the residual hydrogen left on the framework, though at higher temperature any oxygen present in the inert feed gas, even in small quantities, reduces the product yield from some combustion of organic material [66]. Following carbonization, silica if utilized during the synthesis, is removed through etching the product in hydrofluoric acid solution, and washing the material [67,68]. Removal of the silica produces numerous micropores within the pore walls of the nitrogen-functionalized/non-functionalized mesoporous carbons, resulting in a material with a higher surface area, and higher pore volume [67,68].

2.2. THE NANOCASTING METHOD

In relation to soft-templating processes with complex assembly mechanisms, the nanocasting process is much simpler. A nanoporous hard template is filled step-wise with the necessary precursors to produce the desired material. Scaffolds produced by nanocasting inherit the inverse geometry of the hard template following heat treatment to convert the precursors to solids, and the subsequent removal of the template. The simplicity of the method, combined with the preformed nanostructure, enables a wide variety of materials to be produced in this manner. Additionally, in the case of synthesizing functionalized mesoporous carbon, hard templates often allow higher levels of doping to be achieved by circumventing the issues of phase segregation and loss of

nanostructure ordering that occur during assembly in the soft templating process as the level of dopant inclusion is increased.

2.2.1. Hard Template Selection. Nanoporous carbon scaffolds produced in this work with the hard templating method utilized the SBA-15 hard silicate template in accordance with previously published methods [71,73,74]. SBA-15 contains a 2D hexagonal arrangement of mesopores with p6*mm* symmetry that can be varied from 5 to 30 nm during the synthesis process [65]. The material is synthesized by the self-assembly of silicate oligomers derived from the acid hydrolysis of TEOS, with PEO-PPO-PEO based copolymer soft templates [65]. As with previously described soft-templating processes, the copolymer molecules form cylindrical micelles with the PEO blocks making up the outside surface of the cylinder. Silicate oligomers containing OH groups condense and incorporate with the OH groups of the PEO blocks through hydrogen bonding during solvent evaporation. Hexagonal SBA-15 is reported to be thermally stable to high temperatures [65]. The high thermal stability of SBA-15 makes the template ideal for use in nanoporous carbon synthesis, which requires temperatures in excess of 600 °C to carbonize the infiltrated precursor and produce well ordered carbon [71]. Moreover, during assembly silicate oligomers are thought to interpenetrate the PEO blocks of the copolymer template, leading to an array of micropores perpendicularly connecting the main mesopore channels of SBA-15 after calcination [84]. The existence of interconnecting micropores facilitate the production of ordered nanoporous carbon by providing a supporting structure to maintain the geometry of the nanorods formed from the main channels of the SBA-15 template [71]. In contrast, the MCM-41 silica hard template is analogous to SBA-15, but without interconnecting micropores. An attempt to utilize MCM-41 in a nanocasting process resulted in only unconnected carbon nanorods with a featureless XRD profile [71].

2.2.2. Carbon Precursors. Synthesizing nanoporous carbon via the hard templating technique requires selecting a carbon precursor material that can be easily infiltrated into the pores, thus requiring the precursor be a liquid, or sufficiently soluble in solution to allow high pore loadings to be achieved [85]. Additionally, the precursor must not react with the chosen hard template, and resist shrinking during the carbonization process

[85]. In this work, CMK-3 carbon [71] was synthesized using sucrose as the carbon source and SBA-15 as the hard template. Sucrose is dissolved in a mixture of water and sulfuric acid under stirring at room temperature. Addition of the sulfuric acid aids in the dehydration of the dissolved sucrose. As SBA-15 is added to the mixture, the solution infiltrates both the meso and micropores of the template. Heat treatment at temperatures of 100 and 160 °C facilitate the partial polymerization of the dehydrated sucrose. After heat treatment, the dark brown/black solid powder obtained is exposed a second time to a mixture of sulfuric acid/water/sucrose to ensure full pore loading, and the heat treatments are repeated. The resulting composite sample consists of the SBA-15 hard template material containing polymerized sucrose in the micro and mesopore voids.

2.2.3. Nitrogen-Functionalization. Producing CMK-3 carbon functionalized w-ith nitrogen requires the selection of different precursor materials that provide a source of carbon and nitrogen. Work by Vinu et al. [73,74] demonstrated carbon tetrachloride (CTC) and ethylenediamine (EDA) could be used as precursor materials with SBA-15 as the hard template to obtain nitrogen-functionalized CMK-3 carbon (denoted NCMK-3 in the work to be presented). CTC and EDA are both liquids at room temperature, removing the need of any extra solvent addition to successfully infiltrate the pores of the SBA-15 template. Unlike the non-functionalized CMK-3 process, pore infiltration and partial polymerization of the precursors occurs simultaneously during the free-radical polymerization of the CTC/EDA mixture under reflux at 90 °C. At the end of reflux a dark brown mixture is obtained consisting of partially polymerized EDA/CTC within the pores of the SBA-15 template. Drying and hand grinding the product results in a fine brown powder of template/carbon nitride polymer composites [73,74].

2.2.4. Carbonization/Template Removal. Both nitrogen functionalized/non-functionalized nanocomposites synthesized using the hard templating method undergo carbonization in a manner similar to the process used for soft-templated materials. Heating under an inert atmosphere to 600 °C or higher is required to obtain fully ordered carbon nanostructures displaying p6*m* symmetry [71,73,74]. During the heating process, a cross-linked carbon/carbon-nitrogen network is formed in the pores of the SBA-15 template [71,73,74]. After carbonization, the SBA-15 template is removed through

etching in hydrofluoric acid solution, followed by washing. The resulting material is nitrogen functionalized/non-functionalized mesoporous carbon, consisting of nanorods formed in the pores of the SBA-15 template that are organized in a hexagonal arrangement. Disordered nano-fibrils formed in the micropores connecting the main pore channels of the SBA-15 template hold the hexagonal array in place [71,73,74].

3. EXPERIMENTAL METHODS

A number of measurement techniques were utilized to characterize the synthesized carbon scaffolds and nanoconfined metal hydride samples in the studies composing this work. Here, the details of each experimental measurement are presented. Synthesis procedures used to prepare the nitrogen functionalized/non-functionalized carbon scaffolds introduced in the previous section are given in detail, followed by the processes applied to infiltrate specific metal hydrides into the scaffolds. Information for neutron scattering measurements and the NaH/NaOH system are provided in their respective sections.

3.1. EXPERIMENTAL MEASUREMENTS

3.1.1. X-ray Diffraction. Powder X-ray diffraction (PXRD) measurements were acquired using a Rigaku Ultima IV X-ray diffractometer with a Cu K_α radiation source. Samples containing hydrides were sealed using Mylar film in an argon filled glovebox (O_2 < 1 ppm) to prevent air exposure during measurements.

3.1.2. Nitrogen Sorption. N_2 sorption isotherms were recorded using a SA3100 (Coulter) analyzer at 77 K. Samples were loaded into glass analysis vessels in an argon filled glovebox (O_2 < 1 ppm) and transported to the analyzer without air exposure. Before analysis, the bare carbon samples were outgassed at 300 °C for 10 hours, and the infiltrated carbon samples outgassed at 40 °C for 30 minutes on the analyzer. The specific surface area S_{BET} was calculated using the Brunauer-Emmett-Teller (BET) method in a relative pressure range of 0.05 to 0.2. Pore size distributions and total pore volume were calculated using the Barrett, Joyner, and Halenda (BJH) calculation model using data from the adsorption isotherm. The total pore volume was estimated by the amount adsorbed at a relative pressure (P_s/P_0) of 0.99.

3.1.3. Differential Scanning Calorimetry. Scans were taken on a Perkin-Elmer DSC 7 under flowing nitrogen purge gas. Samples were prepared in an argon filled glovebox (O_2 < 1ppm) by placing ~2 mg of sample in Perkin Elmer hermetically sealed sample pans. The samples were transported to and loaded into the DSC 7 without air

exposure. Immediately before closing the cover and initiating the scan a small hole was poked in the hermetic lid to allow gas escape during the heating process.

3.1.4. Residual Gas Analysis Mass Spectroscopy. Measurements were recorded using a SRS RGA200 residual gas analyzer and high temperature sample stage. The system is separated into a high vacuum (HV) (10^{-8}-10^{-5} Torr) sample chamber and ultra high vacuum (UHV) (10^{-9}-10^{-7} Torr) gas analysis chamber. The RGA maintains a line of sight with the sample through a small flow hole to produce the best possible signal. Samples are loaded into Texas Instruments Tzero aluminum pans with hermetic lids in an argon filled glovebox (O_2 < 1 ppm). The samples are transported without air exposure to an argon filled glovebag that acts as an antechamber for the RGA system. Just before loading, a small hole is poked in the hermetic lid to allow gas escape during the experiment. Sample temperature is increased at a chosen pre-calibrated ramp rate from room temperature up to the desired final temperature (< 450 °C). The estimated sample temperature uncertainty is ±10 °C, but repeated scans of the same compound show good reproducibility of gas release at the same measured temperature.

3.1.5. Transmission Electron Microscopy. Carbon scaffolds were investigated using a Philips EM430 high-resolution transmission electron microscope (TEM). The carbon scaffold powder was supported on a holey copper grid for measurements.

3.1.6. Hydrogen Cycling/Kinetics Measurements. A custom built Sieverts-type apparatus was used to perform hydrogen cycling and kinetics measurements. Figure 3.1 displays the layout of the Sieverts apparatus. The system consists of a manifold equipped with calibrated volumes of different capacities, with connection ports for vacuum, H_2, and He gas. Manifold pressures are monitored with two calibrated pressure transducers (MKS model 870B). Sample and manifold temperatures are monitored using type K thermocouples. Pressures and temperatures are recorded with data acquisition software on an interfaced computer. A cylindrical stainless-steel sample holder equipped with a manual valve allows samples to be loaded in an argon filled glovebox (O_2 < 1 ppm) and transported to the apparatus without air exposure. Samples are heated using a cylindrical resistive heating element that fits around the outside of the sample holder connected to a

PID controller. The sample holder/heating element is wrapped in an insulating glass fiber blanket to minimize heat flow to the surrounding environment during the heating process.

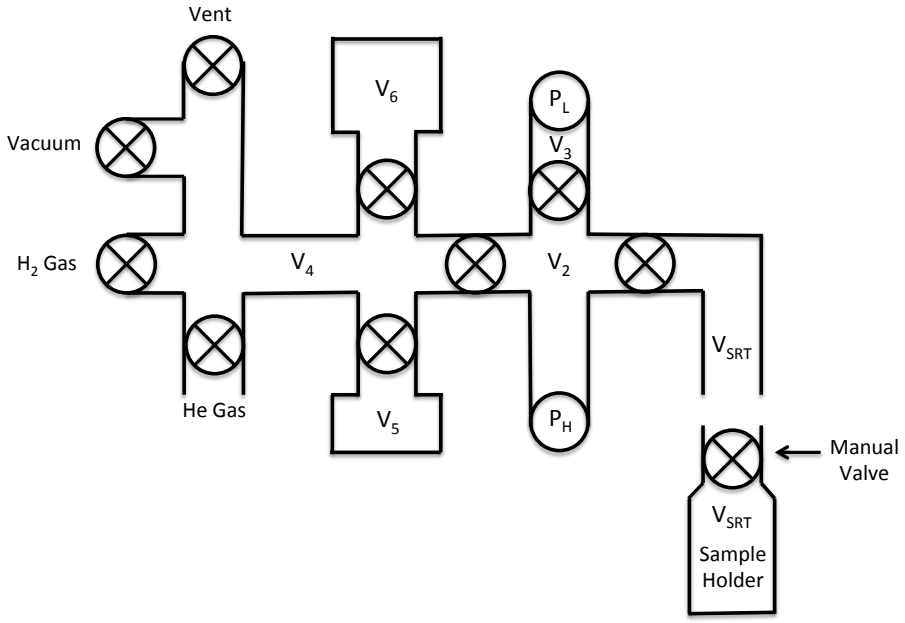

Figure 3.1. Diagram showing the layout of the Sieverts apparatus used for hydrogen cycling and kinetics measurements.

During hydrogen desorption measurements samples were heated at a ramp rate of 4 ºC/min to the desired temperature, desorbing hydrogen into a pre-evacuated and carefully measured volume of the Sieverts apparatus. For rehydrogenation the samples were placed under a predetermined hydrogen pressure at room temperature. The samples were heated to and held at the desired rehydriding temperature for a prescribed dwell time, typically 12 to 15 hours. At the end of the dwell period the samples were cooled to room temperature under hydrogen pressure to prevent any hydrogen desorption during cooling.

Isothermal kinetics measurements and Arrhenius analyses were performed on bulk and nanoconfined metal hydride samples to determine the activation energies of hydrogen desorption. The hydrogen evolution rates were recorded under isothermal conditions at predetermined temperature increments. Samples were quickly heated to the desired temperature at which the system was briefly evacuated ($P < 1.5 \times 10^{-3}$ MPa). As the samples evolved hydrogen into the static vacuum of the Sieverts apparatus during a dwell period at the set temperature, the pressure within the volume was recorded as a function of time. Deviations of the temperature from the desired set point during the dwell period were < 1 °C. At the end of the dwell period the samples were quickly heated to the next setpoint and the process repeated. At each respective temperature, the rate was determined from the change in pressure. Pressure changes with respect to time exhibited linear behavior over the measured time period, with correlation coefficients exceeding 0.98. The rate of hydrogen desorption can be related to the temperature of the sample through the Arrhenius equation:

$$\text{Rate} = \frac{d[\text{H}_2]}{\text{dt}} = \text{K}_0 \text{e}^{-\frac{\text{E}_\text{A}}{\text{RT}}} \quad (1)$$

where K_0 is the pre-exponential rate constant or frequency factor, E_A is the activation energy, and $[H_2]$ is the concentration of hydrogen gas.

3.2. SAMPLE PREPARATION

3.2.1. Chemicals. Phenol, formalin, pentane, tetrahydrofuran (THF), tetra-ethyl orthosilicate (TEOS), Pluronic F-127 tri-block copolymer, dicyandiamide (DCDA), carbon tetrachloride (CTC) and ethylenediamine (EDA) were purchased from Sigma-Aldrich and used without purification unless noted in the preparation procedures. SBA-15 silicate hard template was purchased from ACS Materials. Deionized water was used in all experiments.

3.2.2. Nanoporous Carbon Scaffold Synthesis. Here the individual carbon preparation methods are described in detail. Resol precursors were prepared separately using the presented method for the respective NPC and NNPC processes.

3.2.2.1 Resol precursors. A modified version of the process described by Meng et al. [66] was used for the synthesis. In a typical process, 6.1 g of phenol was melted in a Schlenk flask at 40 ºC and added to 1.3 g of 20 wt.% NaOH solution under stirring. At the end of 10 minutes, 10.5 g of formalin was added at a temperature below 50 ºC dropwise. The resulting mixture was placed in a water bath at 70 ºC under stirring for 80 minutes and then allowed to cool to room temperature (RT). Using 1 N HCl the pH of the solution was adjusted to ~7.0. Water was removed from the solution under vacuum at 45 ºC, producing a gel-like product. Ethanol was added to dissolve the product, producing a 20 wt.% resol-ethanol solution after mixing. The solution was allowed to settle and then poured off into a separate flask, leaving behind the salt from the acid-base neutralization.

3.2.2.2 Soft templated nanoporous carbon. A modified version of the process described by Liu et al. [67] was used for the synthesis. In a typical process to produce 2D hexagonal carbon, 16 g F-127 tri-block copolymer was added to a solution consisting of 80 g ethanol and 10 g 0.2 M HCl. After stirring for 1 hour at 40 ºC, 20.8 g TEOS and 50 g of 20 wt.% resol-ethanol solution were added sequentially, followed by stirring for 2 hours at 40 ºC. The solution was poured into a glass pan and allowed to evaporate overnight at RT, producing a transparent film. In order to thermopolymerize the sample, heat treatment at 100 ºC was carried out in an oven for 24 hours. The sample was scraped from the pan, ground into a fine powder, and placed into a tube furnace under flowing nitrogen for calcination at 350 ºC for 3 hours, followed by carbonization at 900 ºC for 2 hours. During the heat treatment the ramp rate was 1 ºC/min below 600 ºC and 5 ºC/min after. To remove the silicate, the sample was etched in 5 wt.% HF solution overnight twice under stirring, followed by washing with ethanol and deionized water. Finally, the carbon sample was dried for 24 hours at 100 ºC and additionally overnight at 300 ºC under dynamic vacuum. The final sample was transported without air exposure to an argon-filled glovebox for storage.

3.2.2.3 Nitrogen-functionalized soft templated nanoporous carbon. A modified version of the process described by Song et al. [68] was used for the synthesis. In a typical process, 8 g of F-127 tri-block co-polymer and 7.5 g dicyandiamide are added to a solution consisting of 100 g ethanol, 50 g H_2O, and 10 g 0.2 M HCl. After stirring for 1

hour at 40 ºC, 10.4 g TEOS and 25 g of 20 wt.% resol-ethanol solution were added sequentially, followed by stirring for an additional 2 hours at 40 ºC. In order to evaporate the solvent, the mixture was poured into pans and placed in an oven at 45 ºC for 8 hours resulting in the formation of uniform films. In order to thermopolymerize the sample, heat treatment at 100 ºC was carried out in an oven for 24 hours. The sample was scraped from the pan, ground into a fine powder, and placed into a tube furnace under flowing nitrogen for calcination at 250 ºC for 2 hours, followed by carbonization at 700 ºC for 3 hours. During the heat treatment the ramp rate was 1 ºC/min. To remove the silicate, the sample was etched in 5 wt.% HF solution overnight twice under stirring, followed by washing with ethanol and deionized water. Finally, the carbon sample was dried for 24 hours at 100 ºC and additionally overnight at 300 ºC under dynamic vacuum. The final sample was transported without air exposure to an argon-filled glovebox for storage.

3.2.2.4 Nanocasted nanoporous carbon. A modified version of the process described by Ryoo et al. [71] was used for the synthesis. In a typical process, 6.25 g sucrose was dissolved in a mixture consisting of 0.7 g H_2SO_4 and 25 g H_2O, followed by the addition of 5 g SBA-15 silicate hard template material. After 15 minutes of stirring, a uniform white slurry was obtained. Heat treatments of the sample at 100 ºC for 6 hours and 160 ºC for 6 hours were performed sequentially. The resulting black/brown powder sample was added to a solution consisting of 4 g sucrose dissolved in 0.45 g H_2SO_4 and 25 g H_2O. After 25 minutes of stirring the previous heat treatments were repeated, followed by carbonization of the sample in a tube furnace at 900 ºC under flowing argon for 3 hours. During the heat treatment the ramp rate was 1 ºC/min below 600 ºC and 5 ºC/min after. To remove the hard silicate template, the sample was etched in 5 wt.% HF solution overnight twice under stirring, followed by washing with ethanol and deionized water. Finally, the carbon sample was dried for 24 hours at 100 ºC and additionally overnight at 300 ºC under dynamic vacuum. The final sample was transported without air exposure to an argon-filled glovebox for storage.

3.2.2.5 Nitrogen-functionalized nanocasted nanoporous carbon. A modified version of the process described by Vinu et al. [73] was used for the synthesis. In a typical process using Schlenk line techniques, 6.75 g EDA and 15 g CTC were added to a

jacketed flask under stirring at RT. Next, 2.5 g SBA-15 silicate template was added to the mixture of EDA and CTC under stirring slowly. The resultant mixture was allowed to stir for 1 hour until a uniform white slurry was obtained. Under continuous stirring, the temperature was increased to 90 ºC, at which the mixture was refluxed and stirred for 6 hours. The obtained brown colored solid mixture was placed in a drying oven at 100 ºC for 12 hours, and subsequently ground into a fine powder. Sample calcination was carried out in a tubular furnace under flowing nitrogen at 600 ºC for 5 hours. A ramp rate of 3 ºC/min was used to bring the sample up to 600 ºC. After calcination, the composite carbon/silica powder was immersed in 5 wt.% HF acid solution under stirring to dissolve the silica template. Carbon powder was recovered following filtration and several washings with ethanol and deionized water. Finally, the carbon sample was dried for 24 hours at 100 ºC and additionally overnight at 300 ºC under dynamic vacuum. The final sample was transported without air exposure to an argon-filled glovebox for storage.

3.2.3. $NaAlH_4$ Purification. Before use, 7.5 g of the as-received $NaAlH_4$ was dissolved in 400 mL of freshly dried/distilled THF. After stirring for 4 hours the insoluble impurities were allowed to precipitate from the solution. The supernatant was transferred to a separate flask, where the solution was concentrated to a volume of ~125 mL under vacuum. Under stirring 375 mL of dried/distilled pentane was added to the solution, separating $NaAlH_4$ from the solution as a fine precipitate. After removal of the supernatant, $NaAlH_4$ was washed using ~100 mL of dried/distilled pentane. $NaAlH_4$ in the form of a fine white powder was obtained after drying under vacuum. All operations were carried out using Schlenk line techniques.

3.2.4. Infiltration of Nanoporous Carbon Scaffolds with Metal Hydrides. Synthesized carbon scaffolds were infiltrated with metal hydrides using the custom-built Sieverts-type apparatus described previously and outlined in Figure 3.1. Prior to infiltration the substrate materials were dried under dynamic vacuum overnight at 300 °C. Samples were prepared by mixing the appropriate amounts of substrate and metal hydride with a mortar and pestle for 10 minutes, followed by loading into an Al foil roll and placing into a stainless-steel sample holder equipped with a manual valve. All sample handling was performed in an argon-filled glovebox (O_2 < 1 ppm). Samples were

transported to the Sieverts apparatus without air exposure, where they were placed under H_2 over pressures sufficient to prevent the decomposition of the metal hydride upon melting.

3.2.4.1 Melt infiltration of $LiBH_4$. To prevent decomposition, an overpressure of 100 bar H_2 was used for the melt infiltration of $LiBH_4$ into carbon scaffolds at 300 °C. The reported equilibrium pressure for $LiBH_4$ at 370 °C is 1 bar H_2 [44]. Infiltration consisted of heating the pressurized premixed carbon/$LiBH_4$ sample from room temperature to 300 °C with a dwell period of 40 minutes at 300 °C. Samples were allowed to cool under pressure to prevent dehydriding.

3.2.4.2 Melt infiltration of $NaAlH_4$. Premixed carbon/$NaAlH_4$ samples were placed under 190 bar H_2 pressure at room temperature. The reported equilibrium pressure for $NaAlH_4$ at melting (~184 °C) is 128 bar [30]. During infiltration the samples were heated to 200 °C reaching a final pressure of 205 bar H_2. After a dwell period of 45 minutes the samples were cooled under pressure to prevent dehydriding.

PAPER

I. SURFACE-FUNCTIONALIZED NANOPOROUS CARBONS FOR KINETICALLY STABILIZED COMPLEX HYDRIDES THROUGH LEWIS ACID-LEWIS BASE CHEMISTRY

C. L. Carr,[†] and E. H. Majzoub[†,*]

[†]Center for Nanoscience and Department of Physics and Astronomy, and [‡]Department of Chemistry and Biochemistry, University of Missouri-St. Louis, One University Boulevard, St. Louis, Missouri 63121, United States

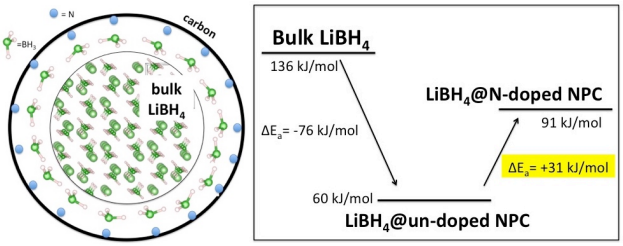

Table of Contents Graphic from Published Paper

ABSTRACT

Complex metal hydrides are an attractive hydrogen storage option due to their high gravimetric hydrogen capacities, but the re/dehydriding reactions generally possess unfavorable thermodynamics and kinetics. Recent studies have attempted to alter these properties through confinement of complex hydrides in nanoporous substrates. For example, $LiBH_4$ may be melt-infiltrated into a nanoporous carbon ($LiBH_4$@NPC), where

electron-withdrawing boron concomitantly incorporates into the substrate, facilitating the wetting of the pores with molten $LiBH_4$. We present results of the surface functionality displayed by incorporation of electron-donating nitrogen into a nanoporous carbon. The presence of pyridinic nitrogen in the substrate, confirmed by XPS analysis, acts as a Lewis base. Our results indicate partial decomposition on melt-infiltration of $LiBH_4$ may produce electron-accepting BH_3 defects at the surface of the hydride forming a stabilizing capping layer. Isothermal hydrogen desorption measurements indicate an activation energy increase of greater than 30 kJ/mol for $LiBH_4$ confined in N-doped versus undoped substrates. Further, temperature-programmed desorption (TPD) measurements show a temperature increase of over 25 °C in the diborane (B_2H_6) signature, marking the beginning of the dehydriding reaction. Stabilizing metal hydrides kinetically through the formation of a capping layer induced by substrate functionalities may allow the use of a wide class of unstable complex metal hydrides with enthalpies below 15 kJ/mol H_2, such as AlH_3, in hydrogen storage systems.

1. INTRODUCTION

Complex metal hydrides for the solid storage of hydrogen for proton exchange membrane fuel cells (PEMFC) generally run into two major difficulties. (1) The majority of known complex hydrides have thermodynamic enthalpy changes $\Delta H°$ for hydrogen desorption that are too large or too small to give pressures between 1 and 10 bar H_2 at the operating temperature of the PEM cell at about 80 °C. (2) Of the materials that do possess reasonable enthalpy changes on the order of 20-30 kJ/mol H_2, they generally suffer from poor kinetics, especially on rehydriding. Extensive materials discovery efforts have yielded many new complex hydrides, but none with acceptable kinetics and thermodynamics meeting the DOE targets for on-board hydrogen storage applications [1]. Recent attempts to control these parameters have focused on nanosize hydrides and nanoconfinement to utilize the large surface-to-volume ratios and changes in surface and interface energies.

Alane (AlH_3) has been extensively studied as a possible candidate for hydrogen storage due to its exceptional wt % and volumetric density [2]. However, the enthalpy

change for alane desorption (11 kJ/molH_2) makes it very unstable with an equilibrium pressure P_{eq}(300 K) of approximately 10 kbar. However, it has long been known in the hydrogen storage community that alane, despite its large thermodynamic instability, is stable in air for decades. The nature of this stability has not been elucidated, but it must be due to a stable surface layer where the decomposition process is inhibited kinetically. This "kinetic stabilization" may provide a useful approach to using a wide class of complex hydrides with enthalpies below 15 kJ/mol H_2, if the surface can be kinetically stabilized. Thermodynamic stabilization in nanoporous frameworks requires nanosize hydrides with a large surface/volume ratio and/or changes in interface energies. The latter may be altered using this functionalization approach as well.

We present evidence that highly ordered, surface functionalized carbons can be used to construct a surface "capping" layer for the complex hydride $LiBH_4$ through Lewis acid – Lewis base chemistry. Although $LiBH_4$ is already too stable for on-board hydrogen storage applications, it provides a well-characterized system for our experiments.

2. EXPERIMENTAL METHODS

Isothermal kinetics measurements were performed using a custom built Sieverts type apparatus. The system consists of a cylindrical stainless steel sample holder equipped with a manual valve allowing samples to be loaded in an argon filled glovebox (O_2 < 1ppm) and transported to the apparatus without air exposure. The system manifold consists of calibrated volumes of different capacities, with connection ports for vacuum, H_2, and He gas. Manifold pressures are monitored with two calibrated pressure transducers (MKS model 870B). Sample and manifold temperatures were monitored using type K thermocouples. Pressures and temperatures were recorded with data acquisition software on an interfaced computer. Samples are heated using a cylindrical resistive heating element that fits around the outside of the sample holder connected to a (PID) controller. During the experiment samples were quickly heated to the desired set point at which the system was briefly evacuated (P < 15 mbar). As the samples evolved hydrogen into the evacuated volume during a dwell period at the set temperature, the pressure within the volume was recorded as a function of time. At the end of the dwell

period, the samples were quickly heated to the next set point and the process repeated. Melt infiltration of carbon substrates with $LiBH_4$ was performed using the Sieverts apparatus already described. The amount of $LiBH_4$ used was calculated based on 30% volume filling of each respective substrate. Using the total pore volume per gram obtained from N_2 sorption measurements and a preselected mass of the substrate, the necessary amount of $LiBH_4$ necessary to fill 30% of the pore volume was calculated based on a mass density of 0.67 g/cm^3 for bulk $LiBH_4$. Prior to infiltration the substrate materials were dried under dynamic vacuum overnight at 300 °C. Samples were prepared by mixing the appropriate amounts of substrate/$LiBH_4$ in a mortar/pestle for 5 min, followed by loading into an Al foil roll and placement into a stainless steel sample holder equipped with a manual valve. All sample handling was performed in an argon filled glovebox (O_2 < 1 ppm). Samples were transported to the Sieverts apparatus without air exposure, where they were placed under 100 bar H_2 pressure and heated to 300 °C. Following a dwell period of 40 min at 300 °C, the samples were allowed to cool under pressure. N_2 sorption isotherms were recorded using a SA3100 (Coulter) analyzer at 77 K. Before analysis, samples were outgassed at 300 °C for 10 h. The specific surface area S_{BET} was calculated using the Brunauer-Emmett-Teller (BET) method in a relative pressure range of 0.05 to 0.2. Pore size distributions and total pore volume were calculated using the Barrett, Joyner, and Halenda (BJH) calculation model using data from the adsorption isotherm. The total pore volume was estimated by the amount adsorbed at a relative pressure (P_s/P_0) of 0.99. Mass spectroscopy was performed using a direct line of sight residual gas analysis mass spectrometer (RGA-MS) consisting of a SRS RGA200 residual gas analyzer and high temperature sample stage. The system is separated into a HV (10^{-8}-10^{-5} Torr) sample chamber and UHV (10^{-9}-10^{-7} Torr) gas analysis chamber. The RGA maintains a line of sight with the sample through a small flow hole to produce the best possible signal. Samples are loaded into Texas Instruments Tzero aluminum pans with hermetic lids in an argon filled glovebox (O_2 < 1ppm). The samples are transported without air exposure to an argon filled glovebag acting as an antechamber for the RGA system. Just before loading, a small hole is poked in the hermetic lid to allow gas escape during the experiment. Sample temperature was

increased at 8 C/Min from room temperature up to 350 °C. Sample temperature calibration at the specified ramp rate was accomplished by placing a thermocouple in the center of a Tzero pan filled with glass beads to insulate the thermocouple from the pan walls. The resulting data was fit as a function of the heater block temperature measured with a separate thermocouple connected to a (PID) controller. The estimated sample temperature uncertainty is ± 10 °C from the fit, but repeated scans of the same compound show good reproducibility of gas release at the same temperature. X-ray photoelectron spectroscopy scans were collected using a Kratos Axis 165 spectrometer using monochromatic Al radiation. During the scans, charge neutralization was employed through the use of a low energy electron flood gun. Nitrogen-doped carbon (NCMK3) was purchased from ACS Materials and used as received after drying under dynamic vacuum.

3. RESULTS AND DISCUSSION

The modification of kinetic and/or thermodynamic properties of metal hydrides by nanoconfinement in nanoporous substrates has been investigated for $LiBH_4$ [3-5], $NaAlH_4$ [6-8], and $Li_4BN_3H_{10}$ [9]. In nanoconfined $LiBH_4$@NPC it was shown that inadvertent boron doping occurs during melt-infiltration and results in a surface functionalization that produces a favorable wetting energy, without which the carbon substrate would not be wetted by $LiBH_4$ [10,11]. Electron-accepting B heteroatoms effectively bind Li^+ on melt infiltration and provide a surface defect that allows small clusters of $LiBH_4$ to wet the substrate. In this work we have selected two carbon scaffolds with different morphologies and investigate the properties of nanoconfined $LiBH_4$ in the presence of electron donating nitrogen heteroatoms. (1) NPC with cylindrical pores packed in a 2D hexagonal P6*m* symmetry was synthesized [12] by the thermopolymerization and subsequent carbonization of polymer nanostructures produced using an inorganic/organic evaporation induced self-assembly (EISA) process in an ethanol solution consisting of F-127 triblock copolymer, tetraethyl orthosilicate (TEOS) and phenol/formaldehyde resol precursors as the carbon source (detailed synthesis procedures can be found in the Supporting Information). After carbonization, the silicate

is removed from the pore walls by etching with 5 wt % HF acid solution. Nitrogen doping of NPC (hereafter NNPC) can be accomplished by the addition of dicyandiamide during the assembly process using a literature method [13]. (2) CMK-3 produced via the nanocasting method [14] using the hard silicate template SBA-15 possessing cylindrical pores packed in 2D hexagonal P6*m* symmetry analogous to NPC. CMK-3 carbon consists of carbon nanorods packed in hexagonal P6*m* symmetry, held in place by disordered, small perpendicular rods that formed in the micropores connecting the mesopore channels of the SBA-15 template. Nitrogen doping of hard templated CMK-3 carbon requires a constituent containing nitrogen to react with the carbon source constituent [15]. In this work we used nitrogen-doped CMK-3 carbon (NCMK-3) purchased from ACS Materials produced using the hard templating method.

Figure 1 shows the nitrogen sorption isotherms and pore distributions of the respective carbon scaffolds. All of the carbon scaffolds exhibit type IV isotherms with the presence of hysteresis, indicative of mesoporosity [16].

In general the shape of the hysteresis loop is representative of pore geometry and uniformity of the pores. Here the NPC geometry samples display type H2 hysteresis loops according to the IUPAC designation [16], signifying regular, ordered pores with some minor deviations from an idealized cylindrical geometry. Figure 2 shows TEM images displaying the well ordered pore channels of the synthesized NPC and NNPC samples.

By contrast, the CMK-3 geometry has an H3 hysteresis loop classification, indicative of slit-like pores. The inset of Figure 1 shows the pore size distribution of the carbon samples calculated using the Barrett, Joyner, and Halenda (BJH) calculation model with data from the adsorption isotherm. The total pore volume was estimated by the quantity adsorbed at a relative pressure (P_s/P_0) of 0.99. NPC and NNPC carbon have distributions of pores centered at 6 and 7.5 nm, respectively, with the indication of numerous micropores below 2 nm present due to the removal of the silicate oligomers by etching in HF acid solution. The distribution is wider for the nitrogen-doped sample most likely caused by inhomogeneity introduced in the structure due to nitrogen addition, but overall displays a good uniformity of the pore sizes. By comparison, the CMK-3 and NC-

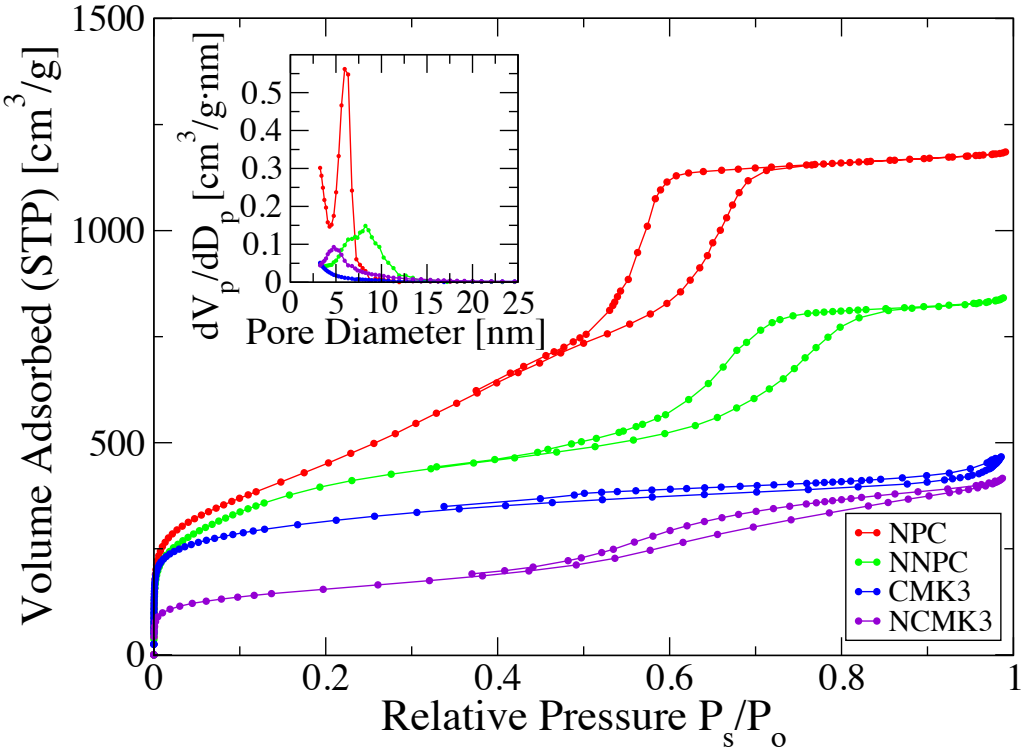

Figure 1. Nitrogen physisorption isotherms and pore distributions for synthesized carbon scaffolds. The CMK-3 curve has been shifted up 25 cc/g for clarity.

MK-3 carbons have distributions centered at 3.5 and 5 nm, respectively, where again the distribution for the doped sample is slightly wider. Table 1 lists the surface areas, total pore volume, and average pore size of the carbon samples obtained from N_2 physisorption measurements. Specific surface area S_{BET} was calculated using the Brunauer-Emmett-Teller (BET) method in a relative pressure range of 0.05 to 0.2.

In order to evaluate the chemical makeup of the carbon substrates, X-ray photoelectron spectroscopy (XPS) scans were recorded. During the scans, a neutralizer was used to mitigate charging effects produced by the ejection of electrons from the sam-

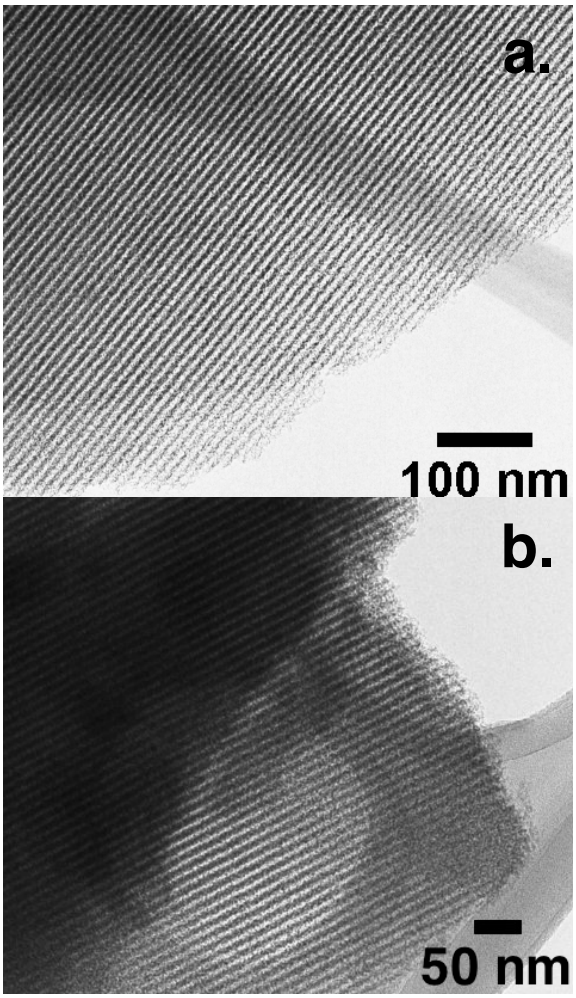

Figure 2. TEM images of synthesized carbons (a) NPC and (b) NNPC showing ordered pore channels.

ple surface. Analysis included a survey spectrum (Supporting Information Figure S1), and detailed scans of the C 1s, O 1s, and N 1s binding energy regions to determine chemical bonding information. A fit was performed on the C 1s spectrum of both doped samples using Gaussian line shapes (Supporting Information Figure S2). The main C 1s peak was fit first and used to constrain the fwhm values of subsequent peaks added to obtain a best fit of the entire C 1s spectrum. Backgrounds were subtracted prior to fitting using the Shirley model. Charge correction of the entire spectrum was performed by

shifting all peaks by the difference in binding energy of the fitted main C 1s peak from that of adventitious carbon at 284.8 eV. Correction values of 0.42 and 0.60 eV were subt-

Table 1. Summary of Carbon Physical Properties Measured with N_2 Physisorption at 77K

sample	pore size[a] [nm]	S_{BET}[b] [m^2/g]	V_T[c] [cm^3/g]
NPC	6.0	1644	1.83
NNPC	7.5	1466	1.31
CMK-3	3.5	1037	0.70
NCMK-3	5.0	520	0.61

[a]Calculated by the BJH method using adsorption branch isotherm data.
[b]Calculated using the BET method in a relative pressure range of 0.05 to 0.2.
[c]Estimated from the amount adsorbed at a relative pressure (P_s/P_0) of 0.99.

racted from all the spectra of NNPC and NCMK-3, respectively. Atomic % concentrations of constituent elements were evaluated from the survey scan using the appropriate relative sensitivity factors (RSF) of the constituents present. Of particular interest for these samples was the atomic % concentration and chemical bonding state of nitrogen. As expected no nitrogen was detected for the NPC or CMK-3 carbon samples. Atomic concentrations of 7.5% and 12.3% were measured in the NNPC and NCMK-3 samples, respectively. In order to obtain chemical bonding information, the N 1s spectrum for both doped samples was deconvoluted into contributions from the different bonding environments using Gaussian line shapes constrained to have the same fwhm values. Figure 3 shows the resulting best fit model for the N 1s spectrum of both doped samples.

Configurations corresponding to four different nitrogen bonding environments were detected in both doped samples. The N 1s spectrum of NNPC displayed peaks

centered at 398.4, 400.2, 401.0, and 402.8 eV, while similarly NCMK-3 contained peaks at 398.3, 400.4, 401.8, and 403.5 eV. Reported literature assigns the first three N 1s binding energy values to pyridinic [17,18], pyrrolic, and quaternary nitrogen environments [18]. The small peak at the higher binding energy is poorly understood [17], but may be due to N-oxides of pyridinic nitrogen [18]. Relative atomic concentrations of each nitrogen type were calculated from the area value each fit peak comprised of the total. Table 2 summarizes the XPS results obtained from the carbon

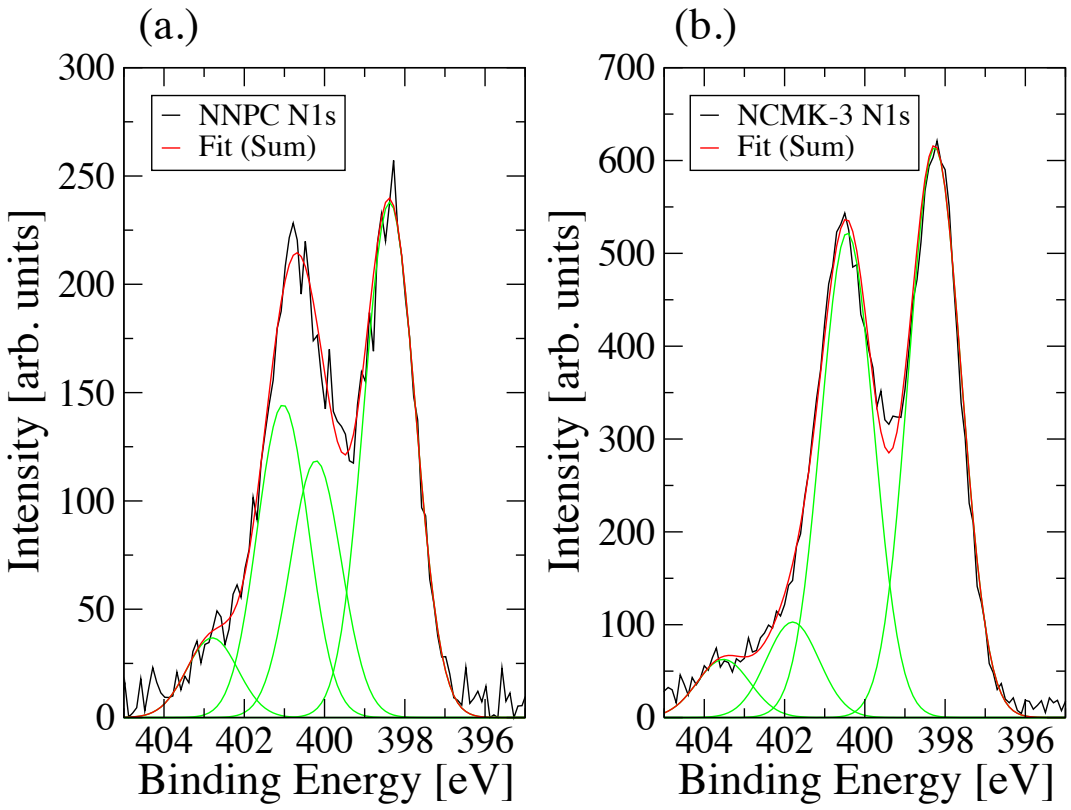

Figure 3. N 1s spectra for (a) NNPC and (b) NCMK-3. The displayed contributions for each sample correspond to four different chemical bonding environments. Pyridinic nitrogen (~398.4 eV) accounted for the largest portion of the spectra in both samples.

samples. For both doped samples, pyridinic nitrogen accounted for the largest part of the N 1s spectrum. In the pyridinic configuration the nitrogen atom is sp2 hybridized, participating in two σ and one π bond with neighboring carbon atoms in the aromatic ring, leaving a lone pair of electrons in an sp2 orbital, allowing the nitrogen to function as a Lewis base.

Table 2. Summary of XPS Measurements for Carbon Substrates

sample	carbon content [atom.%]	nitrogen total [atom.%]	pyridinic nitrogen [atom.%]	pyrrolic nitrogen [atom.%]	quaternary nitrogen [atom.%]	other nitrogen [atom%]
NPC	95.7	-	-	-	-	-
NNPC	87.5	7.5	3.3	1.7	2.0	0.5
CMK-3	98.1	-	-	-	-	-
NCMK-3	81.9	12.3	5.9	5.0	1.0	0.4

The method of melt infiltration (see Experimental section) was used to nano-confine $LiBH_4$ inside the pores of the carbon substrates. A mass of $LiBH_4$ corresponding to 30% pore volume filling was chosen for these experiments, which is well below the maximum loading of ~70% of the pore volume [5]. Here after infiltrated samples are referred to as $LiBH_4$@Carbon (e.g., $LiBH_4$@NPC). Differential scanning calorimetry (DSC) scans (Supporting Information Figure S3) were performed to verify the infiltration of the carbon pores with active material by observing the reduction or elimination of endotherms associated with the LT phase transition and melting of bulk $LiBH_4$ as described in previous publications [4,5]. In addition, a broad endotherm corresponding to decomposition and H_2 release were observed in the DSC scans (Supporting Information Figure S3) at temperatures < 300 °C in agreement with previous studies [4,5], indicating

infiltrated $LiBH_4$ was present in the pores. Powder X-ray diffraction (PXRD) scans (Supporting Information Figure S4) were taken to verify successful pore infiltration. No diffraction peaks were detected for $LiBH_4$, indicating there is little or no $LiBH_4$ exterior to the pores. Together with the DSC scans, this indicates that the infiltration was successful and the confined phase is amorphous, in agreement with previous experimental measurements of confined hydrides in nanoporous carbons [4,5,7-9].

Activation energies for hydrogen release in metal hydrides are commonly measured by taking isothermal desorption rate data at several temperatures, followed by an Arrhenius analysis. Unless the reaction one is studying is known to be a single step, or single mechanism, the results likely depend on the temperature dependence of the pre-exponential, as well as competing mechanisms. The actual decomposition mechanism may be extremely complicated and uniquely determining the pathway can be a formidable challenge [19]. Despite these complications, the analysis provides some insight into processes occurring during hydrogen desorption [20]. Hydrogen desorption from the infiltrated carbon substrates was measured using a custom built Sieverts type apparatus. In this experiment, the sample was contained in a small sample-volume sample holder connected to the larger Sievert's apparatus. With the sample valve closed, the sample is heated to the first set point temperature, 175 °C. The sample valve is then opened to allow desorption. Pressure readings with respect to time were recorded as the sample desorbed hydrogen into a previously evacuated volume. Data was recorded for a period of time < 5 min while maintaining the sample temperature at the experimental set point. The valve was closed, and the temperature was increased to the next set point. The process was repeated in roughly 25 °C increments. The rate of hydrogen desorption was related to temperature through the well-known relation

$$\text{Rate} = \frac{d[H_2]}{dt} = K_0 e^{-\frac{E_A}{RT}} \quad (1)$$

where E_A is the activation energy, K_0 is the pre-exponential rate constant or frequency factor and $[H_2]$ is the concentration of hydrogen gas.

Using the ideal gas law this can be recast into the form

$$\frac{1}{RT}\frac{dP}{dt} = K_0 e^{-\frac{E_A}{RT}} \quad (2)$$

Figure 4 shows the Arrhenius plots of ln(Rate) vs. 1/T for bulk $LiBH_4$ and the respective infiltrated carbon substrates, with lines of best fit calculated by linear regression. In all cases, the correlation coefficients obtained for the data fits were >0.98.

Table 3 lists the activation energies derived from the slope value of $-E_A/R$ obtained from the curves of best fit for each sample. For bulk $LiBH_4$ the activation ener-

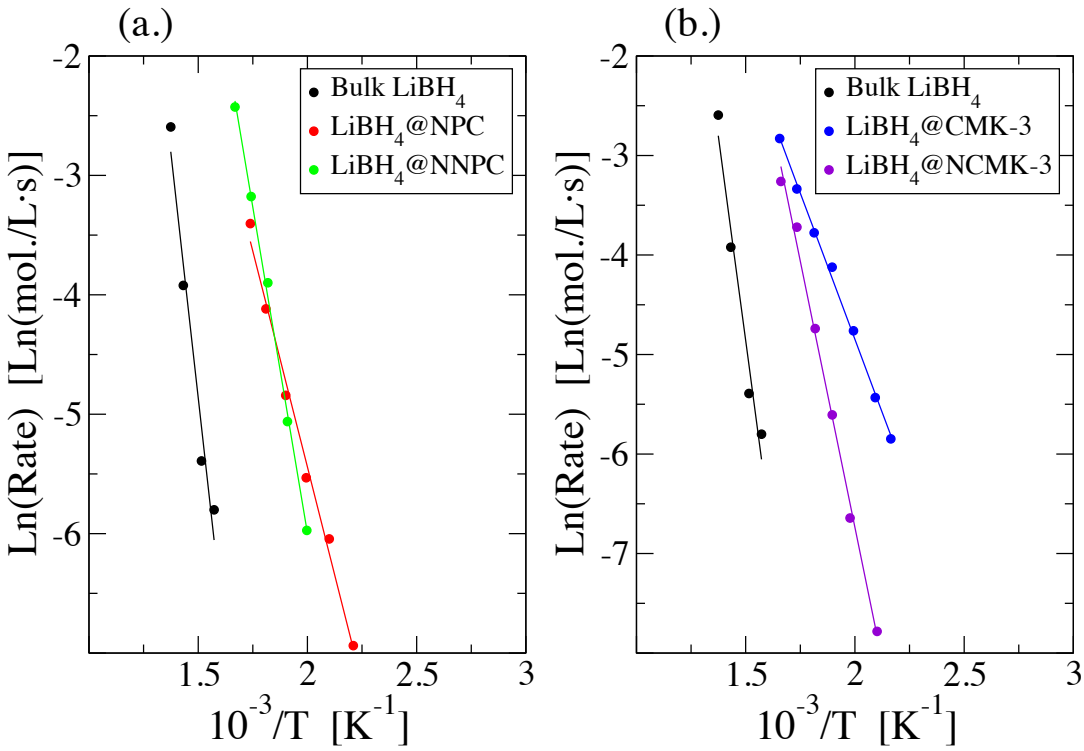

Figure 4. Arrhenius plots for (a) Bulk $LiBH_4$ and $LiBH_4$ infiltrated NPC geometry carbons (b) Bulk $LiBH_4$ and $LiBH_4$ infiltrated CMK-3 geometry carbons. The negative slope of the best fit line is proportional to the activation energy of the sample.

Table 3. Activation Energies Measured by Isothermal Arrhenius Analysis

sample	activation energy [kJ/mol]	relative changes [kJ/mol]
Bulk $LiBH_4$	136.4 ± 18.1	
$LiBH_4$@NPC	60.2 ± 2.8	Δ_{bulk}= –76.2
$LiBH_4$@NNPC	90.8 ± 2.7	Δ_{NPC}= +30.6
$LiBH_4$@CMK-3	48.9 ± 1.2	Δ_{bulk}= –87.5
$LiBH_4$@NCMK-3	89.0 ± 3.3	Δ_{CMK-3}= +40.1

gy is found to be 136.4 kJ/mol and is consistent with the values reported in previous studies [3,21,22]. The larger uncertainty present in the bulk measurement is most likely caused by a multistep decomposition process, where there are the formation of intermediate compounds and the confirmed release of diborane gas [4,5,22]. The reaction process on dehydriding has not been uniquely determined. However, DSC of nanoconfined $LiBH_4$@NPC appears to show desorption in a single step [4,5].

All of the infiltrated samples display decreased activation energies compared to bulk $LiBH_4$. Most interestingly, there is a large difference in $LiBH_4$ activation energy for confinement in a nitrogen doped vs undoped substrate of the same geometry. Activation energies for both bare carbons show a decrease from bulk (Δ_{bulk}) of over –75 kJ/mol. Strikingly, in both cases there is an increase in activation energy in going from bare carbons to N-doped carbons in excess of +30 kJ/mol. Evidently the functionalization of the carbon substrate with nitrogen has a stabilizing effect on the infiltrated $LiBH_4$. First-principles calculations [23] predict a decomposition mechanism for $LiBH_4$ involving the creation of structure vacancies by the removal of $(BH_4)^-$ and/or BH_3 units at the materials surface, allowing H^- species to diffuse into the bulk to act as nucleation sites for the formation of LiH. These calculations also indicate that $(BH_4)^-$ and/or BH_3 must be

transported to the surface in order to sustain the reaction. Further, $(BH_4)^-$ is not stable outside bulk $LiBH_4$ and will decompose to BH_3 and H^-.

In light of these calculations and our experimental results, we propose the stabilization effect observed during our kinetics experiments results from the formation of a capping layer at the surface of the confined bulk $LiBH_4$ from a Lewis acid/base interaction between pyridinic nitrogen contained in the pore wall of the substrate and BH_3 from partial decomposition of $LiBH_4$ during melt-infiltration. Pyridinic nitrogen is able to act as a Lewis base, donating electron density to BH_3 analogous to the formation of the B-N bond in ammonia borane. BH_3 species that would normally be freely released at the hydride surface and be available to form diborane gas are now bound to the pyridinic nitrogen in the pore walls, effectively hindering the decomposition. Formation of the capping layer should make any diborane gas release shift to higher temperatures compared to $LiBH_4$ confined in the undoped substrate.

Following the melt infiltration, the samples, stable at room temperature, were transported without air exposure to a vacuum system equipped with a residual gas analyzer mass spectrometer (RGA-MS) for temperature-programmed desorption (TPD) measurements. Figure 5 shows the background subtracted (Supporting Information) partial pressure of diborane gas as a function of temperature recorded during RGA-MS scans of the NPC type infiltrated samples. The inset of Figure 5 displays hydrogen gas desorption from the samples during the TPD measurements. The initial hydrogen release of the $LiBH_4$@NNPC sample is delayed to higher temperatures by ~30 °C with respect to $LiBH_4$@NPC. The release of hydrogen in the RGA spectrum of the $LiBH_4$@NNPC sample represents desorption from both the $LiBH_4$ in close vicinity of the substrate, likely involved in surface functionalized interactions, in addition to bulk-like $LiBH_4$ at the pore interior. It is difficult to accurately distinguish the contributions of the two groups, though the second significant release at ~200 °C that begins simultaneously in both samples may be due to the bulk-like $LiBH_4$.

Cracking pattern histograms generated from mass spectrum data taken from the NIST Chemistry Webbook were used to positively identify the release of diborane gas for the samples displayed in Figure 5 (Supporting Information Figure S5). The partial

pressure of mass 26 (100% intensity) was used to represent the evolution of diborane gas in Figure 5 due to the low signal-to-noise ratio in the data. Peak diborane release of the $LiBH_4$@NNPC sample occurs at a temperature over 25 °C higher than the undoped sample of the same geometry, providing evidence that a capping layer may have indeed formed. These results suggest that as the sample temperature is increased a point is reached where there is not enough pyridinic nitrogen in the pore walls available to bind all of the releasing BH_3 and/or the nitrogen can no longer maintain its bond to the BH_3. As this occurs the now free BH_3 molecules begin to dimerize into B_2H_6 or decompose further to boron and hydrogen.

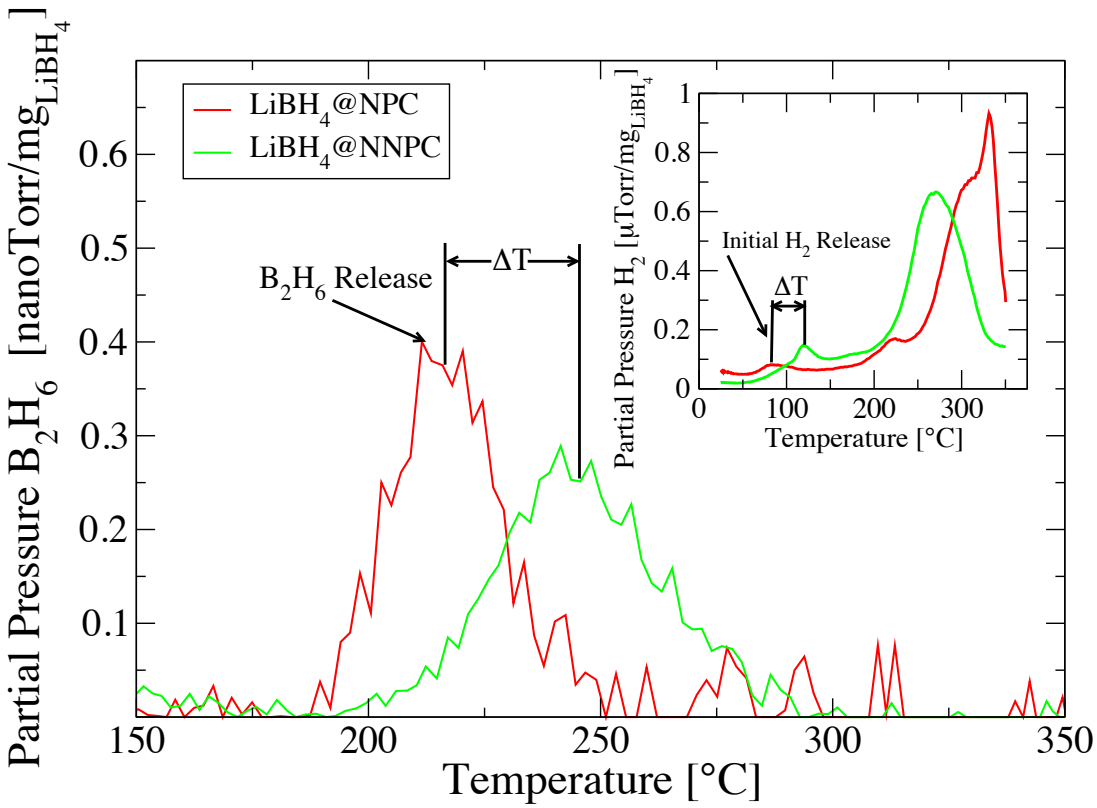

Figure 5. Diborane and H_2 release measured by residual gas analysis mass spectroscopy during temperature-programmed desorption. Initial hydrogen and peak diborane release are delayed for the $LiBH_4$@NNPC sample.

We note that while diborane was detected for the $LiBH_4$@CMK-3 sample (Supporting Information Figure S5), no corresponding release was detected for the $LiBH_4$@NCMK-3 sample. However, the activation energy measurement of $LiBH_4$ confined in NCMK-3 increased 82% with respect to confinement in the undoped substrate, while a more modest 50% increase occurred for the NPC type carbon. This suggests we should see an increased stabilization effect in the CMK-3 type carbons compared to those observed for the NPC systems. Indeed the NCMK-3 sample has nearly double the pyridinic N content of the NNPC sample as shown in the Table 2 XPS results. Further, the infiltrated bare CMK-3 sample releases diborane at a considerably higher temperature (nearly 275 °C) than in the NPC type geometry system (Supporting Info Figure S6), leading us to expect a peak diborane release for the $LiBH_4$@NCMK-3 sample to occur somewhere in excess of 300 °C, but this was not observed. Previous studies of bulk and nanoconfined $LiBH_4$ indicate diborane release is concomitant with decomposition except in substrates with pores less than 4 nm [5], which does not apply to NCMK-3. This suggests that the lack of diborane release might be related to the higher level of substrate doping or it may not form at these higher temperatures when BH_3 is liberated from the bulk surface and/or capping layer and instead decomposes into boron and hydrogen. Future experiments are needed to fully test the effect that the N/C ratio has on the decomposition kinetics and the released species.

4. CONCLUSIONS

We have presented evidence from hydrogen desorption kinetics, XPS, and TPD measurements demonstrating that surface functionalized carbon substrates will stabilize the release of diborane and kinetically stabilize $LiBH_4$ against decomposition to higher temperatures. Our results demonstrate that nitrogen heteroatoms in nanoporous carbon frameworks strongly influence the interface with infiltrated $LiBH_4$, increasing the activation energy for hydrogen desorption by 30 kJ/mol and increasing the diborane release temperature by ~30 °C. Our XPS data shows that a large fraction of the nitrogen is pyridinic, strongly suggesting that the lone pair of electrons is able to effectively solvate BH_3 groups on a surface layer. Unique identification of this interaction is planned

with nuclear magnetic resonance cross-polarization measurements. The resulting capping layer that is likely formed from this Lewis acid/base interaction with $LiBH_4$ should be possible with a much larger class of unstable complex hydrides such as [24] $Ti(BH_4)_4$ and AlH_3 among many others and allow for dramatic improvements in hydrogen storage materials.

ACKNOWLEDGEMENTS

The authors would like to thank B. Porter of the Material Research Center at Missouri University of Science and Technology for his assistance in collecting XPS data, and D. Osborn at the University of Missouri-St. Louis for assistance collecting TEM images. Funding for this work was provided by the University of Missouri through awards from the Research Board (RB) and Interdisciplinary Intercampus (IDIC) Award Committee. Funding for C. Carr was provided through an NSF Integrative Graduate Education Research Traineeship (IGERT) fellowship at the University of Missouri. The authors thank Mark S. Conradi for useful discussions.

REFERENCES

[1] Klebanoff, L. E.; Keller, J. O. 5 Years of Hydrogen Storage Research in the U.S. DOE Metal Hydride Center of Excellence (MHCoE). *Int. J. Hydrogen Energy* **2013**, 38, 4533–4576.

[2] Graetz, J.; Reilly, J. J. Thermodynamics of the α, β and γ Polymorphs of AlH_3 *J. Alloys Compd.* **2006**, 424, 262–265.

[3] Gross, A. F.; Vajo, J. J.; Van Atta, S. L.; Olson, G. L. Enhanced Hydrogen Storage Kinetics of $LiBH_4$ in Nanoporous Carbon Scaffolds. *J. Phys. Chem. C* **2008**, 112, 5651–5657.

[4] Liu, X.; Peaslee, D.; Jost, C. Z.; Majzoub, E. H. Controlling the Decomposition Pathway of $LiBH_4$ via Confinement in Highly Ordered Nanoporous Carbon. *J. Phys. Chem. C* **2010**, 114, 14036–14041.

[5] Liu, X.; Peaslee, D.; Jost, C. Z.; Baumann, T. F.; Majzoub, E. H. Systematic Pore-Size Effects of Nanoconfinement of $LiBH_4$: Elimination of Diborane Release and Tunable Behavior for Hydrogen Storage Applications. *Chem. Mater.* **2011**, 23, 1331–1336.

[6] Lohstroh, W.; Roth, A.; Hahn, H.; Fichtner, M. Thermodynamic Effects in Nanoscale $NaAlH_4$. *ChemPhysChem* **2010**, 11, 789–792.

[7] Gao, J.; Adelhelm, P.; Verkuijlen, M. H. W.; Rongeat, C.; Herrich, M.; van Bentum, P. J. M.; Gutfleisch, O.; Kentgens, A. P. M.; de Jong, K. P.; de Jongh, P. E. Confinement of $NaAlH_4$ in Nanoporous Carbon: Impact on H_2 Release, Reversibility, and Thermodynamics. *J. Phys. Chem. C* **2010**, 114, 4675–4682.

[8] Adelhelm, P.; Gao, J.; Verkuijlen, M. H. W.; Rongeat, C.; Herrich, M.; van Bentum, P. J. M.; Gutfleisch, O.; Kentgens, A. P. M.; de Jong, K. P.; de Jongh, P. E. Comprehensive Study of Melt Infiltration for the Synthesis of $NaAlH_4$ /C Nanocomposites. *Chem. Mater.* **2010**, 22, 2233–2238.

[9] Liu, X.; Peaslee, D.; Majzoub, E. H. Tailoring the Hydrogen Storage Properties of $Li_4BN_3H_{10}$ by Confinement into Highly Ordered Nanoporous Carbon. *J. Mater. Chem. A* **2013**, 1, 3926–3931.

[10] House, S. D.; Liu, X.; Rockett, A. A.; Majzoub, E. H.; Robertson, I. M. Characterization of the Dehydrogenation Process of $LiBH_4$ Confined in Nanoporous Carbon. *J. Phys. Chem. C* **2014**, 118, 8843–8851.

[11] Mason, T.; Majzoub, E. H. Effects of a Carbon Surface Environment on the Decomposition Properties of Nanoparticle $LiBH_4$: A First-Principles Study. *J. Phys. Chem. C* **2014**, 118, 8852–8858.

[12] Liu, R.; Shi, Y.; Wan, Y.; Meng, Y.; Zhang, F.; Gu, D.; Chen, Z.; Tu, B.; Zhao, D. Triconstituent Co-Assembly to Ordered Mesostructured Polymer−Silica and Carbon−Silica Nanocomposites and Large-Pore Mesoporous Carbons with High Surface Areas. *J. Am. Chem. Soc.* **2006**, 128, 11652–11662.

[13] Song, Y.; Li, L.; Wang, Y.; Wang, C.; Guo, Z.; Xia, Y. Nitrogen-Doped Ordered Mesoporous Carbon with a High Surface Area, Synthesized through Organic-Inorganic Coassembly, and Its Application in Supercapacitors. *ChemPhysChem* **2014**, 15, 2084–2093.

[14] Jun, S.; Joo, S. H.; Ryoo, R.; Kruk, M.; Jaroniec, M.; Liu, Z.; Ohsuna, T.; Terasaki, O. Synthesis of New, Nanoporous Carbon with Hexagonally Ordered Mesostructure. *J. Am. Chem. Soc.* **2000**, 122, 10712–10713.

[15] Vinu, A.; Ariga, K.; Mori, T.; Nakanishi, T.; Hishita, S.; Golberg, D.; Bando, Y. Preparation and Characterization of Well-Ordered Hexagonal Mesoporous Carbon Nitride. *Adv. Mater.* **2005**, 17, 1648–1652.

[16] Sing, K. S. W.; Everett, D. H.; Haul, R. A. W.; Moscou, L.; Pierotti, R. A.; Rouquerol, J.; Siemieniewska, T. Reporting Physisorption Data for Gas/Solid Systems with Special Reference to the Determination of Surface Area and Porosity (Recommendations 1984). *Pure Appl. Chem.* **1985**, 57, 603–619.

[17] Gammon, W. J.; Kraft, O.; Reilly, A. C.; Holloway, B. C. Experimental Comparison of N (1s) X-Ray Photoelectron Spectroscopy Binding Energies of Hard and Elastic Amorphous Carbon Nitride Films with Reference Organic Compounds. *Carbon* **2003**, 41, 1917–1923.

[18] Wang, H.; Maiyalagan, T.; Wang, X. Review on Recent Progress in Nitrogen-Doped Graphene: Synthesis, Characterization, and Its Potential Applications. *ACS Catal.* **2012**, 2, 781–794.

[19] Poonyayant, N.; Stavila, V.; Majzoub, E. H.; Klebanoff, L. E.; Behrens, R.; Angboonpong, N.; Ulutagay-Kartin, M.; Pakawatpanurut, P.; Hecht, E. S.; Breit, J. S. An Investigation into the Hydrogen Storage Characteristics of $Ca(BH_4)_2/LiNH_2$ and $Ca(BH_4)_2/NaNH_2$: Evidence of Intramolecular Destabilization. *J. Phys. Chem. C* **2014**, 118, 14759–14769.

[20] Sandrock, G.; Gross, K.; Thomas, G. Effect of Ti-Catalyst Content on the Reversible Hydrogen Storage Properties of the Sodium Alanates. *J. Alloys Compd.* **2002**, 339, 299–308.

[21] Züttel, A.; Rentsch, S.; Fischer, P.; Wenger, P.; Sudan, P.; Mauron, P.; Emmenegger, C. Hydrogen Storage Properties of $LiBH_4$. *J. Alloys Compd.* **2003**, 356-357, 515–520.

[22] Kato, S.; Bielmann, M.; Borgschulte, A.; Zakaznova-Herzog, V.; Remhof, A.; Orimo, S.; Züttel, A. Effect of the Surface Oxidation of $LiBH_4$ on the Hydrogen Desorption Mechanism. *Phys. Chem. Chem. Phys.* **2010**, 12, 10950.

[23] Hoang, K.; Van de Walle, C. G. Mechanism for the Decomposition of Lithium Borohydride. *Int. J. Hydrogen Energy* **2012**, 37, 5825–5832.

[24] Callini, E.; Borgschulte, A.; Hugelshofer, C. L.; Ramirez-Cuesta, A. J.; Züttel, A. The Role of Ti in Alanates and Borohydrides: Catalysis and Metathesis. *J. Phys. Chem. C* **2014**, 118, 77–84.

SUPPORTING INFORMATION

• Introduction to Carbon Preparation Techniques:

There are two primary methods for preparing nanoporous carbons. (1) The soft templating technique that utilizes phenolic resins as the carbon precursor and a triblock-

copolymer such as PEO-PPO-PEO in an organic-organic evaporation induced self-assembly (EISA) [1]. (2) The nanocasting procedure using ordered silicate templates, such as SBA-15, to provide the pore structure, while using sucrose as the carbon precursor [2].

In a typical preparation of soft-templated carbon using triblock-copolymer as the soft template, one prepares a phenolic resin (resols) from a base-catalyzed polymerization of phenol and formaldehyde. The resulting resol precursors and triblock copolymer are dissolved in ethanol and mixed thoroughly. Pouring the mixture into a dish and allowing the ethanol to begin evaporation incites the self-assembly process. Micelles form from the packing of individual triblock-copolymer molecules, in an arrangement that sequesters the hydrophobic PPO blocks to the micelle interior, forming an outer interface layer composed of the hydrophilic PEO blocks. Hydrogen bonding between the abundant hydroxyl (OH^-) groups present in the resol precursors and the PEO blocks incorporates the resol molecules with the micelles. Geometry of the final mesostructure is determined by the ratio of phenol to template material, where increasing the ratio produces micelles with higher curvature. Possible structures include lamellar, body centered cubic and 2D hexagonal. Upon the completion of evaporation, the resulting clear film is heated in an oven at a temperature of 100 ºC for 24 hours to slowly thermopolymerize the material. During the thermopolymerization process the resol precursors cross-link by the formation of covalent bonds between resol molecules at a slow rate induced by the low temperature, which avoids the collapse of the structure formed by the soft template in the assembly process.

Calcination is carried out by heating the material under inert gas to a temperature of 350 ºC for two hours to further cross-link the structure and remove the soft template material through decomposition. At this point in the process the material is mesoporous polymer. Further heating of the material to a temperature >600 ºC under inert gas carbonizes the material resulting in mesoporous carbon. The selected carbonization temperature can reach as high as 1000 ºC and is chosen based on the desired surface area/pore volume of the material. Oxygen in amounts <3% can be added to the inert gas

flow to facilitate the removal of the soft template material and further influence the surface area/pore volumes obtained.

The hard templating or nanocasting method to obtain ordered mesoporous carbon is typically accomplished by selecting an ordered material for use as the template. We have successfully prepared the mesoporous carbon termed [2] CMK-3 using the silicate template SBA-15 that contains cylindrical mesopores arranged in a hexagonal P6*m* symmetry analogous to the 2D hexagonal carbons prepared using the soft templating method. The mesopores of the SBA-15 are impregnated by mixing the template with a solution consisting of sucrose dissolved in water and sulfuric acid. The sulfuric acid assists in the dehydration of the sucrose. The resulting mixture is heated for 6 hours at 100 ºC and then subsequently at 160 ºC for 6 hours in an oven. At this point the sample consisting of brown/black powders contains SBA-15 with pores incompletely filled with partially polymerized sucrose. The sample is again mixed with a solution of the same previous constituents, but in different concentrations. The previous heat treatment cycle is repeated, followed by further heating in a tube furnace under inert gas flow to a temperature of 900 ºC to carbonize the sample. The silicate template is then removed by etching in an HF solution twice overnight. The resulting carbon is the inverse replica of the SBA-15, consisting of carbon rods packed together in a 2D hexagonal P6*m* symmetry. The structure is maintained by a disordered array of smaller perpendicular carbon rods that hold the main large rods in place. These small rods formed from the filling of nanopores that connect the main mesopore channels of the SBA-15 template.

Carbons of both geometries presented can be doped with nitrogen by the addition of dopant containing precursors and the slight modification of the preparation method [3,4]. The doping of hard templated CMK-3 carbon is rather straightforward. A constituent containing nitrogen to react with a carbon source constituent is selected to fill the template. After carbonization and template removal a doped carbon product is obtained. As an example carbon tetrachloride and ethylenediamine can participate in a polymerization reaction and be used to impregnate the pores of a silicate template [3], producing nitrogen doped CMK-3 carbon (NCMK-3). Nitrogen doping via the soft templating method is much more of a challenge due to the necessity of adding species

containing nitrogen to participate in the EISA process. A constituent containing nitrogen and possessing the ability to interact with resol and/or the soft tri-block copolymer template during the assembly process must be chosen. Nitrogen doping can be accomplished by the addition of dicyandiamide to a mixture of resol precursors and triblock copolymer [4]. In addition, higher surface areas and larger pore volumes can be obtained by adding and subsequently acid hydrolyzing tetraethyl orthosilicate (TEOS) [5,6]. The resulting silicate oligomers contain plenty of (OH^-) groups that can hydrogen bond with the PEO block of the triblock copolymer during the assembly process [6] resulting in the co-assembly of silicate oligomers and resol precursors with the micelles formed by the triblock copolymer. Assembled silicate oligomers act to reinforce the pore walls of the polymer during the carbonization process, which without the silica can shrink the framework by >40% [6].

• Experimental Procedures:

Chemicals: Phenol, formalin, TEOS, Pluronic F-127 tri-block copolymer and dicyandiamide were purchased from Sigma-Aldrich and used as received. Deionized water was used in all experiments.

Synthesis of resol precursors: In a typical process 6.1 g of phenol was melted in a shlenk flask at 40 ºC and added to 1.3 g of 20 wt% NaOH solution under stirring. At the end of 10 minutes, 10.5 g of formalin was added at a temperature below 50 ºC dropwise. The resulting mixture was placed in a water bath at 70 ºC under stirring for 80 minutes and then allowed to cool to RT. Using 1N HCl the pH of the solution was adjusted to ~7.0. Water was removed from the solution under vacuum at 45 ºC, producing a gel-like product. Ethanol was added to dissolve the product, producing a 20 wt.% resol-ethanol solution after mixing. The solution was allowed to settle and then poured off into a separate flask, leaving behind the salt from the acid-base neutralization.

NPC produced using inorganic/organic self-assembly method [6]: In a typical process to produce 2D hexagonal carbon, 16 g F-127 tri-block copolymer was added to a solution consisting of 80 g ethanol and 10 g .2M HCl. After stirring for 1 hour at 40 ºC, 20.8 g TEOS and 50 g of 20 wt.% resol/ethanol solution were added sequentially,

followed by stirring for 2 hours at 40 ºC. The solution was poured into a glass pan and allowed to evaporate overnight at R.T., producing a transparent film. In order to thermopolymerize the sample, heat treatment at 100 ºC was carried out in an oven for 24 hours. The sample was scraped from the pan, ground into a fine powder, and placed into a tube furnace under flowing nitrogen for calcination at 350 ºC for 3 hours, followed by carbonization at 900 ºC for 2 hours. During the heat treatment the ramp rate was 1 ºC/min below 600 ºC and 5 ºC/min after. To remove the silicate the sample was etched in 5 wt.% HF solution overnight twice under stirring, followed by washing with ethanol and deionized water.

NNPC produced using inorganic/organic self-assembly method [5]: In a typical process 8 g of F-127 tri-block co-polymer and 7.5 g dicyandiamide are added to a solution consisting of 100 g ethanol, 50 g H_2O, and 10 g .2M HCl. After stirring for 1 hour at 40 ºC, 10.4 g TEOS and 25 g of 20 wt.% resol/ethanol solution were added sequentially, followed by stirring for an additional 2 hours at 40 ºC. In order to evaporate the solvent, the mixture was poured into pans and placed in an oven at 45 ºC for 8 hours resulting in the formation of uniform films. In order to thermopolymerize the sample, heat treatment at 100 ºC was carried out in an oven for 24 hours. The sample was scraped from the pan, ground into a fine powder, and placed into a tube furnace under flowing nitrogen for calcination at 250 ºC for 2 hours, followed by carbonization at 700 ºC for 3 hours. During the heat treatment the ramp rate was 1 ºC/min. To remove the silicate the sample was etched in 5 wt.% HF solution overnight twice under stirring, followed by washing with ethanol and deionized water.

CMK-3 produced using the nanocasting method [2]: In a typical synthesis 6.25 g sucrose was dissolved in a mixture consisting of .7 g H_2SO_4 and 25 g H_2O, followed by the addition of 5 g SBA-15 silicate hard template material. After 15 minutes of stirring a uniform white slurry was obtained. Heat treatments of the sample at 100 ºC for 6 hours and 160 ºC for 6 hours were performed sequentially. The resulting black/brown powder sample was added to a solution consisting of 4 g sucrose dissolved in .45 g H_2SO_4 and 25 g H_2O. After 25 minutes of stirring the previous heat treatments were repeated, followed by carbonization of the sample in a tube furnace at 900 ºC under flowing argon for 3

hours. During the heat treatment the ramp rate was 1 ºC/min below 600 ºC and 5 ºC/min after. To remove the hard silicate template the sample was etched in 5 wt.% HF solution overnight twice under stirring, followed by washing with ethanol and deionized water.

• XPS Supporting Information:

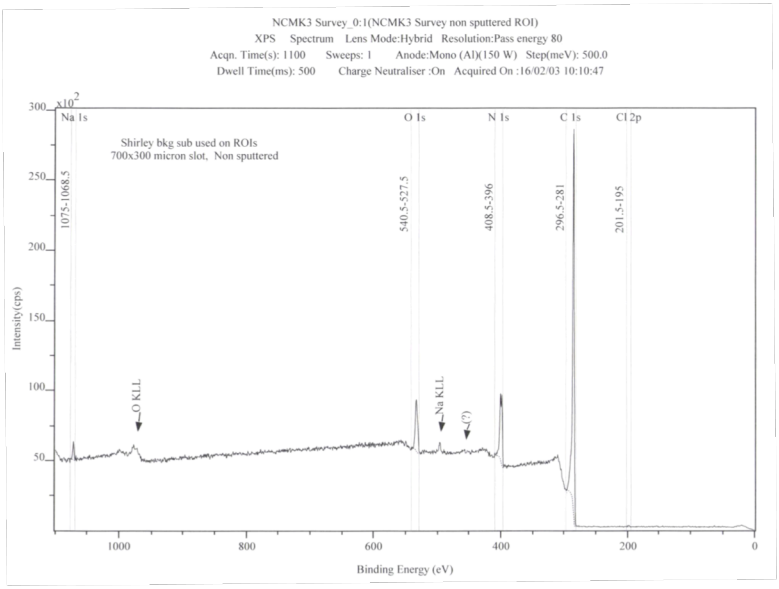

Figure S1a. XPS Survey Spectrum of NCMK-3 Carbon Sample.

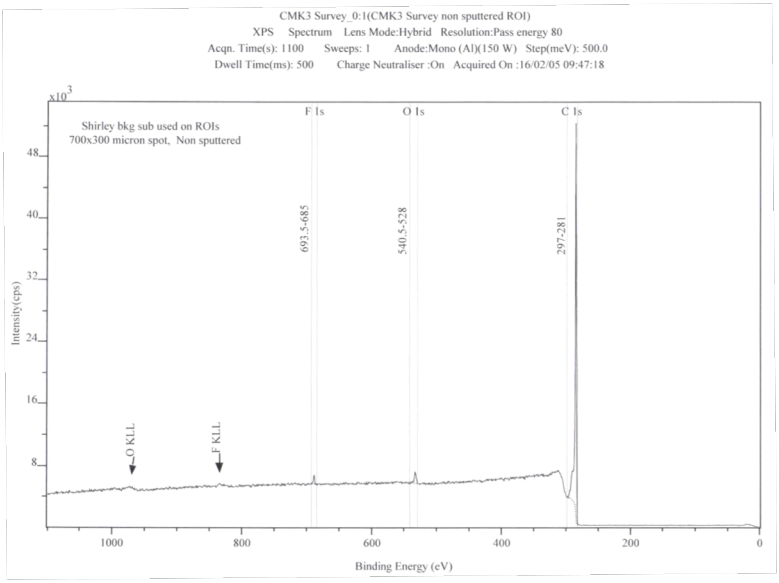

Figure S1b. XPS survey spectrum of CMK-3 sample.

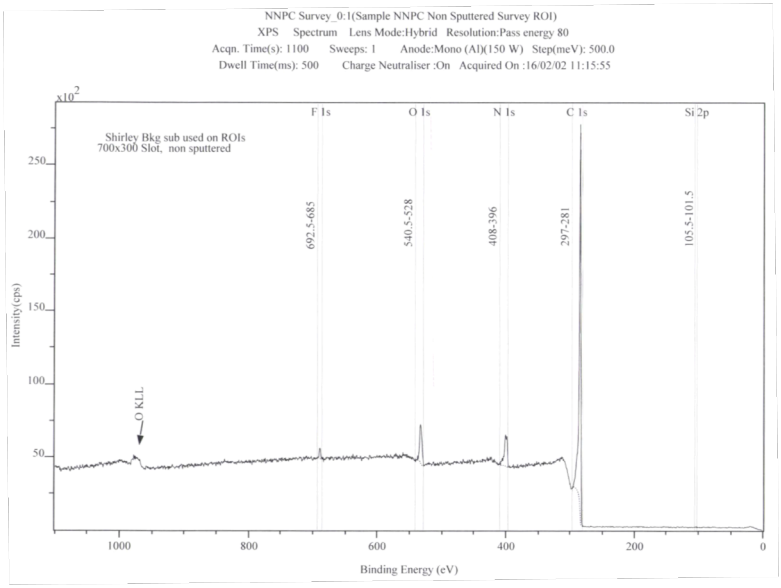

Figure S1c. XPS survey spectrum of NNPC sample.

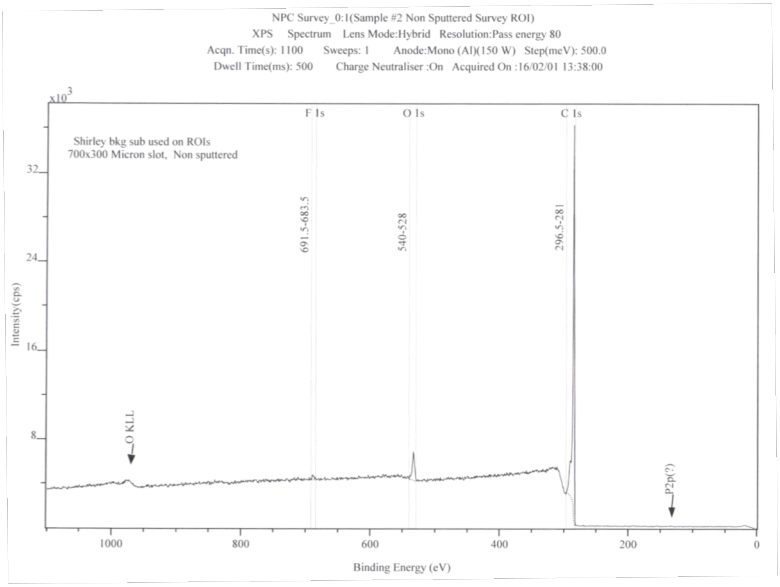

Figure S1d. XPS survey spectrum of NPC carbon sample.

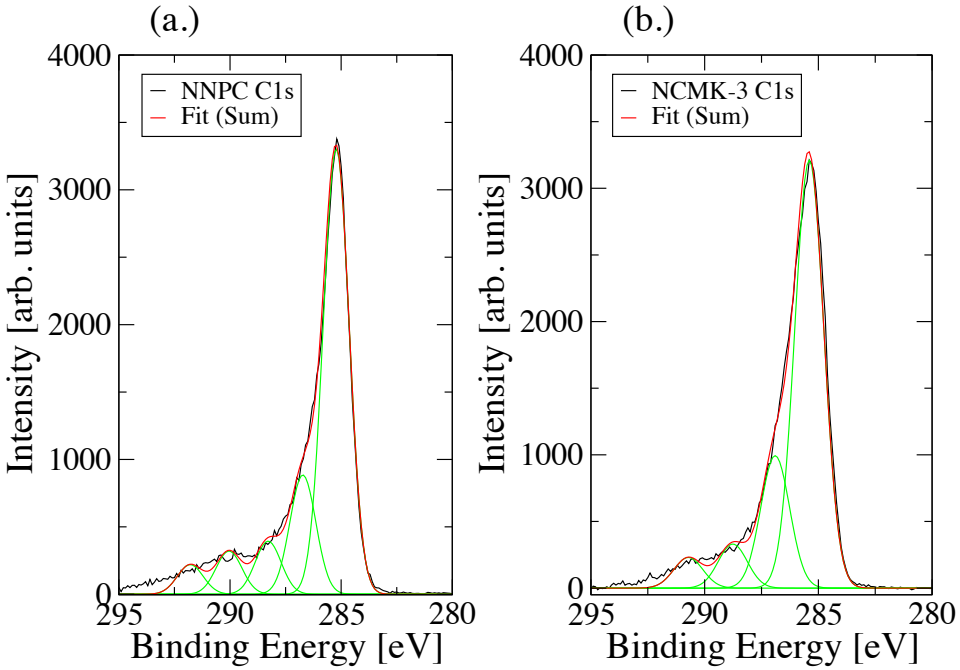

Figure S2. Fit to raw C1s spectrum data used for charge correction of (a.) NNPC and (b.) NCMK-3.

• Differential Scanning Calorimetry:

Scans were taken on a Perkin-Elmer DSC 7 under flowing nitrogen purge gas. Samples were prepared in an argon filled glovebox (O_2 < 1ppm) by placing ~2mg of sample in Perkin Elmer hermetically sealed sample pans. The samples were transported to and loaded into the DSC 7 without air exposure. Immediately before closing the cover and initiating the scan a small hole was poked in the hermetic lid to allow gas escape during the heating process. The heating rate was 20 C/min.

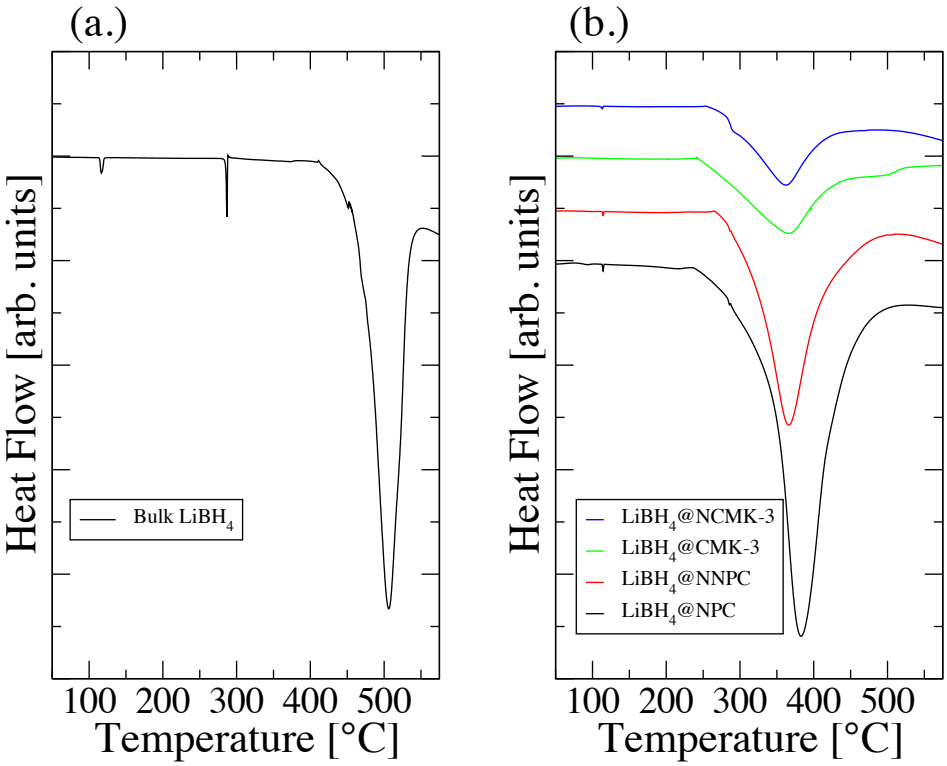

Figure S3. DSC scans of (a.) Bulk $LiBH_4$ and (b.) infiltrated carbon samples. The infiltrated samples do not display the melt endotherm characteristic of bulk $LiBH_4$ just before 300 C. Peak hydrogen desorption temperatures are reduced significantly for the infiltrated carbons. Exothermic heat flow is up in the plots.

• PXRD Scans:

Scans were recorded on a Rigaku Ultima IV X-ray diffractometer with a Cu Kα radiation source. Samples were placed on holders and covered with sealed Mylar film in an argon glovebox to avoid sample air exposure during the PXRD scans.

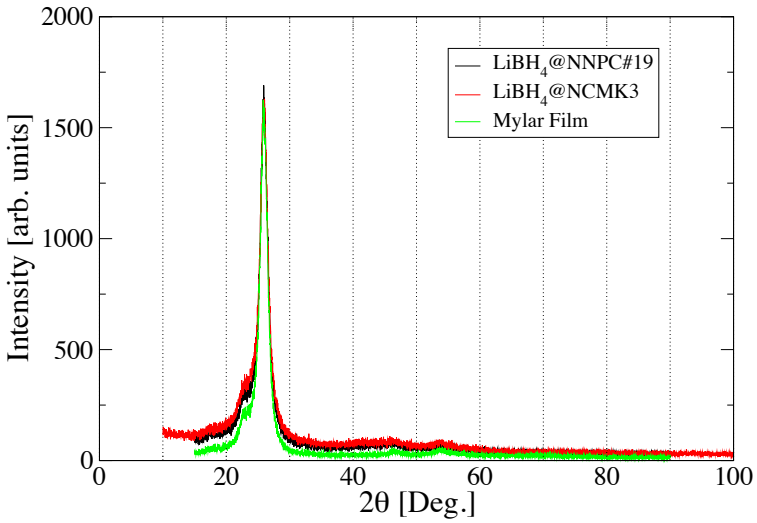

Figure S4. PXRD scans of infiltrated carbon samples. Mylar film was used to cover the sample to avoid air exposure. No peaks from crystalline $LiBH_4$ were detected, indicating the infiltrated material is amorphous.

• RGA-MS Supporting Information:

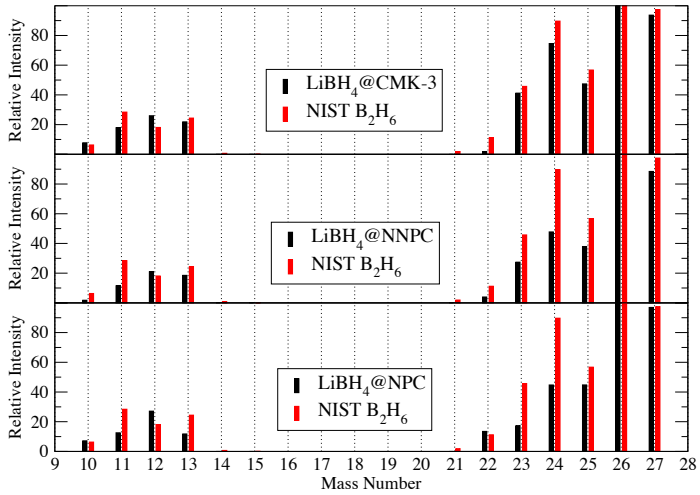

Figure S5. Cracking pattern histograms used to identify diborane gas release from infiltrated samples during RGA-MS measurements.

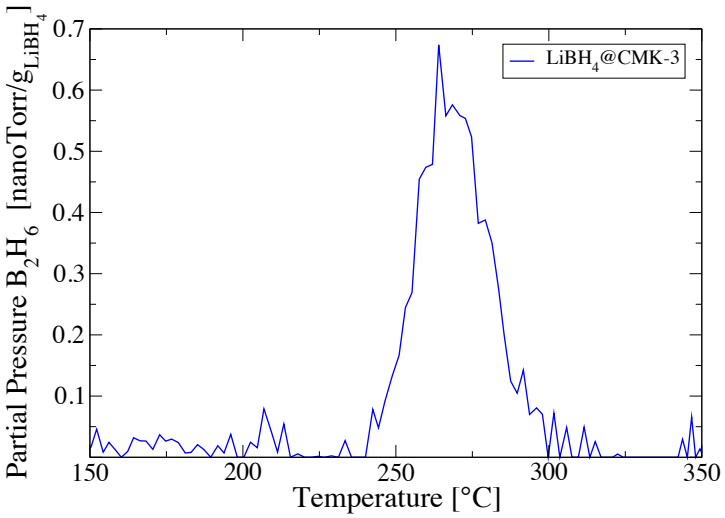

Figure S6. Diborane release measured by residual gas analysis mass spectroscopy during temperature programmed desorption for $LiBH_4$@CMK-3.

RGA scan background subtraction: Before running any RGA sample scans a background spectra was recorded for the empty chamber under the same experimental conditions used during sample runs. The purpose of this run is to sample the state of the chamber vacuum, identifying normally occurring background species such as CO_2, CO, N_2, etc. and record how the partial pressure of each species changes under experimental conditions in the differentially pumped environment. In this work samples were heated from R.T. to 350 C at a ramp rate of 8 C/min. After a sample run is recorded background subtraction is performed using the background spectra scan as a guide. For the sample run the curve of the background species will have relatively the same shape except at regions where the sample released substantial amounts of that particular species. Even if the sample does not release any amount of a particular species present in the background the sample scan will be slightly shifted due to chamber pressure differences caused by the sample releasing other gas species not present in the background scan. Using the background spectra as a guide for each particular mass the background of the sample scan is subtracted by the use of a spline function in a curve-fitting program. Figure S7 shows (top) a chamber background scan for mass 26, (middle) the spectra of mass 26 from the sample run, and (bottom) the mass 26 spectra after performing the background subtraction as outlined above.

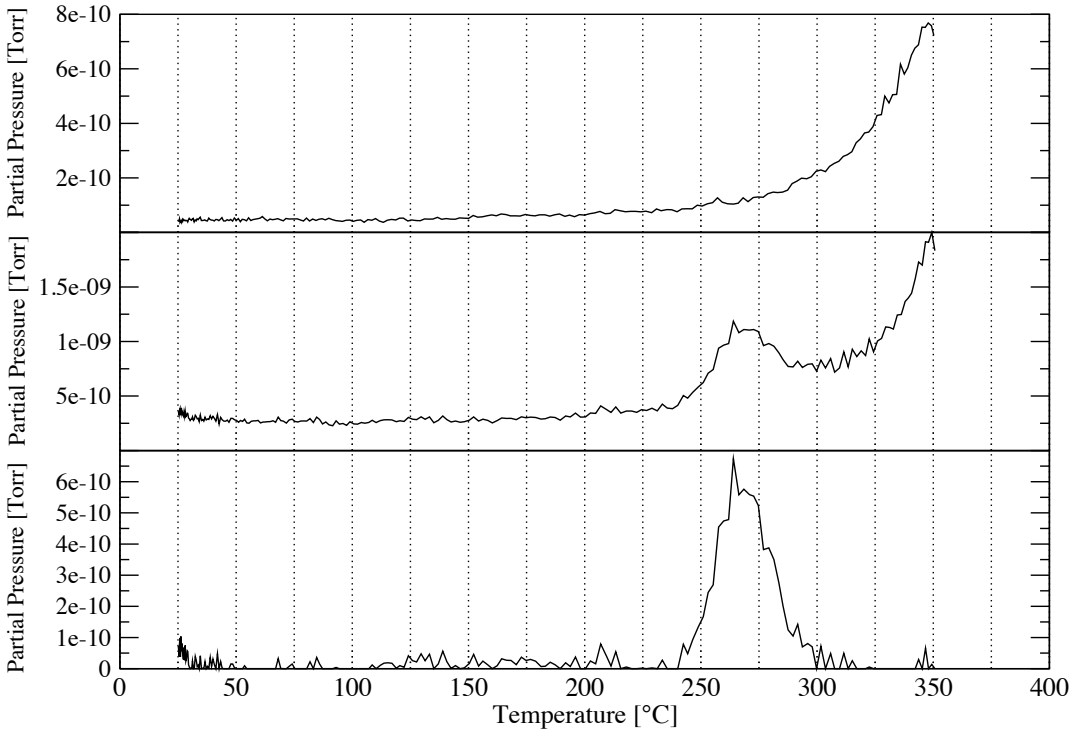

Figure S7. (Top) Mass 26 spectra from empty chamber background scan over experimental conditions, (Middle) mass 26 spectra from $LiBH_4$@CMK-3 sample run, and (Bottom) mass 26 spectra from $LiBH_4$@CMK-3 sample run with background subtracted using outlined procedure.

• References:

[1] Meng, Y.; Gu, D.; Zhang, F.; Shi, Y.; Cheng, L.; Feng, D.; Wu, Z.; Chen, Z.; Wan, Y.; Stein, A.; *et al.* A Family of Highly Ordered Mesoporous Polymer Resin and Carbon Structures from Organic−Organic Self-Assembly. *Chem. Mater.* **2006**, 18, 4447–4464.

[2] Jun, S.; Joo, S. H.; Ryoo, R.; Kruk, M.; Jaroniec, M.; Liu, Z.; Ohsuna, T.; Terasaki, O. Synthesis of New, Nanoporous Carbon with Hexagonally Ordered Mesostructure. *J. Am. Chem. Soc.* **2000**, 122, 10712–10713.

[3] Vinu, A.; Ariga, K.; Mori, T.; Nakanishi, T.; Hishita, S.; Golberg, D.; Bando, Y. Preparation and Characterization of Well-Ordered Hexagonal Mesoporous Carbon Nitride. *Adv. Mater.* **2005**, 17, 1648–1652.

[4] Wei, J.; Zhou, D.; Sun, Z.; Deng, Y.; Xia, Y.; Zhao, D. A Controllable Synthesis of Rich Nitrogen-Doped Ordered Mesoporous Carbon for CO_2 Capture and Supercapacitors. *Adv. Funct. Mater.* **2013**, 23, 2322–2328.

[5] Song, Y.; Li, L.; Wang, Y.; Wang, C.; Guo, Z.; Xia, Y. Nitrogen-Doped Ordered Mesoporous Carbon with a High Surface Area, Synthesized through Organic-Inorganic Coassembly, and Its Application in Supercapacitors. *ChemPhysChem* **2014**, 15, 2084–2093.

[6] Liu, R.; Shi, Y.; Wan, Y.; Meng, Y.; Zhang, F.; Gu, D.; Chen, Z.; Tu, B.; Zhao, D. Triconstituent Co-Assembly to Ordered Mesostructured Polymer−Silica and Carbon−Silica Nanocomposites and Large-Pore Mesoporous Carbons with High Surface Areas. *J. Am. Chem. Soc.* **2006**, 128, 11652–11662.

II. ANOMALOUS H_2 DESORPTION RATE OF $NaAlH_4$ CONFINED IN NITROGEN-DOPED NANOPOROUS CARBON FRAMEWORKS

Christopher L. Carr,[†] Waruni Jayawardana,[†] Hongyang Zou,[§] James L. White,[∥] Farid El Gabaly,[∥] Mark S. Conradi[§,⊥], Vitalie Stavila,[∥] Mark D. Allendorf,[∥] and Eric H. Majzoub[*,†,‡]

[†]Center for Nanoscience and Department of Physics and Astronomy and [‡]Department of Chemistry and Biochemistry, University of Missouri-Saint Louis, One University Boulevard, Saint Louis, Missouri 63121, United States

[§]Department of Physics, Washington University, One Brookings Drive, Saint Louis, Missouri 63130, United States

[∥]Sandia National Laboratories, Livermore, California 94550, United States

[⊥]ABQMR Inc., Albuquerque, New Mexico 87106, United States

Reproduced with permission from *Chem. Mater.* DOI: 10.1021/acs.chemmater.8b00305,

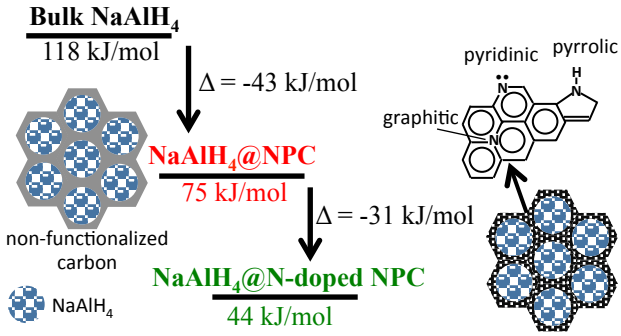

Table of contents graphic from published paper.

ABSTRACT

Confining $NaAlH_4$ in nanoporous carbon scaffolds is known to alter the sorption kinetics and/or pathways of the characteristic bulk hydride reactions through interaction with the framework at the interface, increased specific surface area of the resulting nanoparticles, decreased hydrogen diffusion distances, and prevention of phase segregation. Although the nanosize effects have been well studied, the influence of the carbon scaffold surface chemistry remains unclear. Here we compare the hydrogen sorption characteristics of $NaAlH_4$ confined by melt infiltration in nitrogen-doped/undoped ordered nanoporous carbon of two different geometries. ^{23}Na and ^{27}Al MAS NMR, N_2 sorption, and PXRD verify $NaAlH_4$ was successfully confined and remains intact in the carbon nanopores after infiltration. Both the N-doped/undoped nano-confined systems demonstrate improved reversibility in relation to the bulk hydride during hydrogen desorption/absorption cycling. Isothermal kinetic measurements indicate a lowering of the activation energy for H_2 desorption by as much as 70 kJ/mol in N-doped frameworks, far larger than the reduction in carbon-only frameworks. Most interestingly, this dramatic lowering of the activation energy is accompanied by an unexpected and anomalously low $NaAlH_4$ desorption rate in the N-doped frameworks. This suggests that the framework surface chemistry plays an important role in the desorption process and that the rate limiting step for desorption may be associated with interactions of the hydride and host surface. Our results indicate that functionalization of carbon scaffold surface chemistry with heteroatoms provides a powerful method of altering the characteristic hydrogen sorption properties of confined metal hydride systems. This technique may prove beneficial in the path to a viable metal hydride-based hydrogen storage system.

1. INTRODUCTION

In recent years, confining metal hydrides within porous scaffolds has been established as a useful method of favorably modifying the hydrogen sorption characteristics of the hydride relative to the bulk material. Studies of confined metal

hydrides have reported enhanced desorption kinetics [1-10], improved reversibility [1,3-5,8-10], and, in some instances, altered system thermodynamics [5]. Despite these improvements and extensive search efforts to identify an ideal material, no complex metal hydride systems have been identified that meet all the Department of Energy specifications for onboard hydrogen storage applications [11]. In general, of the complex metal hydrides available, the enthalpy of hydrogen desorption ($\Delta H°$) is either too high (e.g., $LiBH_4$) or too low (e.g., AlH_3) to provide adequate hydrogen pressures (~1–10 bar) for proton exchange membrane fuel cells (PEMFC) operating at a temperature of roughly 80 °C, and/or the hydride is not reversible under modest conditions.

Porous substrates are able to alter hydrogen cycling of confined hydrides by utilizing the large surface-area-to-volume ratio and shifting the surface/interface energies facilitated by the scaffolds. Studies of $LiBH_4$ confined in nanoporous carbon (NPC) have indicated that, during melt infiltration of $LiBH_4$ into the scaffold, the interaction of the molten hydride with the scaffold inadvertently dopes the carbon surface with boron, resulting in a favorable energy for $LiBH_4$ to wet the carbon nanopores [12]. Additionally, neutron scattering and NMR studies of $LiBH_4$ confined within nanoporous carbon and silica scaffolds found that the layer of confined hydride in closest proximity to the pore walls of the scaffolds exhibited rapid reorientations [13-15] or enhanced translational diffusion [16,17] of BH_4^- anions compared to a more bulk-like slower population at the pore interior, suggesting the scaffold must alter the local potential of the anions through either induced lattice strain or electronic effects due to the chemical makeup of the scaffold.

The role of the scaffold chemistry in altering the observed hydrogen sorption properties of the confined metal hydride is less clear. Until recently, there has not been much work aimed at specifically investigating the chemical aspect of the scaffold's influence [15,18]. A study by our group indicated that functionalizing the surface of a nanoporous carbon scaffold with nitrogen heteroatoms can stabilize $LiBH_4$ kinetically, increasing the activation energy for hydrogen desorption by ~30 kJ/mol H_2 in relation to a comparative nonfunctionalized carbon scaffold [18]. Moreover, Suwarno and co-workers [16] studied the influence of scaffold chemistry by confining $LiBH_4$ in carbon

and silica scaffolds of similar pore size, showing the $LiBH_4$ confined in the silica scaffold exhibited a thicker layer of nonbulk-like $LiBH_4$ at the scaffold/hydride interface and a larger depression of the solid-solid phase transition than the carbon based system, together indicating that the chemical nature of the scaffold plays an important role in confined hydride systems.

Here, we report on the modified hydrogen storage properties observed for $NaAlH_4$ confined in nanoporous carbon surface functionalized with nitrogen heteroatoms with respect to a similar nonfunctionalized system. Since the initial work by Bogdanović et al. describing the use of $NaAlH_4$ as a hydrogen storage medium [19], $NaAlH_4$ has been perhaps the most studied complex metal hydride. Considerable attention has been focused on $NaAlH_4$ confined in nanoporous scaffolds. For this reason, $NaAlH_4$ naturally presents itself as an ideal system to test the effect that modifying nanoporous carbon surface chemistry has on the hydrogen storage properties of confined $NaAlH_4$ compared to a base nonfunctionalized system that is relatively well studied. In the present work, matched pairs of nitrogen functionalized/nonfunctionalized carbon scaffolds of two different geometries were used. Our results indicate the activation energy for hydrogen desorption is lowered by more than ~20 kJ/mol H_2 in the nitrogen functionalized systems of both geometries. Despite the lowered activation energies for hydrogen desorption, an anomalous hydrogen desorption bottleneck occurs for the nitrogen functionalized systems in the high temperature region, indicating that the presence of nitrogen may restrict the formation of H_2 at the hydride/scaffold interface in this region.

2. EXPERIMENTAL SECTION

Chemicals/Materials: $NaAlH_4$ (93%), pentane, and THF were purchased from Sigma-Aldrich. Nanoporous carbon (NPC), nitrogen-doped nanoporous carbon (NNPC), CMK-3 type porous carbon, and nitrogen doped CMK-3 (NCMK-3) were synthesized using published literature methods [20-23]. Detailed synthesis procedures are provided in the Supporting Information.

$NaAlH_4$ Purification: Before use, 7.5 g of the as-received $NaAlH_4$ was dissolved in 400 mL of freshly dried/distilled THF. After stirring for 4 h, the insoluble impurities

were allowed to precipitate from the solution. The supernatant was transferred to a separate flask, where the solution was concentrated to a volume of ~125 mL under vacuum. Under stirring, 375 mL of dried/distilled pentane was added to the solution, separating $NaAlH_4$ from the solution as a fine precipitate. After removal of the supernatant, $NaAlH_4$ was washed using ~100 mL of dried/distilled pentane. $NaAlH_4$ in the form of a fine white powder was obtained after drying under vacuum. All operations were carried out using Schlenk line techniques.

Melt Infiltration of $NaAlH_4$ into Carbon Scaffolds: The synthesized carbon scaffolds were infiltrated with $NaAlH_4$ using a custom-built Sieverts-type apparatus. The system consists of a cylindrical stainless-steel sample holder (Setaram) equipped with a manual valve allowing samples to be loaded in an argon filled glovebox (O_2 < 1 ppm) and transported to the apparatus without air exposure. The system manifold consists of calibrated volumes of different capacities, with connection ports for vacuum, H_2, and He gas. Manifold pressures are monitored with two calibrated pressure transducers (MKS model 870B). Sample and manifold temperatures were monitored using type K thermocouples. Pressures and temperatures were recorded with data acquisition software on an interfaced computer. Samples are heated using a cylindrical resistive heating element that fits around the outside of the sample holder connected to a PID controller. The sample holder/heating element is wrapped in an insulating glass fiber blanket to minimize heat flow to the surrounding environment during the heating process.

Prior to infiltration, the substrate materials were dried under dynamic vacuum overnight at 300 °C. Samples were prepared by mixing $NaAlH_4$ in proportion with the respective carbon scaffold to produce a 20 wt % $NaAlH_4$ physical mixture (1.5 wt % H_2 w.r.t. the total sample mass). Mixing was carried out with a mortar and pestle for 10 min, followed by loading into an Al foil roll and placing into a stainless-steel sample holder equipped with a manual valve. All sample handling was performed in an argon-filled glovebox (O_2 < 1 ppm). Samples were transported to the Sieverts apparatus without air exposure, where they were placed under 190 bar H_2 pressure and heated to 200 °C (~15 °C above the melting point of $NaAlH_4$), reaching a final pressure of 205 bar. Following a dwell period of 45 min at 200 °C, the samples were allowed to cool under pressure.

Hydrogen Cycling/Kinetics Measurements: Using the described Sieverts apparatus, isothermal kinetics measurements and Arrhenius analyses were performed on the four composite samples to determine the activation energies of hydrogen desorption. The hydrogen evolution rates were recorded under isothermal conditions in temperature increments of ~10 °C. From room temperature the samples were heated initially to a temperature of 100 °C at an average ramp rate of 20 °C /min using the previously described PID controlled heating element, where the system was briefly evacuated ($P < 1.5 \times 10^{-3}$ MPa). As the samples evolved hydrogen during a 5 min dwell period into the evacuated static vacuum of the Sieverts apparatus, the pressure within the volume was recorded as a function of time. Deviations of the temperature from the desired set point during the dwell period were <1 °C. At the end of the dwell period, the samples were heated to the next set point at an average ramp rate of 8 °C/min, and the process was repeated. At each respective temperature, the rate was determined from the change in pressure. Pressure changes with respect to time exhibited linear behavior over the measured time period, with correlation coefficients exceeding 0.98. The rate of hydrogen desorption can be related to the temperature of the sample through the Arrhenius equation:

$$\text{rate} = \frac{d[H_2]}{dt} = K_0 e^{-\frac{E_A}{RT}} \quad (1)$$

where K_0 is the pre-exponential rate constant or frequency factor, E_A is the activation energy, and $[H_2]$ is the concentration of hydrogen. In the form presented, the equation describes the temperature dependence of the H_2 desorption rate for a single step process.

Following the isothermal kinetics measurements, the samples were heated to 250 °C from the final measurement temperature at a ramp rate of 4 °C/min and held at that temperature until desorption ceased (~1 h). Sample rehydriding was carried out at 150 °C under 180 bar of H_2 for 15 h. To ensure repeatability, the isothermal kinetics measurements were repeated a second time using the rehydrided samples. After a second

rehydriding cycle, desorption of hydrogen from the composite samples into a carefully measured static volume was recorded at a linear ramp rate of 4 °C/min up to 300 °C.

Characterization Measurements: N_2 sorption isotherms were recorded using a SA3100 (Coulter) analyzer at 77 K. Before analysis, the bare carbon samples were outgassed at 300 °C for 10 h, and the infiltrated carbon samples outgassed at 40 °C for 30 min. Samples were loaded into glass analysis vessels in an argon filled glovebox (O_2 < 1 ppm) and transported to the analyzer without air exposure. The specific surface area S_{BET} was calculated using the Brunauer-Emmett-Teller (BET) method in a relative pressure range of 0.05 to 0.2. Pore size distributions and total pore volume were calculated using the Barrett, Joyner, and Halenda (BJH) calculation model using data from the adsorption isotherm. The total pore volume was estimated by the amount adsorbed at a relative pressure (P_s/P_0) of 0.99. Powder X-ray diffraction (PXRD) measurements were acquired using a Rigaku Ultima IV X-ray diffractometer with a Cu K_α radiation source. Samples containing hydrides were sealed using Mylar film in an argon filled glovebox (O_2 < 1 ppm) to prevent air exposure during measurements. For nuclear magnetic resonance (NMR) studies, samples were packed into 5 mm OD pencil rotors inside an argon glove box (O_2 < 1 ppm). The packed rotors were transported without air exposure. N_2 gas boil-off from a liquid nitrogen dewar supplied pure N_2 gas for the bearing and drive gas needed to spin the rotors, thus inhibiting air-related degradation of the samples. Magic angle spinning (MAS) NMR measurements were performed using a home-built spectrometer and Chemagnetics probe on a 7.04 T superconducting magnet. All MAS measurements were made at room temperature with a spinning frequency, f_S, of 5 kHz. X-ray photoelectron spectroscopy (XPS) was performed under UHV conditions (residual pressure better than 1×10^{-8} Torr) using a Physical Electronics 10-360 electron energy analyzer and an Omicron DAR400 Al K-alpha (photon energy = 1487 eV) or Mg K-alpha (photon energy = 1254 eV) X-ray source. Dried samples were embedded in a piece of indium foil to avoid ambiguous quantitation from a carbon support. All XPS peaks were baseline corrected using a Shirley background, and synthetic peaks of mixed Gaussian-Lorentzian (70%/30%) line-shape were used to fit the spectra. Spectra were calibrated to the main C 1s peak at 284.5 eV.

3. RESULTS

Characterization of $NaAlH_4$ in Nanoporous Carbon Frameworks. In this work, nitrogen functionalized and nonfunctionalized carbon scaffolds of two different geometries were employed: (1) ordered mesoporous carbon (CMK-3, NCMK-3) produced via the nanocasting method using a SBA-15 silica template [22,23] and (2) nanoporous carbon (NPC, NNPC) synthesized by the organic-inorganic evaporation-induced self-assembly method [20,21], resulting in carbon consisting of cylindrical nanopore channels in a 2D hexagonal arrangement displaying P6*m* symmetry. Similarly, the SBA-15 silica template contains cylindrical mesopore channels in the P6*m* symmetry as well, with an additional network of smaller disordered micro channels connecting the main mesopores. Nanocasting results in carbon scaffolds with an inverse geometry of the SBA-15 template, consisting of ordered cylindrical nanorods in P6*m* symmetry held in place by nanofibrils formed from the disordered micropore array interconnecting the SBA-15 mesopores. Since SBA-15 and NPC share a common geometry and symmetry of their main pore channels, CMK-3 is inverse to NPC, with the voids between the rods, somewhat slit-like in nature, acting as the mesopores of the CMK-3 type carbon.

Figure 1 displays the isotherms and pore distributions (inset) obtained from nitrogen sorption measurements of the prepared carbon scaffolds at 77 K. All of the scaffolds exhibit type IV isotherms, in addition to hysteresis, indicative of the existence of mesoporosity [24]. As adsorption proceeds in the low relative pressure region, the micropores are filled with adsorbate following monolayer and some multilayer adsorption. In Figure 1 this corresponds roughly to the region where $P_s/P_0 < 0.1$. The increase in relative pressure in the region above 0.1 to the start of each sample's respective hysteresis loop can be mostly attributed to multilayer adsorption along the mesopore walls preceding capillary condensation. Hysteresis is generally indicative of sample mesoporosity [24], with the loop onset shape relating to the size and shape of the mesopores. Onset of capillary condensation corresponding to the sharp increase in adsorbed volume on the adsorption branch of the isotherm occurs at a relative pressure of ~0.4 in the NCMK-3/CMK-3 carbons. In contrast, the NNPC/NPC carbons display a sharp adsorbed volume increase at slightly higher relative pressures in the range 0.45-0.5,

an indication of slightly larger mesopores. According to the IUPAC classifications [24], the NNPC/NPC carbons most closely resemble type H2 hysteresis loops, though the parallel arrangement of the adsorption/desorption isotherms over a considerable pressure range is a feature of type H1 loops. These features together suggest an ordered array of mesopores with a small distribution of sizes and slight deviations from an idealized cylindrical mesopore as noted in SBA-15 [24-26]. However, the CMK-3 type scaffolds have a hysteresis loop containing features of multiple classifications [24], which is not surprising considering the reported structure of these materials [22]. The results suggest an ordered array of mesopores, containing sections that are more slit-like in nature.

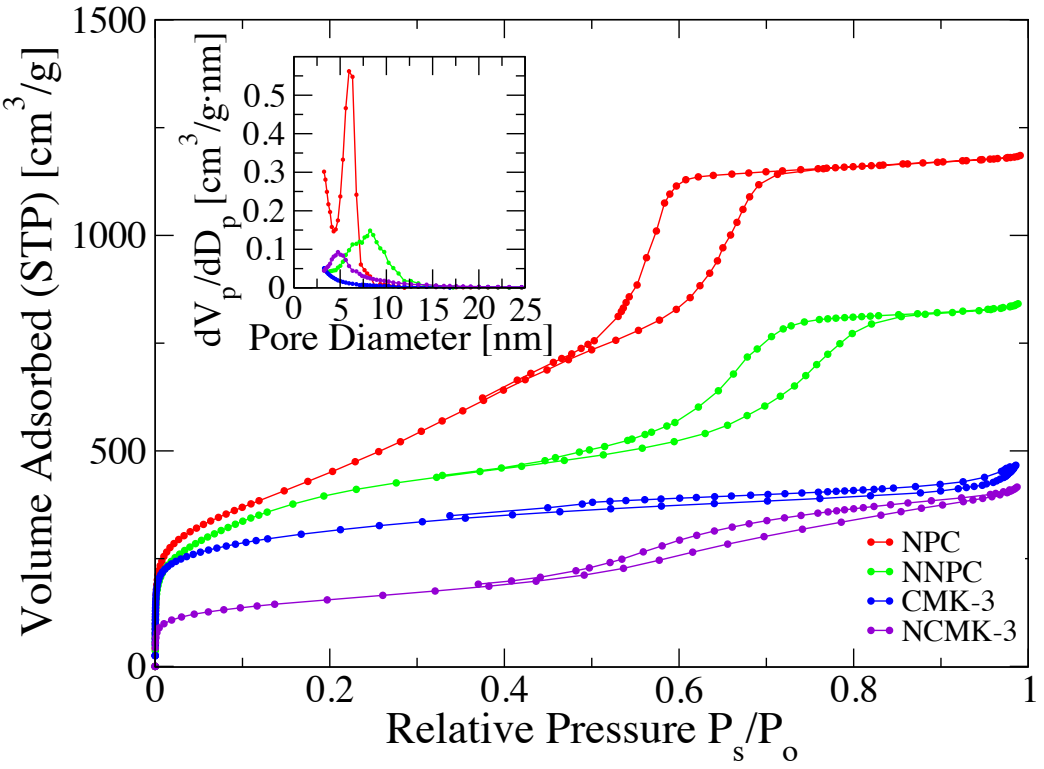

Figure 1. Nitrogen sorption isotherms and pore size distributions (inset) of synthesized porous carbon scaffolds. The NPC and NNPC isotherms have been shifted up 200 and 150 cm^3/g, respectively, for clarity.

Pore size distributions calculated using the BJH model are displayed in the inset of Figure 1. NPC and NNPC have average mesopore diameters of 6 and 7.5 nm respectively, with an indication of a micropore distribution below 3 nm as a result of removing silicate oligomers from the mesopore walls during HF etching following carbonization. The largest contribution to the pore volume in the CMK-3 and NCMK-3 scaffolds appears to be from pores ≤ 3.5 nm. Table 1 lists the average pore size diameter, surface area (S_{BET}), and total pore volume (V_T) obtained for the carbon scaffolds.

Table 1. Summary of Carbon Physical Properties Measured with N_2 Physisorption at 77 K

sample	pore size[a,b] [nm]	S_{BET}[c] [m^2/g]	V_T[d] [cm^3/g]
NPC	6.0	1290	1.63
NNPC	7.5	1426	1.30
CMK-3	3.5	1073	1.08
NCMK-3	3.0	764	0.84

[a] Average pore diameter. [b] Calculated by the BJH method using adsorption branch isotherm data. [c] Calculated using the BET method in a relative pressure range of 0.05 to 0.2. [d] Total pore volume: estimated from the amount adsorbed at a relative pressure (P_s/P_0) of 0.99.

Total pore volume and surface area of the NPC type scaffolds is considerably larger than those of the CMK-3 type. Surface area, pore volume, and average pore size of the respective doped/undoped scaffolds of each geometry are comparable, facilitating a minimization in the variation of substrate-induced effects that could alter the hydrogen sorption properties of an infiltrated metal hydride, allowing any influence of nitrogen functionalizing of the scaffolds to be more readily discerned.

X-ray photoelectron spectroscopy (XPS) measurements were employed to investigate the chemical makeup of the synthesized substrates. Analysis included a survey scan and detailed scans of the N 1s energy region for determination of nitrogen chemical bonding arrangements present in the samples. Survey scans indicated the NPC and CMK-3 substrates contained minor oxygen and nitrogen impurities, with carbon content exceeding 95 atomic percent as shown in Table 2. Figure 2a,b shows the N 1s spectrum recorded for the NNPC and NCMK-3 samples, respectively. In the spectra of both doped samples, four different chemical bonding environments were identified, corresponding to pyridinic (~398 eV), pyrrolic (~400 eV), graphitic (~402 eV), and oxidized nitrogen [27,28]. For each nitrogen bonding environment, the relative atomic concentration was calculated from the proportion of the area of the fit function comprising the total N 1s spectrum for each respective sample. Table 2 summarizes the relative atomic concentrations of each species obtained from the XPS analysis of the carbon samples. Of the identified nitrogen chemical bonding arrangements, the pyridinic nitrogen form is of considerable interest. In this state, a nitrogen atom is sp^2 hybridized within an aromatic ring, participating in one π and two σ bonds with the nearby carbon atoms, leaving a lone pair of electrons available for additional bonding.

Pyridinic nitrogen on the pore wall surface of a carbon scaffold could act as a Lewis base and donate considerable electron density to a confined metal hydride within the nanopore volume, possibly resulting in an alteration of the hydriding properties observed for a metal hydride confined within a comparable nonfunctionalized carbon scaffold of the same geometry.

As a means of observing the effects nitrogen functionalization may have on the hydriding properties of a metal hydride confined within the pore volume of a carbon substrate, the four previously described scaffolds were infiltrated with 20 wt % of $NaAlH_4$, followed by experimental activation energy and hydrogen cycling measurements of the respective composite systems. In order to verify that the $NaAlH_4$ was successfully infiltrated into the pores of the scaffolds, nitrogen sorption, PXRD, and NMR measurements were taken. Figure S1 (Supporting Information) shows a representative plot comparing the isotherm and pore volume distribution of the NPC

carbon scaffold before and after the hydride infiltration process. After infiltration, there is a considerable decrease in volume adsorbed over the whole of the isotherm indicating some portion of the substrate surface is now inaccessible to the nitrogen adsorbate, most likely due to the blocking or filling of substrate pores as evidenced by the shifted pore volume distribution shown in the inset. All of the carbon scaffolds exhibited similar behavior after infiltration. We note here and from previous nitrogen sorption measureme-

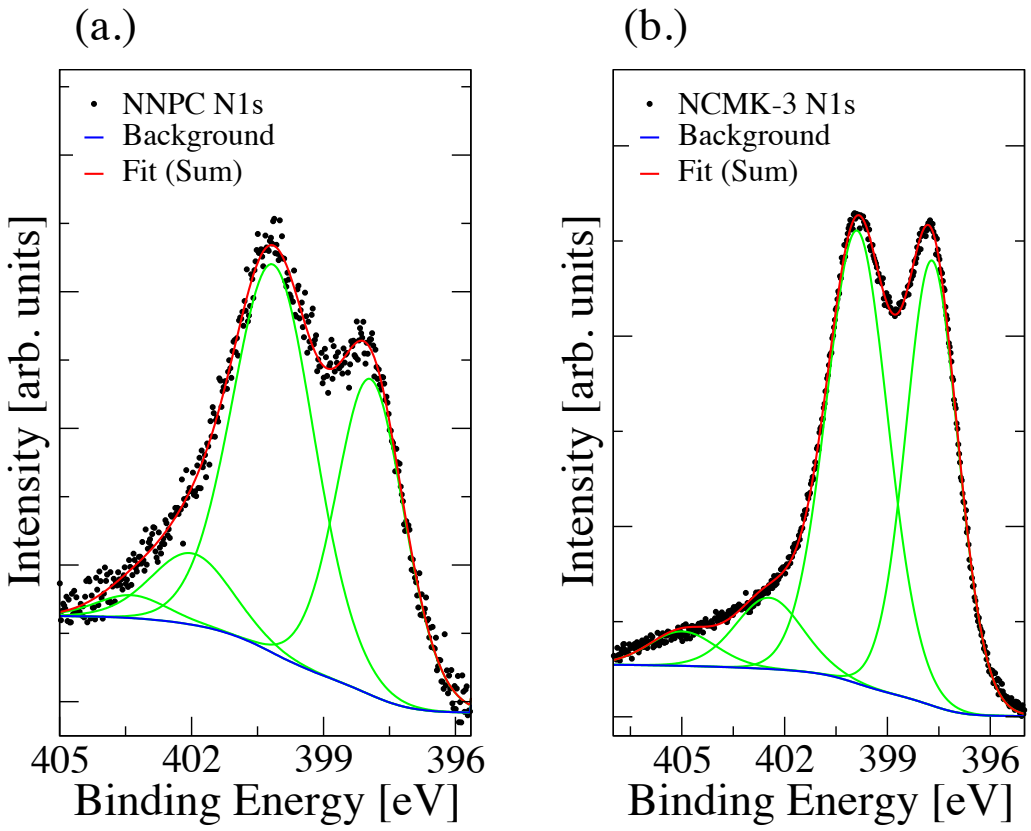

Figure 2. N 1s spectra for (a) NNPC and (b) NCMK-3. Four different chemical bonding environments were identified in the spectra of both samples. Namely, pyridinic (~398 eV), pyrrolic (~400 eV), graphitic (~402 eV), and oxidized (402-405 eV) nitrogen [27,28].

nts that the observed decrease in substrate pore volume after $NaAlH_4$ infiltration is generally slightly higher than expected from a 20 wt % $NaAlH_4$ loading, supporting the notion of minor pore blocking, but consistent with previous studies [4]. Figure S2 shows the PXRD scans taken of the infiltrated and as-prepared substrates. The absence of any $NaAlH_4$ peaks after infiltration confirms that there is little or no $NaAlH_4$ present outside the pores and that any $NaAlH_4$ within the pores is amorphous, suggesting any intact hydride must be confined within the pore structure. Additionally, during this work we found that other samples having identical or slightly higher $NaAlH_4$ loadings and similar pore volume decreases to those described here also exhibited $NaAlH_4$ PXRD reflections, likely due to inadequate mixing of $NaAlH_4$/carbon substrate prior to the infiltration step. Subsequently, PXRD provides a much stronger indicator of successful pore infiltration.

Table 2. Summary of Relative Atomic Concentrations from XPS Measurements

sample	carbon content [at. %]	oxygen content [at. %]	nitrogen total [at. %]	pyridinic nitrogen [at. %]	pyrrolic nitrogen [at. %]	graphitic nitrogen [at. %]	other nitrogen [at. %]
NPC	95.7	3.9	< 1	-	-	-	-
NNPC	84.6	10.5	5.0	1.8	2.6	0.5	0.1
CMK-3	98.1	1.4	< 1	-	-	-	-
NCMK-3	77.8	11.2	11.0	4.4	5.3	0.9	0.4

NMR measurements were conducted to determine which amorphous hydride phases are present in the composite samples. ^{23}Na and ^{27}Al NMR measurements (Figures S3 to S9) show the existence of $NaAlH_4$ in the composite samples and no presence of the NaH or Na_3AlH_6 phases. The ^{23}Na local environment is strongly influenced by the electric field gradient and magnetic susceptibility of the carbon scaffold leading to the different line widths and chemical shifts of the samples. ^{23}Na NMR spectra (Figures S3 to

S5) for confined $NaAlH_4$ are significantly broadened and shifted compared to those of bulk $NaAlH_4$. It is difficult to determine through NMR whether this Na is intercalated into the framework; however, ^{23}Na and ^{27}Al NMR do not indicate the presence of NaH or Na_3AlH_6. Taken together with the N_2 sorption and PXRD measurements, the NMR results indicate that the confinement of $NaAlH_4$ within the carbon scaffold pores was indeed successful. Peaks corresponding to Al can be seen in both the ^{27}Al NMR and PXRD spectra, due to decomposition of a significant fraction of the hydride during infiltration, even at 200 bar H_2, which is considerably higher than the reported equilibrium pressure of 128 bar at 184 °C for the bulk hydride [29]. Measurements performed on a separate set of samples infiltrated at 350 bar H_2 still displayed the presence of Al, indicating decomposition occurs, presumably during the initial substrate wetting process. The spectra for all four composite samples show Al metal but are devoid of the Na_3AlH_6 phase, consistent with previous studies of $NaAlH_4$/C composite systems [4,5,10,30]. Table S1 lists the relative amounts of Al and $NaAlH_4$ calculated from the spectra. In general, the decomposition on infiltration results in about 10 to 70% of aluminum in the metallic state. Although the samples are sealed in separate containers, some oxygen contamination is unavoidable given the surface areas and reactivity of the nanoparticle Al-containing phases. For this reason, peaks corresponding to Al_2O_3 are evident in some ^{27}Al spectra. Since large quantities of Al metal were detected in ^{27}Al NMR and PXRD measurements for both the nitrogen functionalized and nonfunctionalized composite samples, the presence of nitrogen cannot be solely responsible for the noted decomposition. More likely, the catalytic effect of carbon itself during initial hydride wetting is the dominating feature, resulting in a favorable energy shift at the hydride/carbon interface that facilitates decomposition. In contrast, the NCMK-3/CMK-3 type scaffolds showed a higher decomposition compared to the NNPC/NPC versions, indicating the pore geometry might be a more important factor contributing to the degree of decomposition on initial wetting. In the previous study by Nielson et al. [10], the authors observed carbon aerogels with higher pore volumes and surface areas appear to stabilize molten $NaAlH_4$, resulting in less decomposition of $NaAlH_4$ to Al metal during the infiltration process. It is difficult to assess our samples for

a similar trend since the scaffolds of each type were purposely selected to match as closely as possible to minimize the impact of surface area and pore volume in an attempt to elucidate the effect of nitrogen functionalization, in contrast to the carbon aerogels used by Nielson et al. that had differences in surface area and pore volume of at least 44% and 30%, respectively [10]. In this work, more decomposition upon infiltration was noted with the NNPC in comparison to NPC, with the NNPC having 10% more surface area, but 20% less pore volume. In contrast, a *higher* level of decomposition was noted during infiltration with the CMK-3 scaffold, having ~25% *larger* surface area and pore volume, displaying the opposite trend observed in the work by Nielson et al [10].

Arrhenius Analysis. The results of an Arrhenius analysis performed utilizing the methods developed by Sandrock et al. [31] are presented in Figure 3. Data for the bulk $NaAlH_4$ sample recorded previously by Sandrock et al. [31] in a similar experiment is shown for comparison with the nanoconfined samples. In agreement with previous work [1,8,18], the activation energy for H_2 desorption is lowered with respect to the bulk hydride in all nanoconfined samples. Interestingly, $NaAlH_4$ confined in the nitrogen functionalized scaffolds of both geometries exhibits activation energies at least 20 kJ/mol H_2 lower than $NaAlH_4$ confined in the corresponding nonfunctionalized scaffold. Considering the similarity in physical properties with respect to surface area, pore volume, and pore distribution of the respective functionalized/nonfunctionalized scaffold pairs, it appears the presence of nitrogen has a profound effect on the H_2 desorption process. Previous studies indicate that Arrhenius analysis can provide significant insight concerning the processes occurring during hydrogen desorption [31]. However, if desorption does not occur in a single reaction step, the measured activation energy will reflect the multiple competing decomposition mechanisms on the molecular level, making unique determination of the decomposition a challenge [32]. In this regard, $NaAlH_4$ nanoconfined in porous scaffolds has been observed to desorb hydrogen in an apparent single step, without the formation of intermediate phases [4,5,30]. However, multiple processes including nucleation, diffusion, hydride/substrate interactions, and hydride phase transitions may occur during thermal decomposition simultaneously. Consequently, the activation energy of hydrogen desorption measured from isothermal

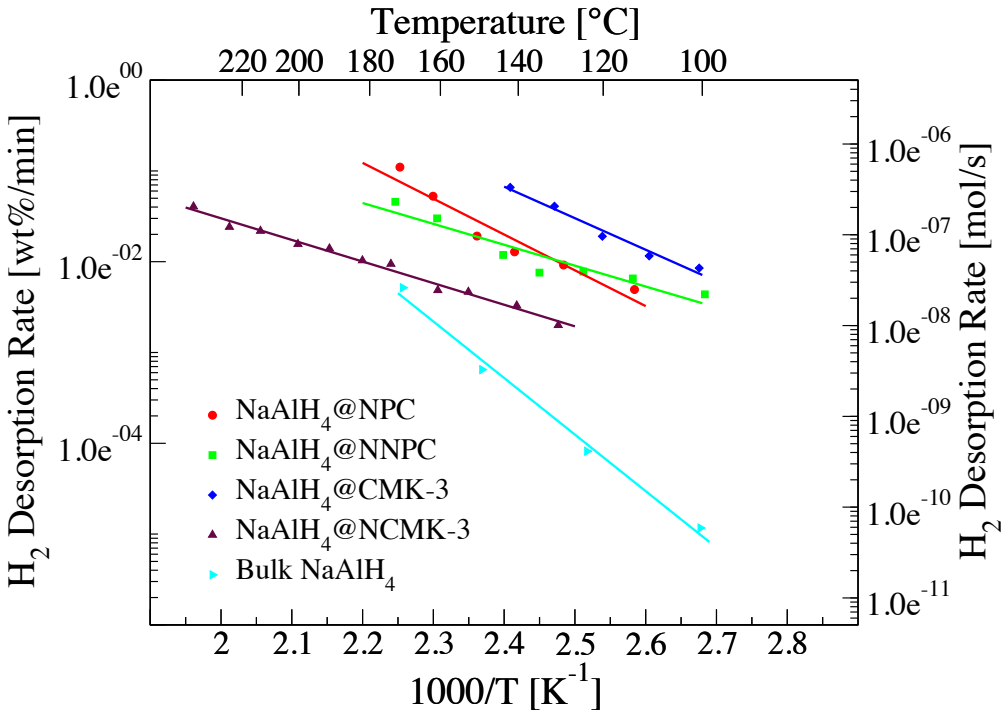

Figure 3. Arrhenius plots from isothermal desorption measurements. Data for the bulk $NaAlH_4$ was obtained from Sandrock et al. [31] and shown for comparison.

Arrhenius analysis should therefore be viewed as an amalgamation of the energies associated with each individual process. Calculated errors for the hydrogen desorption rate are less than 1.7 X 10^{-3} wt %/min. All of the data in Figure 3 was recorded during the first desorption from the infiltrated samples. Following rehydriding, the experiment was repeated. The measured activation energies from the second experiment agree well with the initial findings. Table 3 lists the activation energies and pre-exponential rate constants obtained from the Arrhenius analysis. Physically, the pre-exponential rate constant or frequency factor describes the frequency of collisions between reactant species and therefore is directly related to the desorption mechanism. As shown in Table 3, the rate constants increase with the activation energy. Though a trend is evident, determining the relation to the desorption mechanism is not straightforward due to the existence of impurities and the multiple phases present. Although studies of the bulk decomposition

processes in $NaAlH_4$ have been identified [33,34], the mechanisms for diffusion in real experiments are dramatically altered by the presence of impurities, for example, oxygen, in particular. This is most obviously seen in the identification of a rapidly mobile Al species identified in $NaAlH_4$ when oxygen is present even in small quantities [35]. In our decomposing material, there are multiple phases in contact including solid, liquid, and gas phase reactants, in addition to the variable surface morphology of the carbon and the impurities that are present in the carbon.

Gas Desorption. To investigate the dehydriding process of confined $NaAlH_4$ in the presence of nitrogen atoms, the desorption of hydrogen from the samples was recorded during the third cycle. Figure 4 displays the third H_2 desorption cycle from RT to 300 °C at a ramp rate of 4 °C/min. The H_2 weight percent has been normalized considering the mass of $NaAlH_4$ present in each respective sample prior to the infiltration procedure. Due to the noted decomposition of a portion of the sample during infiltration, the wt % desorbed for each sample in Figure 4 represents a lower bound, and the actual

Table 3. Activation Energies Measured by Isothermal Arrhenius Analysis

sample	activation energy [kJ/mol H_2]	rate constant [wt % H_2/min]	relative changes [kJ/mol H_2]
bulk $NaAlH_4$	118.1[a]	3.3×10^{11} [a]	-
$NaAlH_4$@NPC	75.5 ± 10.4	5.9×10^{7}	$\Delta_{Bulk} = -42.6$
$NaAlH_4$@NNPC	44.1 ± 6.6	5.1×10^{3}	$\Delta_{NPC} = -31.4$
$NaAlH_4$@CMK-3	66.5 ± 5.7	1.5×10^{7}	$\Delta_{Bulk} = -51.6$
$NaAlH_4$@NCMK-3	45.6 ± 1.7	1.7×10^{3}	$\Delta_{CMK3} = -20.9$

[a]Data taken from Sandrock et al. [31]

sample capacity is likely higher. Hydrogen desorption during the first two cycles was used to measure the rate of desorption under isothermal conditions at different set temperatures as previously described and therefore is not directly comparable with the data presented in Figure 4 as the total desorption capacity during the first two cycles cannot be accurately assessed due to the evacuation of the desorption volume between successive measurement points. As displayed in Figure 4, all the samples still display reversibility after the initial two cycles noted. Additionally, Figure S9 shows $NaAlH_4$ is reformed following the third rehydriding cycle. Nonfunctionalized systems have a higher reversible capacity of ~3 wt % hydrogen with respect to the initial $NaAlH_4$ loading compared to ~1 wt % observed for the nitrogen functionalized samples. In Figure 4, the

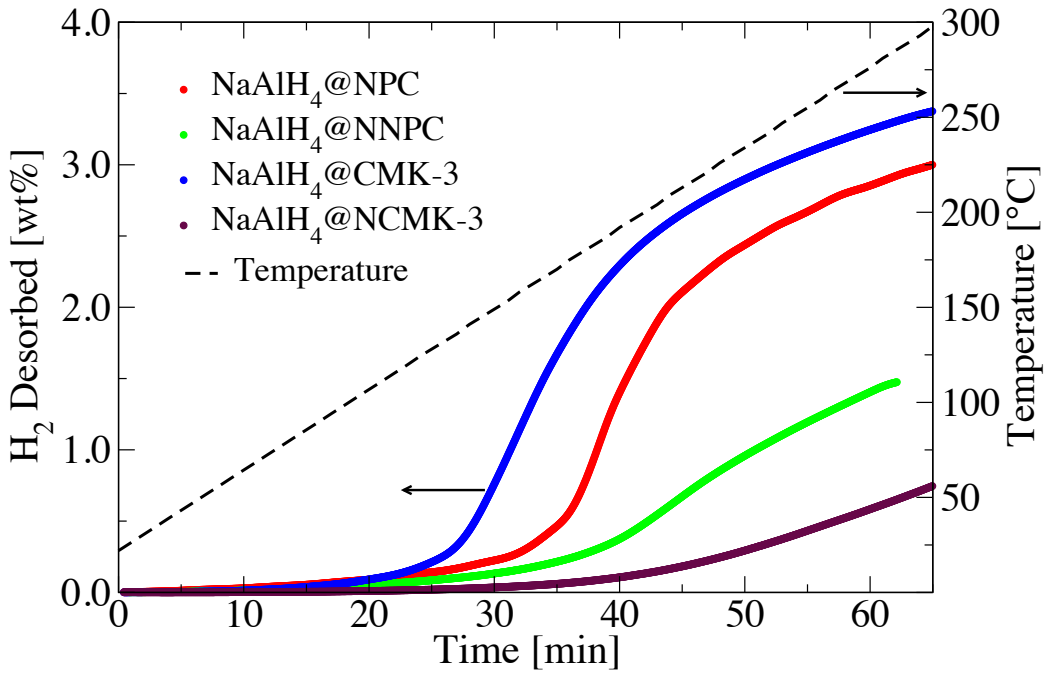

Figure 4. Hydrogen desorption (third cycle) from the $NaAlH_4$-infiltrated substrates. The black dashed trace displays the sample temperature profile.

difference in the desorption profile between the nitrogen functionalized/nonfunctionalized systems is immediately apparent, as the composite systems functionalized with nitrogen do not desorb hydrogen in significant quantity until much higher temperature. Considering the results of the Arrhenius analysis, which indicated activation energies for hydrogen desorption of at least 20 kJ/mol H_2 less in the nitrogen functionalized samples, the behavior exhibited by these samples in the desorption profile is unexpected. To better understand the hydrogen desorption profile, it was instructive to consider the hydrogen desorption rate as a function of time. Using a forward difference routine, we calculated the derivative of the measured desorption data sets.

Figure 5 shows the rate profiles resulting from differentiating the data presented in Figure 4. The rate curves are cutoff at the point corresponding to depletion of the $NaAlH_4$ reactant during decomposition. Profiles presented in Figure 5 highlight the significant difference in temperature at which hydrogen desorption from the nitrogen functionalized samples reach the highest rate of desorption in comparison to the respective nonfunctionalized scaffold. Small temperature fluctuations in the ramp rate are exacerbated in the forward difference resulting in, for example, the small deviations at 28 and 34 min for the data corresponding to $NaAlH_4$@NPC (red). This does not affect the clear difference in rates between nitrogen-doped and undoped carbons. Black bars on the rate profiles indicate the temperature region where desorption rate measurements were recorded during a separate isothermal Arrhenius experiment conducted to determine experimentally the activation energies in Table 3. We emphasize that the activation energies were not calculated using data from Figure 5; we show the temperature regions corresponding to the Arrhenius measurements for comparison only.

4. DISSCUSSION

Previous studies of $NaAlH_4$ supported on nanofibers [36] and $NaAlH_4$ nano-confined in a variety of materials including high surface area graphite [4,5], carbon aerogels [9,10,37], and metal-organic frameworks (MOFs) [8,38] have all reported enhanced desorption kinetics and improved reversibility with regard to bulk $NaAlH_4$. In

particular, the work by Baldé et al. [36] demonstrated a correlation between decreasing nanoparticle size with a reduction in the activation energy and temperature of hydrogen desorption, in addition to a lower required pressure for hydrogen reloading. Baldé et al. measured an activation energy of 58 kJ/mol H_2 for nanoparticles with a size distribution

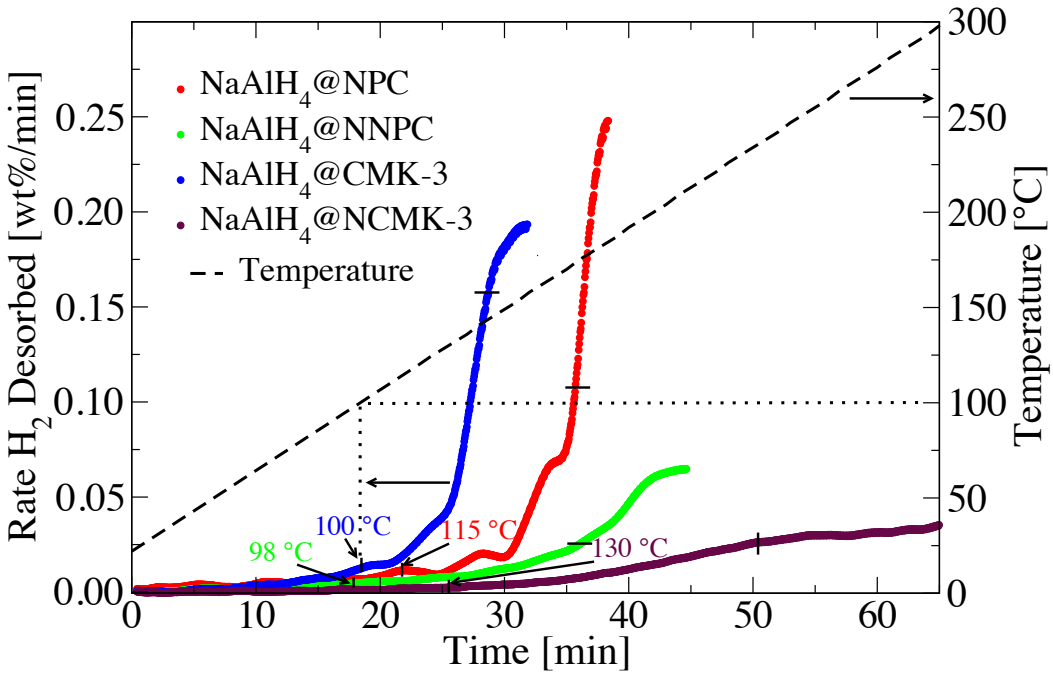

Figure 5. Rate of hydrogen desorption with respect to time for the four desorption profiles (third cycle) of the $NaAlH_4$-infiltrated carbon scaffolds shown in Figure 4. For comparison, the black line delineates the temperature region where desorption rates were measured during the separate isothermal Arrhenius experiment presented in Figure 3.

of 1-10 nm. A tighter bound on the nanoparticle size required to achieve activation energies below 60 kJ/mol H_2 was provided in subsequent studies of $NaAlH_4$ confined in highly ordered MOFs containing monodisperse pore distributions near 1 nm [8,38], reporting activation energies of 53.3 and 57.4 kJ/mol H_2. Our measured activation energies for the nonfunctionalized scaffolds in Table 3 are in relative agreement with the

previous studies, measuring 75.5 and 66.5 kJ/mol H_2 for $NaAlH_4$ confined in NPC with an average pore size of 6 nm and CMK-3 with an average pore size of 3.5 nm. Considering the similar physical characteristics between the nonfunctionalized and functionalized scaffolds of both morphologies, it is interesting that the measured activation energies for $NaAlH_4$ confined in NNPC and NCMK-3 are reduced to 44.1 and 45.6 kJ/mol H_2, respectively. Based on previous studies, the hydride particle size alone in the surface functionalized systems cannot account for a decrease in activation energy below 50 kJ/mol H_2, suggesting the presence of nitrogen influences the hydrogen desorption process. In accordance with previous works on nanoconfined $NaAlH_4$ [4,5,8-10,37,38], we observed significant temperature decreases for the onset of hydrogen desorption relative to bulk $NaAlH_4$ and maximum rates of hydrogen desorption at temperatures <180 °C for the samples confined in nonfunctionalized scaffolds. In contrast, samples of $NaAlH_4$ confined in nitrogen functionalized scaffolds show a less pronounced decrease in the onset of hydrogen desorption and display maximum rates of hydrogen desorption at temperatures exceeding 200 °C. In view of the further decreased activation energy for the nitrogen functionalized samples, the shift in maximum desorption rate to *higher* temperatures is unexpected. There appears to be some correlation between the shifting of maximum hydrogen desorption rate to higher temperature and nitrogen content of the carbon scaffolds, as the temperature shift is considerably larger for the CMK-3/NCMK-3 pair, where the NCMK-3 scaffold contains roughly two times more nitrogen than the NNPC scaffold. Although the magnitude of the temperature shift could be a function of the pore geometry, this seems less likely in view of the similarity in the shapes of the desorption and desorption rate profiles for the functionalized and nonfunctionalized samples, respectively, even though the scaffolds have markedly different pore geometries.

It is difficult to determine uniquely the mechanism through which nitrogen addition to the scaffold surface acts to influence $NaAlH_4$ in this system, though previous studies concerning carbon scaffold surface chemistry may provide insight into some of the general underlying features. Through modeling and experiment, Berseth et al. [39] found that the presence of carbon scaffolds (graphene, nanotubes, and C_{60}) destabilized

the $NaAlH_4$ as a result of the charge transfer from Na atoms to the electronegative carbon scaffold at the hydride/scaffold interface, resulting in a weakening of the Na-AlH_4 ionic bond that is correlated with the electron affinity and curvature of the carbon substrate. Surface functionalization with nitrogen will increase the electron density in the scaffold but should remain localized near the nitrogen heteroatom, giving rise to the XPS spectra indicating pyridinic and pyrrolic signatures. The amorphous nature of our carbons and the presence of adsorbates (Na, NaH, Al, AlH_x, etc.) and impurities such as oxygen preclude a definitive explanation of the anomalous desorption rates. Putting aside these difficulties, first-principles calculations of the electronic properties of N-doped graphene monolayers show the electronic DOS is shifted down with respect to a nonfunctionalized graphene sheet, due to additional filling of electronic states around the Fermi level from the increased number of valence electrons as a result of nitrogen inclusion [40]. There are unfilled electronic states in the vicinity of the Fermi level, indicating that the transfer of electron density from an adsorbate species in close proximity to the scaffold is allowed and should depend on the relative electronic energy levels of the scaffold and adsorbate species, respectively. In regard to defects such as edge sites, measurements of the local DOS on the surface of nitrogen functionalized graphite indicated nitrogen atoms in the pyridinic configuration are likely to be negatively charged and should act as Lewis bases with respect to adsorbate species [41].

Although the exact mechanism responsible for the observed anomalous desorption is not fully understood, it must be associated with interactions between the hydride and host surface. It is also important to note that the fastest desorption in the functionalized carbons takes place above 180 °C, near the melting temperature of bulk $NaAlH_4$ [5,29], and suggests the anomalous behavior is linked with the transition of $NaAlH_4$ from the solid to liquid phase in the presence of nitrogen atoms in the functionalized substrate. Desorption data in Figure 4 indicate that the majority of hydrogen is released above ~ 180 °C. Figure 5 shows the maximum desorption rate coincides with this observation as well. Further, NMR measurements confirmed considerable hydride decomposition occurs during infiltration where $NaAlH_4$ is in the liquid phase. Due to the partial decomposition of a fraction of $NaAlH_4$ during infiltration,

it is likely that Al metal and some Na species coexist in the pores with the intact $NaAlH_4$. This Na species cannot be positively identified as NaH, and there is no indication from ^{27}Al NMR that Na_3AlH_6 has formed. Intercalated Na in the framework would generally increase the electron density in the local environment, and this may influence the surface energies of adsorbed $NaAlH_4$, which could influence the desorption kinetics and/or mechanism. Finally, nanoconfinement of $NaAlH_4$ causes a shift in melting temperature from that of the bulk phase due to mechanical effects such as substrate-induced lattice strain, chemical interaction with the substrate, or electronic effects [4,5].

5. CONCLUSIONS

We presented evidence from N_2 sorption, XPS, PXRD, and NMR measurements that indicate two different types of nanoporous carbon scaffolds, both with and without nitrogen surface functionalization, were successfully infiltrated with $NaAlH_4$. After infiltration, no reflections from crystalline $NaAlH_4$ were detected during PXRD measurements, indicating any intact $NaAlH_4$ is amorphous. ^{27}Al MAS NMR and PXRD detect the presence of Al metal, revealing a fraction of $NaAlH_4$ decomposes during infiltration in the presence of all carbon scaffolds of both geometries at hydrogen pressures well in excess of the bulk equilibrium pressure at melting [29], suggesting a strong interaction with the scaffold surface. Despite some decomposition, NMR confirms the existence of intact $NaAlH_4$, with no detection of the Na_3AlH_6 or NaH phases present in the samples. Isothermal Arrhenius analysis indicates the activation energy for hydrogen desorption from nitrogen functionalized carbons is decreased by 20 kJ/mol or more over the nonfunctionalized carbons. The presence of nitrogen evidently has a significant influence on the desorption process. Hydrogen cycling measurements indicate that hydrogen can be reversibly stored within all the scaffolds examined, with a reversible storage capacity up to 3 wt % H_2 after three cycles with the pore loading achieved in this work. Higher levels of reversible capacity could likely be attained with higher pore loadings. During the hydrogen desorption process, the majority of hydrogen is not released until higher temperatures for $NaAlH_4$ confined in the nitrogen functionalized scaffolds, despite the significantly lower measured activation energies. This indicates the

existence of a rate-limiting step for desorption that may be linked to the level of nitrogen doping in the scaffolds and the onset of $NaAlH_4$ melting. Further investigation will include magic angle spinning nuclear magnetic resonance experiments using the NCMK-3 scaffold, but with labeled ^{15}N isotope-containing scaffolds.

Ultimately, our results show that nanoconfinement and surface functionalization of carbon substrates allows for dramatically altering the kinetic behavior, and possibly thermodynamics, governing the decomposition of $NaAlH_4$ and potentially related complex hydrides. A detailed understanding of the basic mechanisms underlying these effects could yield a powerful tool for designing materials for hydrogen storage and other applications involving nanoporous carbon substrates.

ACKNOWLEDGEMENTS

Sandia National Laboratories is a multimission laboratory managed and operated by National Technology and Engineering Solutions of Sandia, LLC., a wholly owned subsidiary of Honeywell International, Inc., for the U.S. Department of Energy's National Nuclear Security Administration under contract DE-NA-0003525. The authors gratefully acknowledge research support from the Hydrogen Materials Advanced Research Consortium (HyMARC), established as part of the Energy Materials Network under the U.S. Department of Energy, Office of Energy Efficiency and Renewable Energy, Fuel Cell Technologies Office, under Award Number DOE-EE0007656. The views and opinions of the authors expressed herein do not necessarily state or reflect those of the United States Government or any agency thereof. Neither the United States Government nor any agency thereof, nor any of their employees, makes any warranty, expressed or implied, or assumes any legal liability or responsibility for the accuracy, completeness, or usefulness of any information, apparatus, product, or process disclosed, or represents that its use would not infringe privately owned rights. The authors would like to thank Josh Whaley for the design and construction of clean-transfer holders for the XPS system.

REFERENCES

[1] Gross, A. F.; Vajo, J. J.; Van Atta, S. L.; Olson, G. L. Enhanced Hydrogen Storage Kinetics of $LiBH_4$ in Nanoporous Carbon Scaffolds. *J. Phys. Chem. C* **2008**, *112*, 5651–5657.

[2] Cahen, S.; Eymery, J.-B.; Janot, R.; Tarascon, J.-M. Improvement of the $LiBH_4$ Hydrogen Desorption by Inclusion into Mesoporous Carbons. *J. Power Sources* **2009**, *189*, 902–908.

[3] Stephens, R. D.; Gross, A. F.; Van Atta, S. L.; Vajo, J. J.; Pinkerton, F. E. The Kinetic Enhancement of Hydrogen Cycling in $NaAlH_4$ by Melt Infusion into Nanoporous Carbon Aerogel. *Nanotechnology* **2009**, *20*, 204018.

[4] Adelhelm, P.; Gao, J.; Verkuijlen, M. H. W.; Rongeat, C.; Herrich, M.; van Bentum, P. J. M.; Gutfleisch, O.; Kentgens, A. P. M.; de Jong, K. P.; de Jongh, P. E. Comprehensive Study of Melt Infiltration for the Synthesis of $NaAlH_4$/C Nanocomposites. *Chem. Mater.* **2010**, *22*, 2233–2238.

[5] Gao, J.; Adelhelm, P.; Verkuijlen, M. H. W.; Rongeat, C.; Herrich, M.; van Bentum, P. J. M.; Gutfleisch, O.; Kentgens, A. P. M.; de Jong, K. P.; de Jongh, P. E. Confinement of $NaAlH_4$ in Nanoporous Carbon: Impact on H_2 Release, Reversibility, and Thermodynamics. *J. Phys. Chem. C* **2010**, *114*, 4675–4682.

[6] Liu, X.; Peaslee, D.; Jost, C. Z.; Majzoub, E. H. Controlling the Decomposition Pathway of $LiBH_4$ via Confinement in Highly Ordered Nanoporous Carbon. *J. Phys. Chem. C* **2010**, *114*, 14036–14041.

[7] Liu, X.; Peaslee, D.; Jost, C. Z.; Baumann, T. F.; Majzoub, E. H. Systematic Pore-Size Effects of Nanoconfinement of $LiBH_4$: Elimination of Diborane Release and Tunable Behavior for Hydrogen Storage Applications. *Chem. Mater.* **2011**, *23*, 1331–1336.

[8] Stavila, V.; Bhakta, R. K.; Alam, T. M.; Majzoub, E. H.; Allendorf, M. D. Reversible Hydrogen Storage by $NaAlH_4$ Confined within a Titanium-Functionalized MOF-74(Mg) Nanoreactor. *ACS Nano* **2012**, *6*, 9807–9817.

[9] Nielsen, T. K.; Javadian, P.; Polanski, M.; Besenbacher, F.; Bystrzycki, J.; Jensen, T. R. Nanoconfined $NaAlH_4$: Determination of Distinct Prolific Effects from Pore Size, Crystallite Size, and Surface Interactions. *J. Phys. Chem. C* **2012**, *116*, 21046–21051.

[10] Nielsen, T. K.; Javadian, P.; Polanski, M.; Besenbacher, F.; Bystrzycki, J.; Skibsted, J.; Jensen, T. R. Nanoconfined $NaAlH_4$: Prolific Effects from Increased Surface Area and Pore Volume. *Nanoscale* **2014**, *6*, 599–607.

[11] Klebanoff, L. E.; Keller, J. O. 5 Years of Hydrogen Storage Research in the U.S. DOE Metal Hydride Center of Excellence (MHCoE). *Int. J. Hydrogen Energy* **2013**, *38*, 4533–4576.

[12] Mason, T.; Majzoub, E. H. Effects of a Carbon Surface Environment on the Decomposition Properties of Nanoparticle $LiBH_4$: A First-Principles Study. *J. Phys. Chem. C* **2014**, *118*, 8852–8858.

[13] Remhof, A.; Mauron, P.; Züttel, A.; Embs, J. P.; Łodziana, Z.; Ramirez-Cuesta, A. J.; Ngene, P.; de Jongh, P. Hydrogen Dynamics in Nanoconfined Lithiumborohydride. *J. Phys. Chem. C* **2013**, *117*, 3789–3798.

[14] Verdal, N.; Udovic, T. J.; Rush, J. J.; Liu, X.; Majzoub, E. H.; Vajo, J. J.; Gross, A. F. Dynamical Perturbations of Tetrahydroborate Anions in $LiBH_4$ due to Nanoconfinement in Controlled-Pore Carbon Scaffolds. *J. Phys. Chem. C* **2013**, *117*, 17983–17995.

[15] Suwarno; Ngene, P.; Nale, A.; Eggenhuisen, T. M.; Oschatz, M.; Embs, J. P.; Remhof, A.; de Jongh, P. E. Confinement Effects for Lithium Borohydride: Comparing Silica and Carbon Scaffolds. *J. Phys. Chem. C* **2017**, *121*, 4197–4205.

[16] Shane, D. T.; Corey, R. L.; McIntosh, C.; Rayhel, L. H.; Bowman, R. C.; Vajo, J. J.; Gross, A. F.; Conradi, M. S. $LiBH_4$ in Carbon Aerogel Nanoscaffolds: An NMR Study of Atomic Motions. *J. Phys. Chem. C* **2010**, *114*, 4008–4014.

[17] Zou, H.; Gradišek, A.; Emery, S. B.; Vajo, J. J.; Conradi, M. S. $LiBH_4$ in Aerogel: Ionic Motions by NMR. *J. Phys. Chem. C* **2017**, *121*, 15114–15119.

[18] Carr, C. L.; Majzoub, E. H. Surface-Functionalized Nanoporous Carbons for Kinetically Stabilized Complex Hydrides through Lewis Acid–Lewis Base Chemistry. *J. Phys. Chem. C* **2016**, *120*, 11426–11432.

[19] Bogdanović, B.; Schwickardi, M. Ti-Doped Alkali Metal Aluminium Hydrides as Potential Novel Reversible Hydrogen Storage Materials. *J. Alloys Compd.* **1997**, *253-254*, 1–9.

[20] Liu, R.; Shi, Y.; Wan, Y.; Meng, Y.; Zhang, F.; Gu, D.; Chen, Z.; Tu, B.; Zhao, D. Triconstituent Co-Assembly to Ordered Mesostructured Polymer−Silica and Carbon−Silica Nanocomposites and Large-Pore Mesoporous Carbons with High Surface Areas. *J. Am. Chem. Soc.* **2006**, *128*, 11652–11662.

[21] Song, Y.; Li, L.; Wang, Y.; Wang, C.; Guo, Z.; Xia, Y. Nitrogen-Doped Ordered Mesoporous Carbon with a High Surface Area, Synthesized through Organic-Inorganic Coassembly, and Its Application in Supercapacitors. *ChemPhysChem* **2014**, *15*, 2084–2093.

[22] Jun, S.; Joo, S. H.; Ryoo, R.; Kruk, M.; Jaroniec, M.; Liu, Z.; Ohsuna, T.; Terasaki, O. Synthesis of New, Nanoporous Carbon with Hexagonally Ordered Mesostructure. *J. Am. Chem. Soc.* **2000**, *122*, 10712–10713.

[23] Vinu, A.; Ariga, K.; Mori, T.; Nakanishi, T.; Hishita, S.; Golberg, D.; Bando, Y. Preparation and Characterization of Well-Ordered Hexagonal Mesoporous Carbon Nitride. *Adv. Mater.* **2005**, *17*, 1648–1652.

[24] Sing, K. S. W. Reporting Physisorption Data for Gas/Solid Systems with Special Reference to the Determination of Surface Area and Porosity. *Pure Appl. Chem*. **1985**, *57*, 603–619.

[25] Zhao, D.; Feng, J.; Huo, Q.; Melosh, N.; Fredrickson, G. H.; Chmelka, B. F.; Stucky, G. D. Triblock Copolymer Syntheses of Mesoporous Silica with Periodic 50 to 300 Angstrom Pores. *Science* **1998**, *279*, 548–552.

[26] Kruk, M.; Jaroniec, M.; Ko, C. H.; Ryoo, R. Characterization of the Porous Structure of SBA-15. *Chem. Mater.* **2000**, *12*, 1961–1968.

[27] Sun, F.; Liu, J.; Chen, H.; Zhang, Z.; Qiao, W.; Long, D.; Ling, L. Nitrogen-Rich Mesoporous Carbons: Highly Efficient, Regenerable Metal-Free Catalysts for Low-Temperature Oxidation of H_2S. *ACS Catal.* **2013**, *3*, 862–870.

[28] Zhao, Z.; Dai, Y.; Lin, J.; Wang, G. Highly-Ordered Mesoporous Carbon Nitride with Ultrahigh Surface Area and Pore Volume as a Superior Dehydrogenation Catalyst. *Chem. Mater.* **2014**, *26*, 3151–3161.

[29] Dymova, T. N.; Dergachev, Y. M.; Sokolov, V. A.; Grechanaya, N. A. Dissociation Pressure of $NaAlH_4$ and Na_3AlH_6. *Dokl. Akad. Nauk SSSR* **1975**, *224*, 591–592.

[30] Verkuijlen, M. H. W.; Gao, J.; Adelhelm, P.; van Bentum, P. J. M.; de Jongh, P. E.; Kentgens, A. P. M. Solid-State NMR Studies of the Local Structure of $NaAlH_4$/C Nanocomposites at Different Stages of Hydrogen Desorption and Rehydrogenation. *J. Phys. Chem. C* **2010**, *114*, 4683–4692.

[31] Sandrock, G.; Gross, K.; Thomas, G. Effect of Ti-Catalyst Content on the Reversible Hydrogen Storage Properties of the Sodium Alanates. *J. Alloys Compd.* **2002**, *339*, 299–308.

[32] Poonyayant, N.; Stavila, V.; Majzoub, E. H.; Klebanoff, L. E.; Behrens, R.; Angboonpong, N.; Ulutagay-Kartin, M.; Pakawatpanurut, P.; Hecht, E. S.; Breit, J. S. An Investigation into the Hydrogen Storage Characteristics of $Ca(BH_4)_2/LiNH_2$ and $Ca(BH_4)_2/NaNH_2$: Evidence of Intramolecular Destabilization. *J. Phys. Chem. C* **2014**, *118*, 14759–14769.

[33] Michel, K. J.; Ozoliņš, V. Native Defect Concentrations in $NaAlH_4$ and Na_3AlH_6. *J. Phys. Chem. C* **2011**, *115*, 21443–21453.

[34] Michel, K. J.; Ozoliņš, V. Vacancy Diffusion in $NaAlH_4$ and Na_3AlH_6. *J. Phys. Chem. C* **2011**, *115*, 21465–21472.

[35] Ivancic, T. M.; Hwang, S.-J.; Bowman, R. C.; Birkmire, D. S.; Jensen, C. M.; Udovic, T. J.; Conradi, M. S. Discovery of A New Al Species in Hydrogen Reactions of $NaAlH_4$. *J. Phys. Chem. Lett.* **2010**, *1* (15), 2412–2416.

[36] Baldé, C. P.; Hereijgers, B. P. C.; Bitter, J. H.; Jong, K. P. de. Sodium Alanate Nanoparticles − Linking Size to Hydrogen Storage Properties. *J. Am. Chem. Soc.* **2008**, *130*, 6761–6765.

[37] Nielsen, T. K.; Polanski, M.; Zasada, D.; Javadian, P.; Besenbacher, F.; Bystrzycki, J.; Skibsted, J.; Jensen, T. R. Improved Hydrogen Storage Kinetics of Nanoconfined $NaAlH_4$ Catalyzed with $TiCl_3$ Nanoparticles. *ACS Nano* **2011**, *5*, 4056–4064.

[38] Bhakta, R. K.; Herberg, J. L.; Jacobs, B.; Highley, A.; Behrens, R.; Ockwig, N. W.; Greathouse, J. A.; Allendorf, M. D. Metal−Organic Frameworks As Templates for Nanoscale $NaAlH_4$. *J. Am. Chem. Soc.* **2009**, *131*, 13198–13199.

[39] Berseth, P. A.; Harter, A. G.; Zidan, R.; Blomqvist, A.; Araújo, C. M.; Scheicher, R. H.; Ahuja, R.; Jena, P. Carbon Nanomaterials as Catalysts for Hydrogen Uptake and Release in $NaAlH_4$. *Nano Lett.* **2009**, *9*, 1501–1505.

[40] Laref, A.; Ahmed, A.; Bin-Omran, S.; Luo, S. J. First-Principle Analysis of the Electronic and Optical Properties of Boron and Nitrogen Doped Carbon Mono-Layer Graphenes. *Carbon* **2015**, *81*, 179–192.

[41] Kondo, T.; Casolo, S.; Suzuki, T.; Shikano, T.; Sakurai, M.; Harada, Y.; Saito, M.; Oshima, M.; Trioni, M. I.; Tantardini, G. F.; et al. Atomic-Scale Characterization of Nitrogen-Doped Graphite: Effects of Dopant Nitrogen on the Local Electronic Structure of the Surrounding Carbon Atoms. *Phys. Rev. B* **2012**, *86,* 035436.

SUPPORTING INFORMATION

• Experimental Procedures:

Chemicals: Phenol, Formalin, tetraethyl orthosilicate (TEOS), Pluronic F-127 tri-block copolymer, dicyandiamide, carbon tetrachloride (CTC) and ethylenediamine

(EDA) were purchased from Sigma-Aldrich. SBA-15 silicate hard template was purchased from ACS Materials. Deionized water was used in all experiments.

Resol precursors: In a typical process, 6.1 g of phenol was melted in a Schlenk flask at 40 ºC and added to 1.3 g of 20 wt.% NaOH solution under stirring. At the end of 10 minutes, 10.5 g of formalin was added at a temperature below 50 ºC dropwise. The resulting mixture was placed in a water bath at 70 ºC under stirring for 80 minutes and then allowed to cool to room temperature (RT). Using 1 N HCl the pH of the solution was adjusted to ~7.0. Water was removed from the solution under vacuum at 45 ºC, producing a gel-like product. Ethanol was added to dissolve the product, producing a 20 wt.% resol-ethanol solution after mixing. The solution was allowed to settle and then poured off into a separate flask, leaving behind the salt from the acid-base neutralization.

NPC produced using inorganic/organic self-assembly method [1]: In a typical process to produce 2D hexagonal carbon, 16 g F-127 tri-block copolymer was added to a solution consisting of 80 g ethanol and 10 g 0.2 M HCl. After stirring for 1 hour at 40 ºC, 20.8 g TEOS and 50 g of 20 wt.% resol-ethanol solution were added sequentially, followed by stirring for 2 hours at 40 ºC. The solution was poured into a glass pan and allowed to evaporate overnight at RT, producing a transparent film. In order to thermopolymerize the sample, heat treatment at 100 ºC was carried out in an oven for 24 hours. The sample was scraped from the pan, ground into a fine powder, and placed into a tube furnace under flowing nitrogen for calcination at 350 ºC for 3 hours, followed by carbonization at 900 ºC for 2 hours. During the heat treatment the ramp rate was 1 ºC/min below 600 ºC and 5 ºC/min after. To remove the silicate, the sample was etched in 5 wt.% HF solution overnight twice under stirring, followed by washing with ethanol and deionized water. Finally, the carbon sample was dried for 24 hours at 100 ºC and additionally overnight at 300 ºC under dynamic vacuum. The final sample was transported without air exposure to an argon-filled glovebox for storage.

NNPC produced using inorganic/organic self-assembly method [2]: In a typical process, 8 g of F-127 tri-block co-polymer and 7.5 g dicyandiamide are added to a solution consisting of 100 g ethanol, 50 g H_2O, and 10 g 0.2 M HCl. After stirring for 1 hour at 40 ºC, 10.4 g TEOS and 25 g of 20 wt.% resol-ethanol solution were added

sequentially, followed by stirring for an additional 2 hours at 40 ºC. In order to evaporate the solvent, the mixture was poured into pans and placed in an oven at 45 ºC for 8 hours resulting in the formation of uniform films. In order to thermopolymerize the sample, heat treatment at 100 ºC was carried out in an oven for 24 hours. The sample was scraped from the pan, ground into a fine powder, and placed into a tube furnace under flowing nitrogen for calcination at 250 ºC for 2 hours, followed by carbonization at 700 ºC for 3 hours. During the heat treatment the ramp rate was 1 ºC/min. To remove the silicate, the sample was etched in 5 wt.% HF solution overnight twice under stirring, followed by washing with ethanol and deionized water. Finally, the carbon sample was dried for 24 hours at 100 ºC and additionally overnight at 300 ºC under dynamic vacuum. The final sample was transported without air exposure to an argon-filled glovebox for storage.

CMK-3 produced using the nanocasting method [3]: In a typical synthesis, 6.25 g sucrose was dissolved in a mixture consisting of 0.7 g H_2SO_4 and 25 g H_2O, followed by the addition of 5 g SBA-15 silicate hard template material. After 15 minutes of stirring, a uniform white slurry was obtained. Heat treatments of the sample at 100 ºC for 6 hours and 160 ºC for 6 hours were performed sequentially. The resulting black/brown powder sample was added to a solution consisting of 4 g sucrose dissolved in 0.45 g H_2SO_4 and 25 g H_2O. After 25 minutes of stirring the previous heat treatments were repeated, followed by carbonization of the sample in a tube furnace at 900 ºC under flowing argon for 3 hours. During the heat treatment the ramp rate was 1 ºC/min below 600 ºC and 5 ºC/min after. To remove the hard silicate template, the sample was etched in 5 wt.% HF solution overnight twice under stirring, followed by washing with ethanol and deionized water. Finally, the carbon sample was dried for 24 hours at 100 ºC and additionally overnight at 300 ºC under dynamic vacuum. The final sample was transported without air exposure to an argon-filled glovebox for storage.

NCMK-3 produced using the nanocasting method [4]: In a typical process using Schlenk line techniques, 6.75 g EDA and 15 g CTC were added to a jacketed flask under stirring at RT. Next, 2.5 g SBA-15 silicate template was added to the mixture of EDA and CTC under stirring slowly. The resultant mixture was allowed to stir for 1 hour until a uniform white slurry was obtained. Under continuous stirring, the temperature was

increased to 90 ºC, at which the mixture was refluxed and stirred for 6 hours. The obtained brown colored solid mixture was placed in a drying oven at 100 ºC for 12 hours, and subsequently ground into a fine powder. Sample calcination was carried out in a tubular furnace under flowing nitrogen at 600 ºC for 5 hours. A ramp rate of 3 ºC/min was used to bring the sample up to 600 ºC. After calcination, the composite carbon/silica powder was immersed in 5 wt.% HF acid solution under stirring to dissolve the silica template. Carbon powder was recovered following filtration and several washings with ethanol and deionized water. Finally, the carbon sample was dried for 24 hours at 100 ºC and additionally overnight at 300 ºC under dynamic vacuum. The final sample was transported without air exposure to an argon-filled glovebox for storage.

• Nitrogen Sorption Supporting Information:

Scans were recorded on a Coulter SA3100 at 77 K.

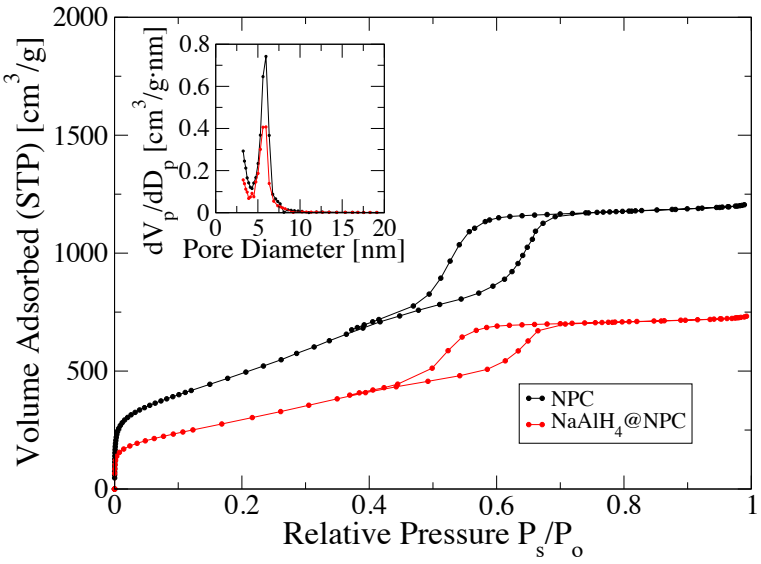

Figure S1. Nitrogen sorption isotherms and pore volume distributions (inset) for the NPC carbon substrate before and after infiltration with $NaAlH_4$. The decreased volume adsorbed over the whole of the isotherm indicates some portion of the available surface area is now inaccessible to the adsorbate, as a result of the filling or blocking of the substrate pores.

• PXRD Supporting Information:

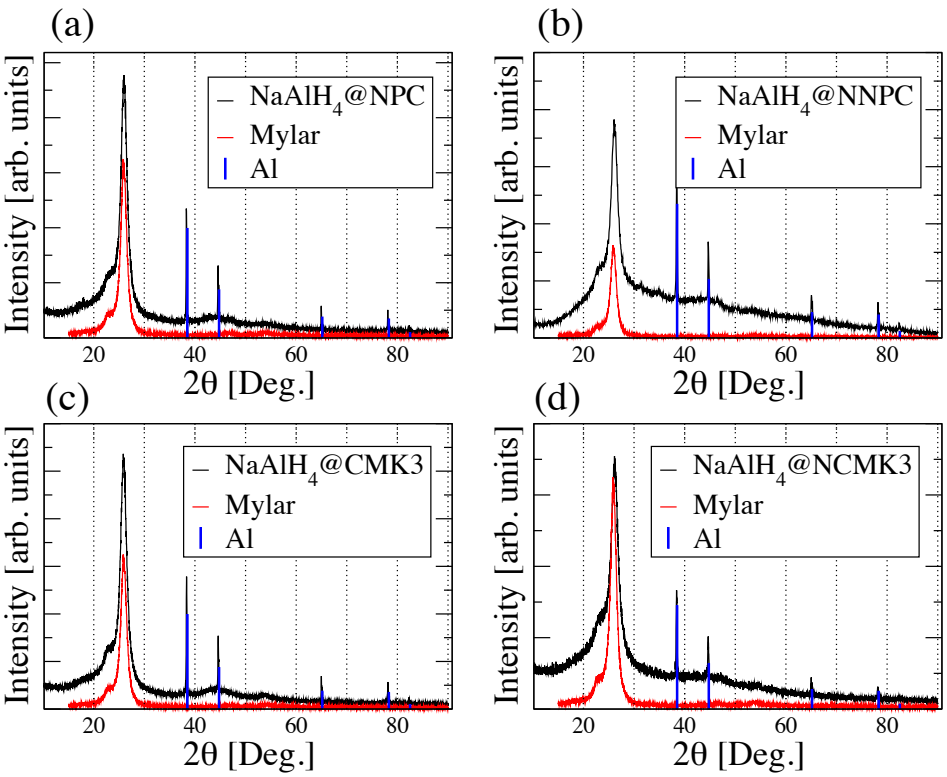

Figure S2. PXRD scans of infiltrated carbons: (a) NPC, (b) NNPC, (c) CMK-3, and (d) NCMK-3. Mylar film was used to cover the sample to avoid air exposure. No peaks from crystalline $NaAlH_4$ were detected, indicating the presence of little or no $NaAlH_4$ outside the pores, and indicating $NaAlH_4$ contained inside the pores is amorphous.

Table S1. $NaAlH_4$ and Al Metal Content of Infiltrated Carbon Scaffolds

Sample	$NaAlH_4$	Al metal	Al_2O_3
$NaAlH_4$@CMK-3	26.5%	73.5%	0%
$NaAlH_4$@NCMK-3	68.0%	32.0%	0%
$NaAlH_4$@NPC	89.2%	10.8%	0%
$NaAlH_4$@NNPC	20.1%	22.3%	26.9%

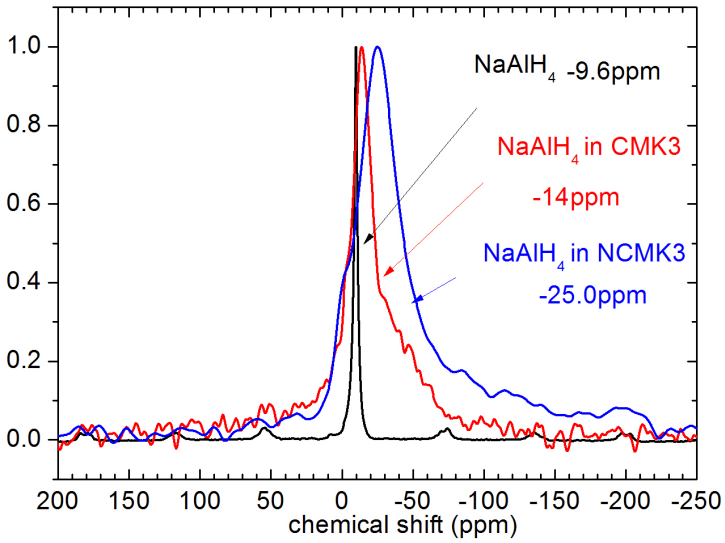

Figure S3. ^{23}Na 5 kHz MAS NMR spectra referenced to a 6 M NaCl solution showing measured chemical shifts for bulk $NaAlH_4$, $NaAlH_4$@CMK-3, and $NaAlH_4$@NCMK-3 indicating $NaAlH_4$ remains intact after confinement in the carbon scaffolds. The position of the observed $NaAlH_4$ line is consistent with previous studies of the bulk hydride [5].

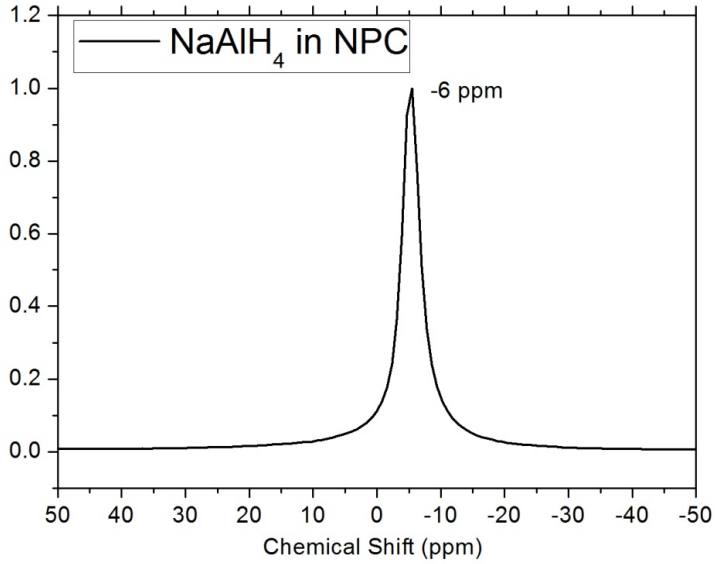

Figure S4. ^{23}Na 25 kHz MAS NMR spectra referenced to a 6 M NaCl solution at 156.022 MHz for $NaAlH_4$@NPC. The observed $NaAlH_4$ line position is consistent with previous studies of bulk $NaAlH_4$ [5].

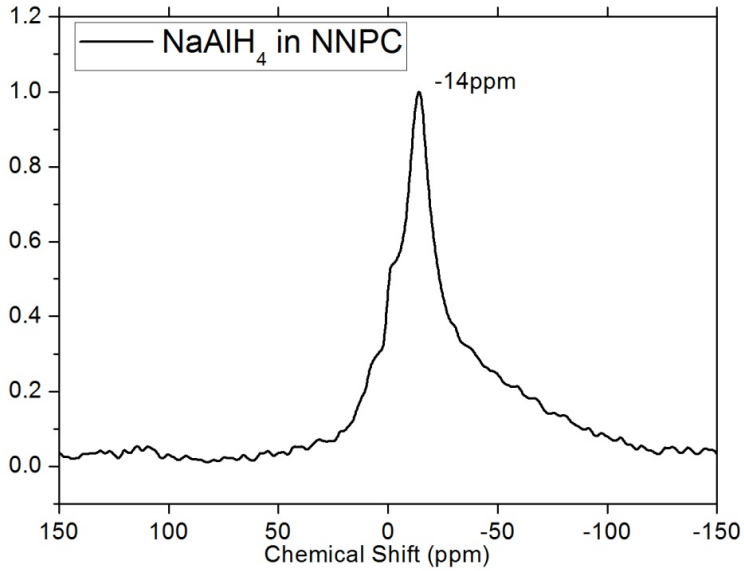

Figure S5. ^{23}Na 9 kHz MAS NMR spectra referenced to a 6 M NaCl solution at 79.27 MHz for $NaAlH_4$ in NNPC. The observed $NaAlH_4$ line position is consistent with previous studies of bulk $NaAlH_4$ [5].

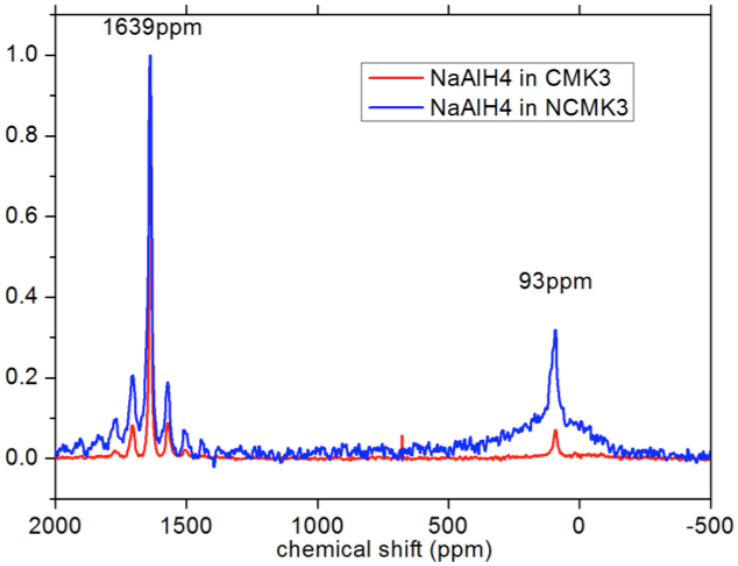

Figure S6. ^{27}Al 5 kHz MAS NMR referenced to 1 M $Al(NO_3)_3$ solution. $NaAlH_4$-infiltrated carbon samples have one Al metal peak at 1639 ppm and a $NaAlH_4$ peak at 93 ppm [5].

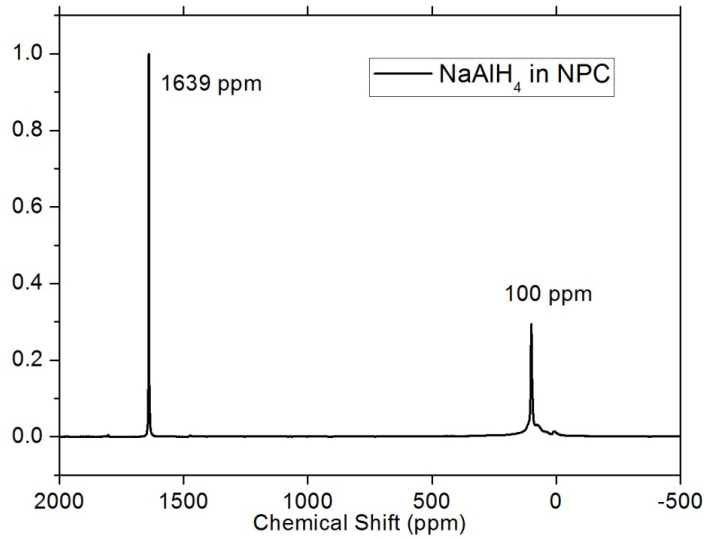

Figure S7. ^{27}Al 25 kHz MAS NMR referenced to 1 M $Al(NO_3)_3$ solution at 153.69 MHz for $NaAlH_4$@NPC. There is one Al metal peak at 1639 ppm and one $NaAlH_4$ peak at 100 ppm [5].

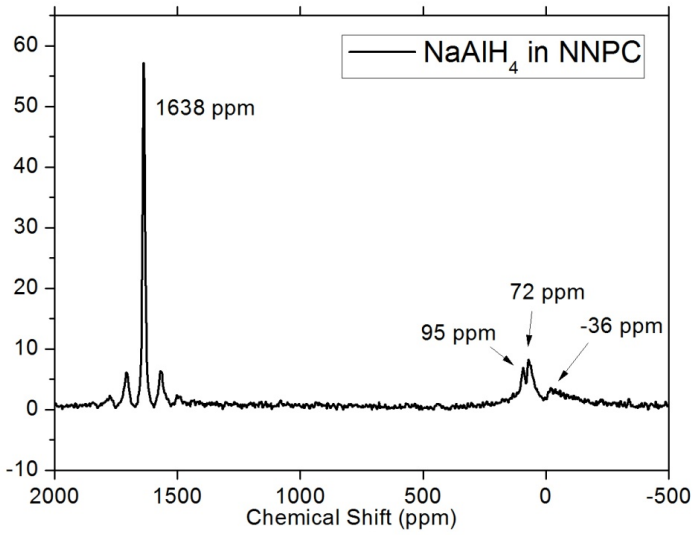

Figure S8. ^{27}Al 5 kHz MAS NMR referenced to 1 M $Al(NO_3)_3$ solution at 78.085 MHz. Although the samples are sealed in separate containers, some oxygen contamination is unavoidable given the surface areas and reactivity of the nanoparticle Al-containing phases. For this reason, peaks corresponding to Al_2O_3 are evident in the ^{27}Al spectra. There is still one Al metal peak at 1639 ppm and a $NaAlH_4$ peak at 95 ppm [5].

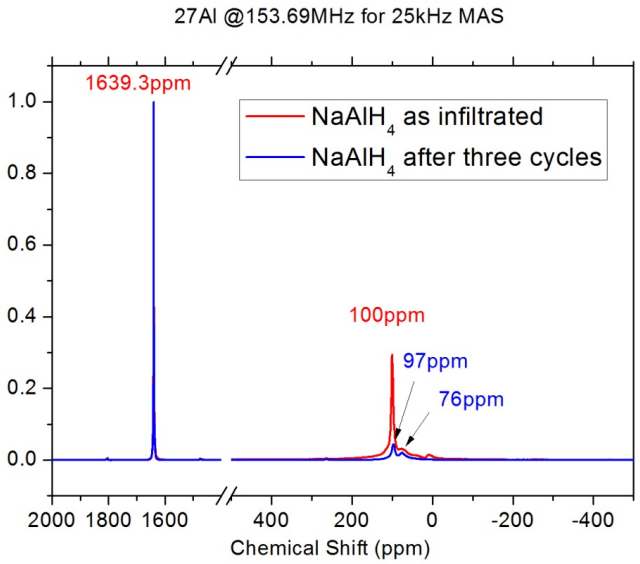

Figure S9. $NaAlH_4$@NPC as infiltrated and after three cycles ^{27}Al 25 kHz MAS NMR. Reference 1M $Al(NO_3)_3$ solution at 153.69 MHz. There is one Al metal peak at 1639 ppm and a $NaAlH_4$ peak at 97 ppm after 3 cycles [5]. Although the samples are sealed in separate containers, some oxygen contamination is unavoidable given the surface areas and reactivity of the nanoparticle Al-containing phases. For this reason, peaks corresponding to Al_2O_3 are evident in the ^{27}Al spectra.

• References:

[1] Liu, R.; Shi, Y.; Wan, Y.; Meng, Y.; Zhang, F.; Gu, D.; Chen, Z.; Tu, B.; Zhao, D. Triconstituent Co-Assembly to Ordered Mesostructured Polymer−Silica and Carbon−Silica Nanocomposites and Large-Pore Mesoporous Carbons with High Surface Areas. *J. Am. Chem. Soc.* **2006**, 128, 11652–11662.

[2] Song, Y.; Li, L.; Wang, Y.; Wang, C.; Guo, Z.; Xia, Y. Nitrogen-Doped Ordered Mesoporous Carbon with a High Surface Area, Synthesized through Organic-Inorganic Coassembly, and Its Application in Supercapacitors. *ChemPhysChem* **2014**, 15, 2084–2093.

[3] Jun, S.; Joo, S. H.; Ryoo, R.; Kruk, M.; Jaroniec, M.; Liu, Z.; Ohsuna, T.; Terasaki, O. Synthesis of New, Nanoporous Carbon with Hexagonally Ordered Mesostructure. *J. Am. Chem. Soc.* **2000**, 122, 10712–10713.

[4] Vinu, A.; Ariga, K.; Mori, T.; Nakanishi, T.; Hishita, S.; Golberg, D.; Bando, Y. Preparation and Characterization of Well-Ordered Hexagonal Mesoporous Carbon Nitride. *Adv. Mater.* **2005**, 17, 1648–1652.

[5] Bogdanović, B.; Felderhoff, M.; Germann, M.; Härtel, M.; Pommerin, A.; Schüth, F.; Weidenthaler, C.; Zibrowius, B. Investigation of Hydrogen Discharging and Recharging Processes of Ti-Doped $NaAlH_4$ by X-Ray Diffraction Analysis (XRD) and Solid-State NMR Spectroscopy. *J. Alloys Compd.* **2003**, *350*, 246–255.

SECTION

4. COMPARING $[BH_4]^-$ ANION MOBILITY OF $LiBH_4$ CONFINED IN SURFACE FUNCTIONALIZED AND NON-FUNCTIONALIZED NANOPOROUS CARBON SCAFFOLDS VIA QUASIELASTIC NEUTRON SCATTERING

Unlike x-ray photons that are scattered by atomic electrons, neutrons scatter from atomic nuclei within the sample. As a consequence, whereas x-ray scattering is not very sensitive to low Z elements (i.e. hydrogen), the scattering cross section for neutrons is dictated by the interaction with the nuclear potential, resulting in scattering cross sections that vary widely over the periodic table. Moreover, the lack of electric charge combined with the small characteristic range of the nuclear force (~femtometers) allows neutrons to penetrate deeply or pass through materials normally opaque to x-rays, allowing more latitude in controlling the sample environment of the designed experiment.

Most scattering techniques utilize cold or thermal neutrons with energies and wavelengths on the order of meV and Å respectively at room temperature, which are comparable to the excitation energies and interatomic spacing of condensed matter, allowing dynamics to be studied as both a function of space and time on the atomic scale during a single measurement [86]. Unfortunately, neutron sources generally supply a flux of neutrons that is small compared to other scattering techniques. The weaker scattering interaction of neutrons and the low incident flux result in small scattering intensity signals, limiting the usefulness of the technique. Despite the challenges, neutron scattering provides information about materials that cannot be elucidated by other techniques. To alleviate the problem to some degree, instruments have been designed to increase the signal intensity of certain scattering information at the expense of another. Often samples must be measured on multiple instruments to access the full spectrum of the system's dynamics.

Hydrogen has an inherently large incoherent scattering cross section, making neutron scattering an ideal technique for studying hydrogen storage materials. In particular, $LiBH_4$ confined in porous scaffolds has been extensively studied using a

variety of neutron scattering techniques [87-90]. In a study by Remhof et al. quasielastic neutron scattering (QENS) measurements revealed $LiBH_4$ confined in high surface area graphite (HSAG) exists within the pores in two distinct phases displaying different levels of $[BH_4]^-$ anion reorientational mobilities [89]. Though unable to definitively determine the foundation of each phase, the authors suggested the two phases could be described in terms of a core and interfacial region within the scaffold pore, where phase mobility is determined by the interaction of $LiBH_4$ with the pore wall [89]. In one case, $LiBH_4$ near the pore wall becomes immobilized with a high mobility population residing at the pore's core region, or alternatively the roles reverse with the interaction at the pore wall resulting in enhanced mobility in the interfacial region with instead an immobile bulk-like core region [89]. Subsequent studies of $LiBH_4$ in ordered NPC with average pore diameters of 2 and 4 nm also identified two populations of $LiBH_4$ using QENS and were able to determine the highly mobile $[BH_4]^-$ anions belonged to the $LiBH_4$ in closest proximity to the pore walls, while a slower more bulk-like population occupies the pore interior [87,88].

In the studies of nanoconfined $LiBH_4$ discussed above [87-89] the interaction of $LiBH_4$ with the carbon scaffold has a significant impact on the observed dynamics. Infiltration induced strain [89], pore size, and chemical makeup of the scaffold [87-89] have all been speculated to be important factors that could describe the hydride/carbon scaffold interaction. Until recently, there have not been many studies specifically targeted to determine how the chemical nature of the confining scaffold affects the infiltrated metal hydride's behavior [90,91]. Work by Suwarno and co-workers investigated $LiBH_4$ confined in both carbon and silica scaffolds with similar pore sizes and geometries to determine how the chemical aspect of the scaffolds would affect the observed dynamics [90]. $LiBH_4$ confined in the silica scaffold displayed a larger solid-solid phase transition depression in addition to a thicker non-bulk like hydride layer at the scaffold/hydride interface in comparison to the carbon scaffold system; together demonstrating the scaffold's chemical makeup plays a significant role in the altered dynamics [90].

In this work, QENS and neutron vibrational spectroscopy (NVS) were used to investigate $LiBH_4$ confined in both nitrogen-functionalized/non-functionalized carbon

scaffolds with similar physical characteristics to determine how functionalization of the scaffold surface with nitrogen affects the dynamics of the confined hydride. CMK-3 and NPC type nitrogen-functionalized/non-functionalized scaffold pairs were measured to explore the role pore geometry may have in the systems.

4.1. EXPERIMENTAL METHODS

Isotope enriched $^{7}Li^{11}BH_4$ was used exclusively in these studies to increase the transmission of neutrons with respect to a naturally occurring $LiBH_4$ sample containing the strong neutron absorbing isotopes ^{6}Li and ^{10}B. Carbon scaffolds and infiltrated samples were prepared following the procedures outlined in Section 3. Physical characterization of the scaffolds used here were reported in Paper I. Prior to scattering measurements, samples were loaded into an Al measurement vessel and sealed with indium foil in a helium filled glovebox to avoid air exposure.

4.1.1. Neutron Vibrational Spectroscopy. Vibrational density of states measurements were carried out in neutron energy loss at 4 K using the Filter-Analyzer Neutron Spectrometer (FANS) [92]. In the vibrational energy range of 34 to 200 meV measured, pre and post-monochromator collimations of 60′ and 40′ resulted in an energy resolution between 1.5 and 16 meV.

4.1.2. Quasielastic Neutron Scattering. Local bonding and dynamics of $LiBH_4$ confined in nitrogen-functionalized/non-functionalized carbon scaffolds were investigated with quasielastic neutron scattering on the high-flux backscattering spectrometer (HFBS) [93] and disk chopper spectrometer (DCS) [94] at NIST. The recorded spectra were reduced and analyzed with the DAVE software package [95].

4.1.2.1 High flux backscattering spectrometer. Fixed window scans (FWS) in a temperature range of 4 to 275 K were recorded to determine the temperatures at which the dynamics of the measured samples are observable. Quasielastic neutron scans were taken with momentum transfers (Q) of range 0.2 to 1.75 $Å^{-1}$, with an incident neutron wavelength of 6.27 Å (2.08 meV) and a full width at half maximum (FWHM) detector energy resolution of 0.8 μeV.

4.1.2.2 Disk chopper spectrometer. Quasielastic neutron scans at specified temperatures were recorded using incident neutron wavelengths of 5 Å (3.3 meV) and FWHM elastic line widths of 50.1 μeV and 105.5 μeV, and 8 Å (1.3 meV) and a FWHM elastic line width of 14.3 μeV.

4.1.3. Prompt Gamma Activation Analysis. Carbon scaffolds were measured using a cold neutron source on a dedicated beam line at the NIST facility [96]. The carbon, hydrogen, and nitrogen relative peak areas of a standard urea/graphite mixture were compared with those of the carbon scaffold to determine the respective elemental ratios in the sample.

4.2. RESULTS AND DISCUSSION

Before beginning the QENS study, vibrational neutron spectra were recorded at 4 K in energy loss for both the bare and $LiBH_4$ infiltrated carbon scaffolds. Figure 4.1 displays the measured spectra of the empty carbon scaffolds. Due to the large scattering cross-section of hydrogen in relation to ^{11}B and ^{12}C, the recorded spectra represents the vibrational density of states (DOS) of the remaining hydrogen bonded to the scaffold. As a guideline, previous prompt gamma measurements of similar NPC-type carbon substrates synthesized from phenol/formaldehyde resol precursors reported a H/C ratio of ~0.1 [88]. In comparison, the NCMK-3 scaffold measured as part of this work had a H/C ratio approaching 0.2, most likely the result of the lower carbonization temperature during synthesis. All four scaffolds show similar spectra, displaying vibrational modes characteristic of sp^2 bonded H atoms as reported for coronene [97]. Figure 4.2 shows the vibrational neutron spectra for $LiBH_4$ confined in the respective carbon scaffolds after proper subtraction of the contributions from the carbon scaffold. For comparison, data for bulk $LiBH_4$ measured on the FANS instrument previously reported by Verdal et al. is shown [88]. Torsional (~52 meV) and bending (125 - 175 meV) modes are present in the bulk $LiBH_4$ spectra [88]. In comparison, all four spectra of nanoconfined $LiBH_4$ show broadening of the torsional peak at 52 meV indicating some portion of the $[BH_4]^-$ anions experience rotational potentials markedly different from the bulk sample. Upon infiltrati-

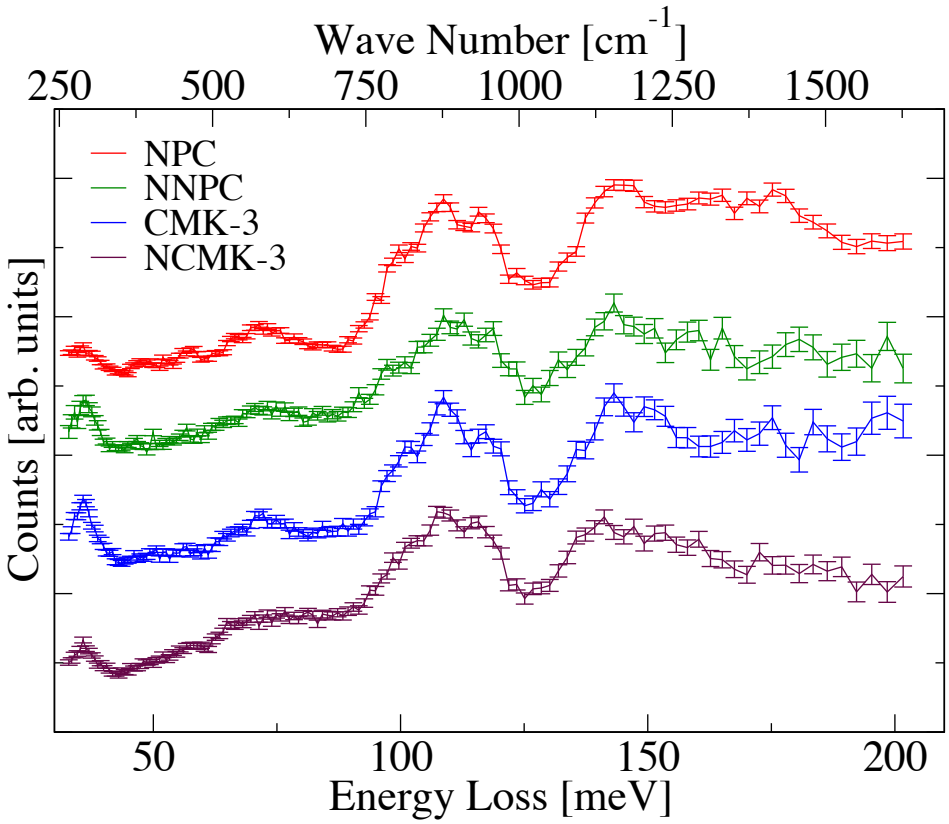

Figure 4.1. Vibrational neutron spectra of empty carbon scaffolds at 4 K.

on there is not much change in the potentials related to the bending modes with the exception of $LiBH_4$@NCMK-3, where the peak appearing at ~140 meV is greatly attenuated. No firm explanation for the attenuation was identified at this time, though it should be noted the NCMK-3 scaffold does contain the highest nitrogen and residual hydrogen content in comparison with the other scaffolds. Some combination of these factors may be responsible for the observed behavior.

In a QENS experiment the scattering intensity is measured as a function of momentum transfer ($\hbar Q$) and small energy transfers ($\hbar\omega$) in the range of neV-μeV. Generally, the QENS signal is a result of diffusive molecular and atomic processes

occurring on a timescale of 10^{-13} – 10^{-7} s [86]. The measured scattering intensity is proportional to the double differential cross section [86]

$$\frac{d^2\sigma}{d\Omega d\omega} = \frac{k_f}{k_i}\left[\frac{\sigma_{coh}}{4\pi}S_{coh}(Q,\omega) + \frac{\sigma_{inc}}{4\pi}S_{inc}(Q,\omega)\right] \quad (1)$$

with k_f and k_i the wave number of the scattered and incident neutrons respectively. Incoherent scattering will dominate the measured intensity signal in the work presented here due to the excessively large incoherent scattering cross section of hydrogen (σ_{inc}) relative to lithium or boron. In this regard the total scattering intensity is approximated

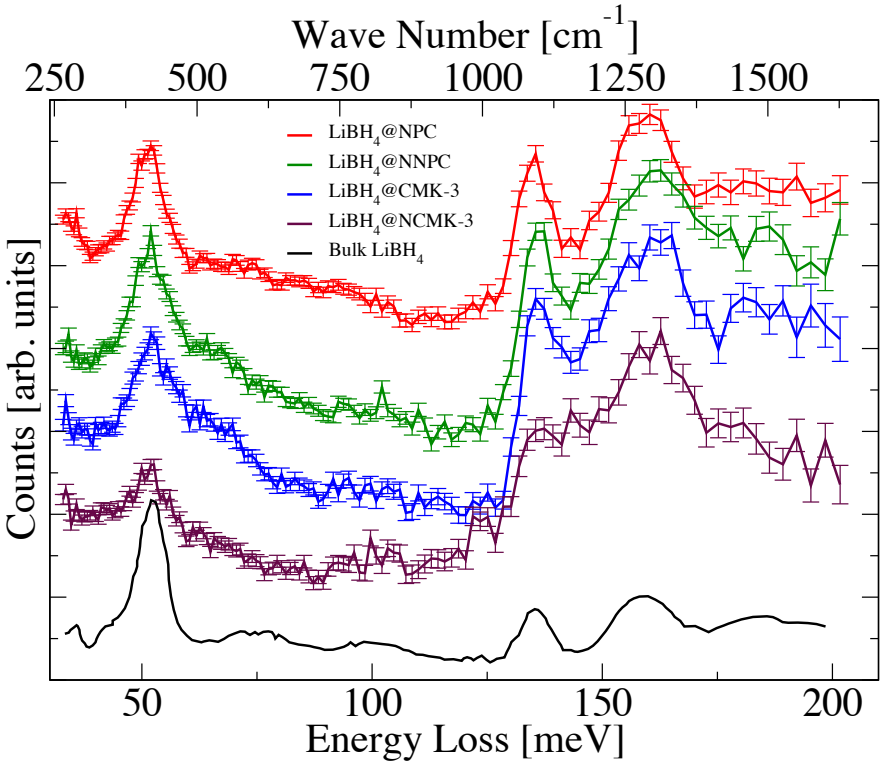

Figure 4.2. Vibrational neutron spectra of $LiBH_4$ confined in carbon scaffolds. Data for bulk $LiBH_4$ was taken from Verdal et al. [88].

to result from incoherent scattering from hydrogen, ignoring the contribution of scattering from Li, B, and additionally any coherent scattering. Collected spectra were reduced using DAVE [95] software to yield the incoherent scattering function $S_{inc}(Q,\omega)$. A typical QENS spectra consists of an instrumental resolution function convolved with an elastic scattering contribution at zero energy transfer modeled by a delta function $\delta(\omega)$ in addition to a quasielastic feature modeled by one or more Lorentzian functions $L_i(\omega)$ that appear as a broadening of the elastic line. With the proposed model the incoherent scattering function can be represented by [88]

$$S_{inc}(Q\,,\omega) = A_0(Q)\delta(\omega) + \sum A_i(Q)L_i(\omega) \qquad (2)$$

where the elastic incoherent structure factor (EISF) can be calculated from the ratio of the elastic peak area $A_0(Q)$ to the entire area of the measured scattering $(A_0(Q) + \sum A_i(Q))$ at a specific Q value [88].

In order to estimate the onset of dynamics in the system that will be observable in the available energy window of the spectrometer, FWS were recorded before beginning any quasi-elastic measurements. During FWS the energy of the incoming and scattered neutrons is fixed, and the elastic scattering intensity is measured as a function of an external variable, in this case temperature. Motions occurring on a timescale slower than the instrument energy window cannot be resolved and appear within the set elastic window corresponding with the resolution of the spectrometer. As the temperature is increased the dynamics of the system being measured occur on a faster timescale, eventually producing scattering that appears outside the elastic energy window, resulting in a decrease of the measured elastic scattering intensity. FWS of the nanoconfined $LiBH_4$ taken on the HFBS are shown in Figure 4.3. Data for bulk $LiBH_4$ was taken from Liu et al. and is shown for comparison [87]. Elastic scattering intensity begins to decrease sharply for the nanoconfined $LiBH_4$ at ~50 K marking the onset of $[BH_4]^-$ anion mobility, roughly 100 K before a comparable drop is evident in the bulk spectra. Clearly the transition to dynamic behavior is more step-like in nature for the bulk material compared

to the confined samples, where the transition occurs over a larger temperature range, indicating $[BH_4]^-$ anions experience a wide spread in rotational potentials. Interestingly, the spectra of all the confined samples displayed similar behavior despite the chemical differences of the scaffold surfaces, suggesting either confinement induced disorder plays a more significant role in the $[BH_4]^-$ dynamics or the influence of the surface chemistry results in a difference in dynamical behavior that lies outside the resolvable energy window of the particular spectrometer.

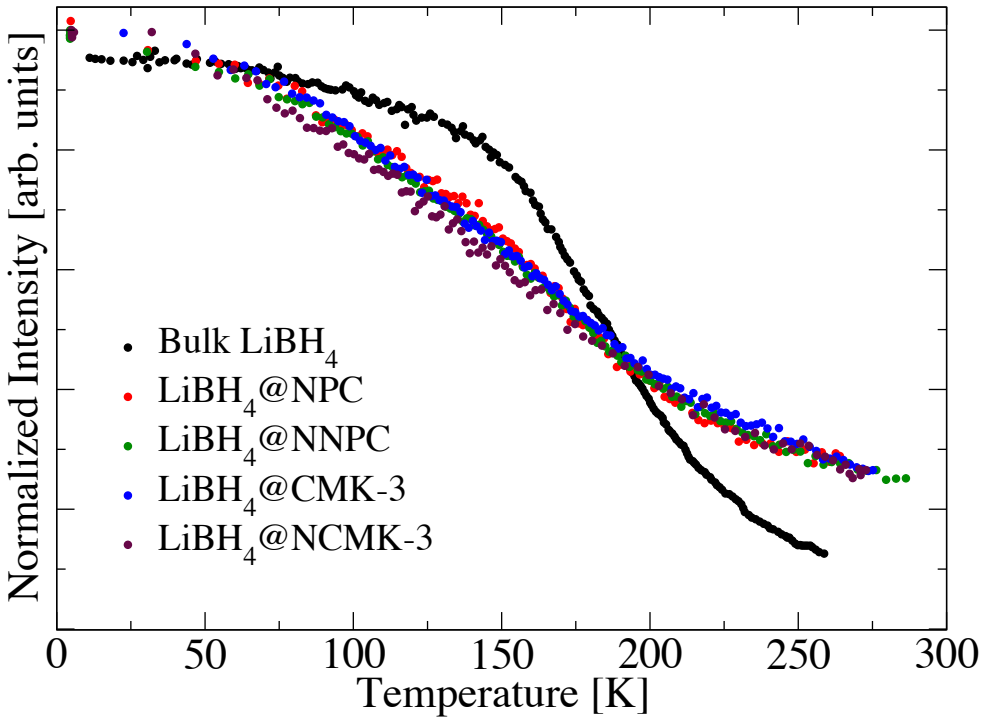

Figure 4.3. Fixed window scans of bulk $LiBH_4$ and $LiBH_4$ confined in carbon scaffolds. Data for bulk $LiBH_4$ was taken from Liu et al. [87].

To investigate the dynamics, quasielastic spectra were recorded on the HFBS in the temperature range of 4 to 165 K for each of the four nanoconfined $LiBH_4$ samples. A representative quasielastic spectrum taken on the HFBS is presented in Figure 4.4. Data

recorded in all of the spectra throughout the temperature range sampled were best fit by a model consisting of a delta function, Lorentzian, and background, which represent the elastic scattering, a single quasielastic feature, and scattering appearing as background, respectively, all convolved with an instrumental resolution function as shown in Figure 4.4. In contrast, the measured DCS spectra of $LiBH_4$ confined in NPC/NNPC required a model containing two distinct quasielastic features represented by Lorentzian functions. An example of the DCS spectra obtained for the $LiBH_4$@NNPC and $LiBH_4$@NPC samples is given in Figure 4.5. Each of the two Lorentzians modeling the quasielastic

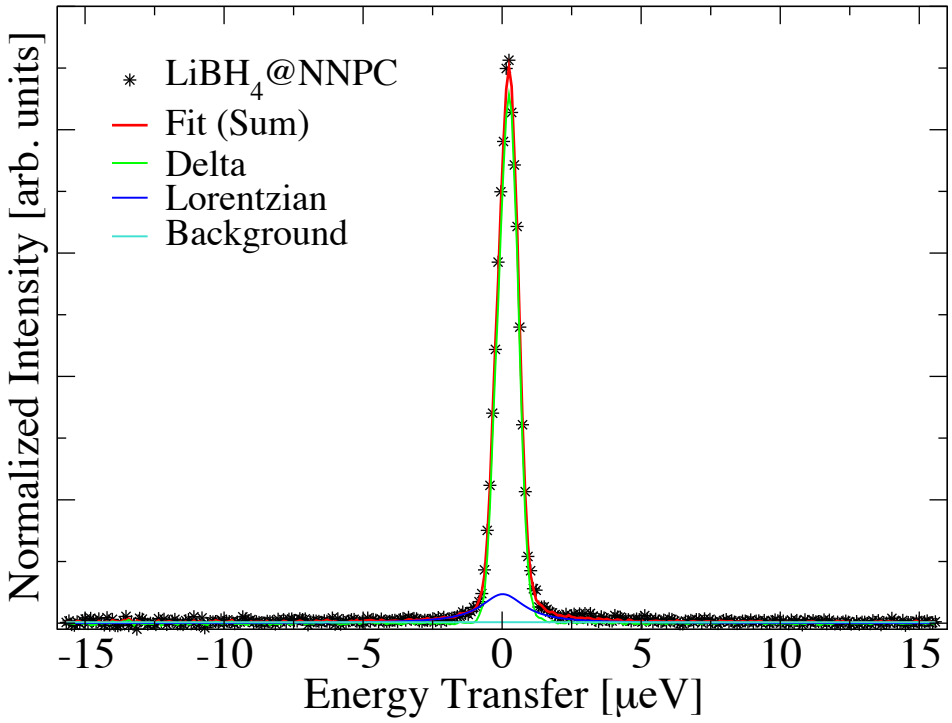

Figure 4.4. A representative HFBS quasielastic neutron scattering spectrum for $LiBH_4$ confined in carbon scaffolds. A model consisting of a delta function, one Lorentzian, and a background contribution produced the best-fit for all the measured spectra.

features and the delta function representing the elastic feature, all convolved with the instrumental resolution function, have been shaded to display the contribution of each component to the overall scattering function. Clearly the two quasielastic features are very different, characterized by FWHM line widths almost an order of magnitude in difference.

As discussed in the introduction, a previous study of $LiBH_4$ confined in ordered nanoporous carbon with features similar to the NPC/NNPC used in this work revealed DCS spectra best fit by a model with two different quasielastic features and additionally HFBS spectra with the presence of only a single quasielastic component, in agreement with the findings presented here [88]. In that work a core-shell model was suggested, w-

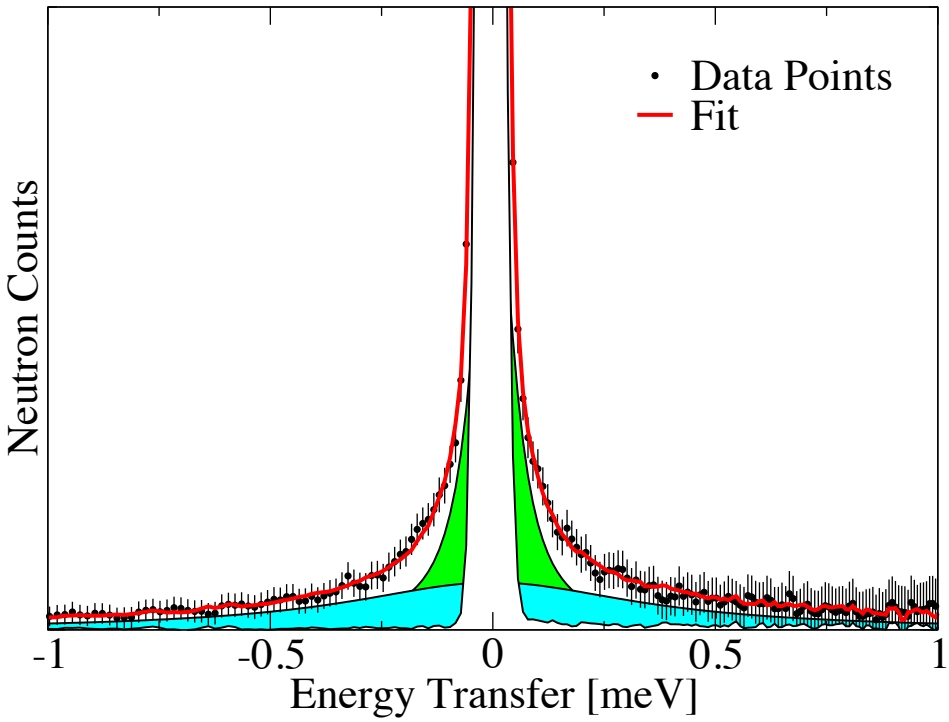

Figure 4.5. Example of the DCS spectra obtained for the $LiBH_4$@NPC and $LiBH_4$@NNPC samples showing the best-fit model to the experimental data (red), composed of an instrumental resolution function (not shown) convolved with a delta function (white), and two Lorentzians (blue and green) representing distinct quasielastic features.

ith a population of the $[BH_4]^-$ anions belonging to a shell of $LiBH_4$ at the scaffold/hydride interface that displayed faster reorientational dynamics than those anions in a more bulk-like core region [88]. Observation of only a single quasielastic component from the HFBS measurements was thought to result from a portion of the system dynamics occurring outside the available energy window of the HFBS, which only provides energy transfers of +/- 17 μeV from the elastic line with a resolution of ~1 μeV [88]. Given this small window and the order of magnitude difference in the quasielastic feature widths of the two components determined from the DCS, it is unlikely both dynamics could be observed on the HFBS at a specific temperature [88]. As determined from the FWS presented in Figure 4.3, the onset of dynamics in the confined sample occurs around 50 K. If one assumes a more bulk-like population within the pore would display an onset of dynamics at a temperature similar to the bulk, occurring around 150 K in Figure 4.3, then in this case the single quasielastic component observed at temperatures less than ~150 K should be associated with the faster reorienting shell component in the model suggested by Verdal et al. [88], and the slower bulk-like component would appear as elastic scattering. As the temperature is increased it is possible the line width of the faster dynamic broadens to the point it is outside the spectrometer's energy window, appearing as background. Any quasielastic feature observed at that point would be attributed to the appearance of the component associated with the bulk-like dynamic. Verdal et al. indicated the line width obtained from the HFBS at 200 K agreed well with the measured line width of the bulk-like component at the same temperature on the DCS [88]. In the current work only temperatures of 165 K and below were measured on the HFBS, not allowing confirmation of a similar observation around 200 K.

Interestingly unlike $LiBH_4$ confined in NPC/NNPC, the DCS spectra of the $LiBH_4$@CMK-3 and $LiBH_4$@NCMK-3 samples were fit best with a model consisting of only one quasielastic feature at all the temperatures measured, similar with the HFBS data. CMK-3 and NCMK-3 scaffolds have a pore geometry that is the inverse replica of the SBA-15 silica template that has cylindrical pores analogous to the NPC type scaffolds, resulting in pores that are slit-like in nature after removal of the silica template. It is likely the different pore geometry contributes to the measurement of only one

dynamic during the QENS measurements. Pores more slit-like in shape may not facilitate a substantial core region isolated from the scaffold wall influence as proposed in the cylindrical case, resulting in the observation of only the faster dynamic. FWS revealed very similar onset temperatures for reorientations of $LiBH_4$ confined in all four carbon scaffolds, suggesting the single dynamic observed on the HFBS for the $LiBH_4$@CMK-3 and $LiBH_4$@NCMK-3 samples likewise belongs to the faster dynamic associated with $[BH_4]^-$ anions in the vicinity of the scaffold as discussed for the NPC/NNPC systems.

As the temperature is increased during a QENS experiment the width of the measured quasielastic feature broadens as the reorientational jump rate increases, often displaying Arrhenius type behavior. The quantity $1/\tau$ is directly proportional to the HWHM of the quasielastic feature, where τ is the residence time between jumps. An activation energy E_a for a reorientational jump can be obtained from a fit to an Arrhenius equation of the form

$$\frac{1}{\tau} = \frac{1}{\tau_0} e^{-\frac{E_a}{k_B T}} \tag{4}$$

with $k_B = 8.617 \times 10^{-5}$ eV/K the Boltzmann constant and τ_0 the apparent residence time as $T \rightarrow \infty$. An Arrhenius plot in Figure 4.6 displays the fit to the quasielastic data taken during measurements on the DCS at temperatures in the range 200 - 300 K. At each temperature the HWHM of the respective quasielastic feature was determined from an average over Q. Data for bulk $LiBH_4$ was taken from Verdal et al. and shown for comparision [88]. Table 4.1 lists the residence times τ_0 and the activation energies for reorientational jumps determined from the best-fit line to the data calculated using linear regression. In Table 4.1 component 1 is referenced to the quasielastic feature equated with more bulk-like behavior and component 2 is associated with the faster dynamic in the NPC/NNPC systems. There is a good agreement between the measured $LiBH_4$@NPC and $LiBH_4$@NNPC sample $[BH_4]^-$ reorientational activation energies of the bulk-like component, with values of 7.8 and 7.9 kJ/mol respectively. Despite the correlation between samples here, the measured values are low compared with the 16 and 14.4

kJ/mol reported by Verdal et al. for the bulk-like component of $LiBH_4$ in nanoporous carbons with 4 and 2 nm average pore sizes [88]. Though the main mesopores are similar in geometry and pore shape to the NPC's in Verdal et al. [88], the NPC/NNPC used here contains a large micropore distribution below 2 nm as the result of etching silica from the pore walls after carbonization. Moreover, the NPC/NNPC here exhibit surface area and pore volumes of $> 1400\ m^2/g$ and $> 1.3\ cm^3/g$, compared to $730\ m^2/g$ and $0.53\ cm^3/g$ for 4 nm NPC used in Verdal et. al [88]. It is difficult to uniquely determine how the differences in physical aspects of the substrates will modify the current results in relation to previous studies, but here the differences in the NPC/NNPC and CMK-3/NCMK-3 scaffold pairs were minimized in an attempt to elucidate how the chemical nature of the scaffold surface affects the dynamics of the confined $LiBH_4$. It is interesting that in both cases higher activation energies were measured for reorientations of $[BH_4]^-$ anions in the nitrogen-functionalized scaffold in comparison to its non-functionalized counterpart. The measured difference in activation energy of $LiBH_4$@NPC and $LiBH_4$@NNPC was for the faster dynamic component referenced with the $LiBH_4$/scaffold interfacial region, in contrast to the difference in activation energy measured for the single quasielastic component of the $LiBH_4$@CMK-3 and $LiBH_4$@NCMK-3 systems that appears to more closely resemble the bulk-like component.

In the study of $LiBH_4$ confined in surface functionalized carbon scaffolds presented in Paper I the addition of nitrogen to the scaffolds was found to stabilize the decomposition of $LiBH_4$ to higher temperatures, with measured activation energies for the desorption of hydrogen 30 kJ/mol or greater in the systems functionalized with nitrogen compared to the base non-functionalized system [91]. In that work, the observed increase of the desorption activation energy in the nitrogen-functionalized systems was thought to be associated with the formation of a stabilizing capping layer during the $LiBH_4$ infiltration process that is the result of Lewis acid/Lewis base interactions of borane (BH_3), with pyridinic nitrogen in the pore wall surface [91]. In relation to the current QENS study, it is of interest to consider how, if present, a capping layer containing borane might alter the observation of dynamics with QENS. A decomposition

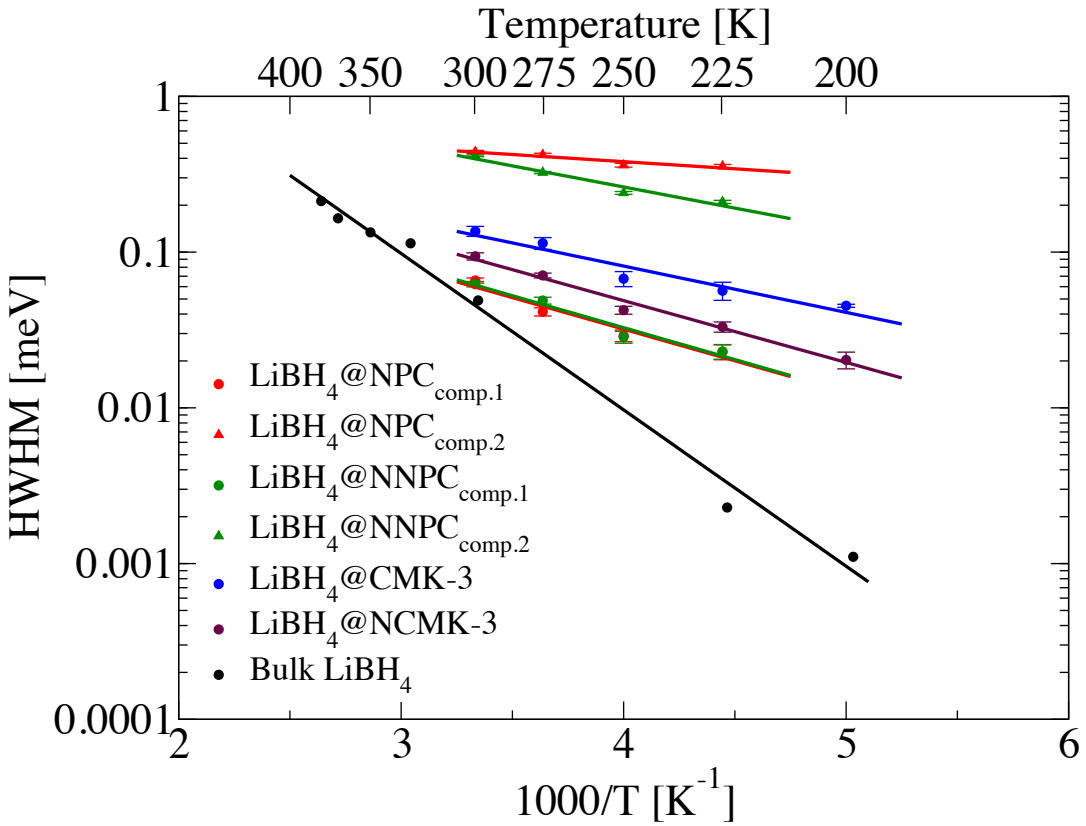

Figure 4.6. Arrhenius plot displaying the fit to the quasielastic data taken during measurements on the DCS. Data for bulk $LiBH_4$ was taken from Verdal et al. [88] and shown for comparison.

Table 4.1. $[BH_4]^-$ Reorientational Activation Energies and Residence Times Determined from QENS Measurements

sample	$E_{a\ comp.1}$ [kJ/mol]	τ_0 [fs]	$E_{a\ comp.2}$ [kJ/mol]	τ_0 [fs]
$LiBH_4$@NPC	7.8 ± 1.3	0.5 ± 0.3	1.8 ± 0.4	0.7 ± 0.2
$LiBH_4$@NNPC	7.9 ± 1.2	0.5 ± 0.3	5.2 ± 0.8	0.2 ± 0.1
$LiBH_4$@CMK-3	5.7 ± 0.9	0.5 ± 0.2	-	-
$LiBH_4$@NCMK-3	7.6 ± 0.6	0.3 ± 0.1	-	-

mechanism for $LiBH_4$ was predicted from first-principles calculations involving the creation of structure vacancies at the materials surface by the removal of $[BH_4]^-$ and/or BH_3 units allowing H^- species to diffuse into the bulk and act as nucleation sites for the formation of LiH [98]. Moreover, the calculations indicate the decomposition of $LiBH_4$ can only be sustained if $[BH_4]^-$ and/or BH_3 are transported to the surface of the hydride, where $[BH_4]^-$ unstable outside the hydride, further decomposes to BH_3 and H^- [98]. If it is assumed a capping layer did form in the nitrogen-functionalized systems during infiltration, then it is probable there is a reduced amount of $LiBH_4$ in close proximity to the pore wall, minimizing the scaffold induced affects that seem to produce enhanced $[BH_4]^-$ reorientational dynamics. It seems likely in this case a portion of the $LiBH_4$ normally displaying the faster dynamic in a physically similar non-functionalized carbon scaffold would now have a measured dynamic shifted toward the more bulk-like dynamic. Although the data here cannot firmly establish this conjecture is correct, the higher measured $[BH_4]^-$ reorientational activation energies do support the notion of the faster dynamic becoming more bulk-like for the nitrogen-functionalized carbon systems. A thorough investigation of the EISF could provide insight into whether a different reorientational mechanism is present in the nitrogen-functionalized systems, but is beyond the scope of the present investigation. Accurate determination of the EISF for these samples will also require NMR measurements to determine the fraction of the confined $LiBH_4$ that is intact after the infiltration process, where some fraction transforms to non $[BH_4]^-$ forms of boron within the scaffold as determined in previous studies [87]. After determining the amount of intact $LiBH_4$ with ^{11}B MAS NMR the elastic scattering contribution from the carbon scaffold, ^7Li, and ^{11}B can be removed from the incoherent scattering intensity to isolate scattering from nanoconfined $LiBH_4$, allowing the correct calculation of the EISF.

4.3. STUDY CONCLUSIONS

Neutron scattering measurements were performed on $LiBH_4$ confined in nitrogen-functionalized and non-functionalized carbon scaffolds with similar physical characteristics in an attempt to understand the affect functionalizing a carbon scaffold

surface with nitrogen has on the measured $LiBH_4$ dynamics. Matched nitrogen-functionalized/non-functionalized carbon scaffolds of two types were used in the study, CMK-3 type carbon with slit-like pores, and NPC type carbon with cylindrical pores. Vibrational neutron spectroscopy revealed $[BH_4]^-$ anions associated with confined $LiBH_4$ experience a broader distribution of rotational potentials with respect to the bulk hydride, as evidenced by a substantially broadened torsional mode peak at 52 meV. Fixed window scans indicated the onset of $[BH_4]^-$ reorientations begins by ~50 K when $LiBH_4$ is confined in the carbon scaffolds, approximately 100 K before the 150 K onset noted for bulk $LiBH_4$. Quasielastic neutron spectra from the HFBS suggested the presence of a single quasielastic feature in agreement with a previous similar study [88]. DCS measurements produced spectra for the $LiBH_4$@NPC and $LiBH_4$@NNPC samples indicative of two quasielastic features with an order of magnitude difference in line widths. The distinct features are thought to represent slower reorientating $[BH_4]^-$ anions from bulk-like $LiBH_4$ near the center of the cylindrical pore, and faster reorientating $[BH_4]^-$ anions of the $LiBH_4$ near the pore wall. In contrast, a single quasielastic feature was found from the DCS data for $LiBH_4$@CMK-3 and $LiBH_4$@NCMK-3, where slit-like pores may not be cohesive to producing two dynamics with enough difference to be distinguishable with the QENS measurements taken here.

An Arrhenius analysis of the DCS data resulted in calculated activation energies for $[BH_4]^-$ reorientations of 1.8 ± 0.4 and 5.2 ± 0.8 kJ/mol for the faster quasielastic component in $LiBH_4$@NPC and $LiBH_4$@NNPC respectively, and 5.7 ± 0.9 and 7.6 ± 0.6 kJ/mol for the single quasielastic component of $LiBH_4$@CMK-3 and $LiBH_4$@NCMK-3 respectively. The slower bulk-like component of $LiBH_4$@NPC and $LiBH_4$@NNPC were consistent with each other with measured values of 7.8 ± 1.3 and 7.9 ± 1.2 kJ/mol. Across the samples, $LiBH_4$ in the nitrogen-functionalized scaffolds experienced a higher activation energy for reorientations than its corresponding non-functionalized counterpart. Together the results suggest the chemical makeup of the confining carbon scaffold influences the properties of the confined metal hydride and may provide a beneficial way to further modify metal hydride based hydrogen storage systems.

4.4. ACKNOWLEDGEMENTS

A special thanks to Terry Udovic and Mirjana Dimitrievska of the NIST NCNR for their assistance in collecting the neutron data and financial support from NSF IGERT: Neutron Scattering for the Science and Engineering of the 21st Century under award number 1069091 administered through University of Missouri in Columbia, MO.

5. INVESTIGATION OF SOLID SOLUBILITY IN THE NaH/NaOH SYSTEM USING IN-SITU X-RAY DIFFRACTION

Hydrogen sorption in complex metal hydride systems is governed by solid-state reactions, often consisting of multiple steps and involving the presence of several hydride phases, in addition to pure metals and gaseous hydrogen. Decomposition of $NaAlH_4$ occurs in two steps producing both phase separated Na_3AlH_6 + Al and NaH + Al. To reversibly store hydrogen, segregated species must be recombined into the proper stoichiometric combinations. The addition of a small amount of titanium has been shown to facilitate reversible hydrogen storage in $NaAlH_4$ [28,29], though the exact mechanism responsible for the improved cycling is not fully understood. Experimental studies indicate the mass transport of metal containing species through the bulk phases play an important role in the hydrogen sorption processes [99,100]. Though mass transport theories have been developed in detail for the $NaAlH_4$ system the effect of impurities are not examined [101,102], but will likely be present at some level in any applied system. Interestingly, oxygen contaminants have been linked [103] to the discovery of a new mobile aluminum containing species in $NaAlH_4$ [104] and shown to increase the mobility of hydrogen in NaH [105], a decomposition product of $NaAlH_4$. In the study of the latter, density functional theory (DFT) calculations suggested significant solubility of OH^- in the NaH lattice is allowed and is associated with a solid-solid phase transition [105]. In this regard, a NaH/NaOH solid solution phase that facilitates the mass transport and faster diffusion of Na may be important in the reversibility of $NaAlH_4$. Understanding the solid solubility of the NaH/NaOH system could provide an explanation of the function oxygen impurities play in hydrogen sorption processes. NaH as a component of the $NaAlH_4$ system is not only relevant in current hydrogen storage work, but also provides a simple test case for this study.

Solid solubility of the $NaH_{1-x}(OH)_x$ system was investigated via in situ PXRD for a range of compositions ($0.3 \leq x \leq 1.0$) as part of a combined computational/experimental study (full article available in Appendix A) [106]. The results are compared with the solid solubility reported in earlier work by Mikheeva et al. [107] that focused on the hydroxide rich side of the NaH/NaOH system. Their work demonstrated restricted regions of solid solution formation in the NaH/ NaOH system [107]. The authors determined there exists two regions of solid solution phases: the α phase solid solution consisting of H^- substitution on OH^- sites in orthorhombic (B*mm*b) NaOH and the β phase solid solution consisting of H^- substitution on OH^- sites in fcc NaOH [107]. The phase diagram shows the region of the α phase solution forms up to 27 and 32 mol % NaH at room temperature and 200 °C, respectively [107]. The region of the β phase solution is shown to exist up to 36 and 75 mol % NaH at 240 and 450 °C respectively [107]. Between the α and β regions there is a very small region that contains both α and β phase solid solutions [107]. Outside these regions mixtures of α + NaH and β + NaH are present where the dividing line is at roughly 225 °C [107]. There is no solubility shown for NaOH on the NaH-rich side of the phase diagram in the Mikheeva work [107].

5.1. EXPERIMENTAL

NaH (95%) was purchased from Sigma-Aldrich and used as received. NaOH (97%) was purchased from Fisher Chemical and was dried at 300 °C under dynamic vacuum for 12 hours in order to remove any remaining water. No hydrates were visible in X-ray diffraction or nuclear magnetic resonance measurements after drying [105]. All samples were prepared and handled in an Ar atmosphere glove box with oxygen and H_2O levels below 1ppm. All NaH/NaOH samples were hand mixed with mortar and pestle in the glove box for approximately 5 minutes prior to calorimetry or X-ray diffraction measurements. All mixtures are given in molar percent.

The in-situ powder X-ray diffraction (PXRD) was performed on a Rigaku Ultima IV diffractometer using the standard Bragg-Brentano scattering geometry and Cu-K_α radiation. The NaH/NaOH samples were placed in a rectangular aluminum sample holder and sealed with thin adhesive Kapton tape during preparation in the glovebox. The

Kapton tape provides an airtight seal up to about 300°C. Powder samples were compacted in the sample holder for better thermal transfer than a loose powder would provide. The aluminum XRD sample holder was heated with a Dale 20 W power resistor fastened to the bottom surface. The sample temperature was maintained using an Omega Autotune controller, and the holder temperature was measured with type-K thermocouples. The samples were heated from room temperature up to 260 °C, and the XRD spectra were recorded in roughly 30-50 °C temperature intervals from 22 to 260 °C and again on cooling. For a few of the compositions, the samples were heated a second time to a temperature of 325 °C and cooled. XRD spectra were recorded at 325 °C and again at room temperature. A range from 30° to 70° of 2θ was used for all scans. The step size was 0.02° 2θ, with a scanning speed of 1.5°/min.

5.2. RESULTS AND DISCUSSION

In situ X-ray diffraction was performed on multiple NaH/ NaOH samples of differing compositions to experimentally investigate the mixing process in the NaH/NaOH system. Figure 5.1 shows the heating and cooling process of a 40 mol % NaH + 60 mol % NaOH sample heated up to 260 °C. At 260 °C the sample is almost completely mixed into a single fcc phase solid solution. As the sample cools, the fcc phase solid solution is still present at 180 °C (but shifted to higher angle), but some of the solid solution has now phase separated into B*mm*b phase NaOH and NaH. As the sample reaches room temperature, NaH and NaOH are mostly phase separated. At 315 °C (top panel in Figure 5.1) the sample *completely mixed* into an fcc structure solid solution. Similar results were obtained for compositions of 90, 70, 50, and 25 mol % NaH, respectively. These results suggest necessary modifications to the phase diagram as presented in Mikheeva's work. The region of fcc β solid solutions should be extended to higher NaH concentrations at temperatures of >260 °C to accommodate hydride rich compositions that continue to form solid solutions. Further, the region where α and β solid solutions exist simultaneously shown in Mikheeva's phase diagram should possibly be extended to include higher NaH concentrations, as the X-ray diffraction data clearly show the existence of the two phases for concentrations outside the allowed region in

Mikheeva's diagram. However, sluggish kinetics at lower temperature may be responsible for incomplete phase separation.

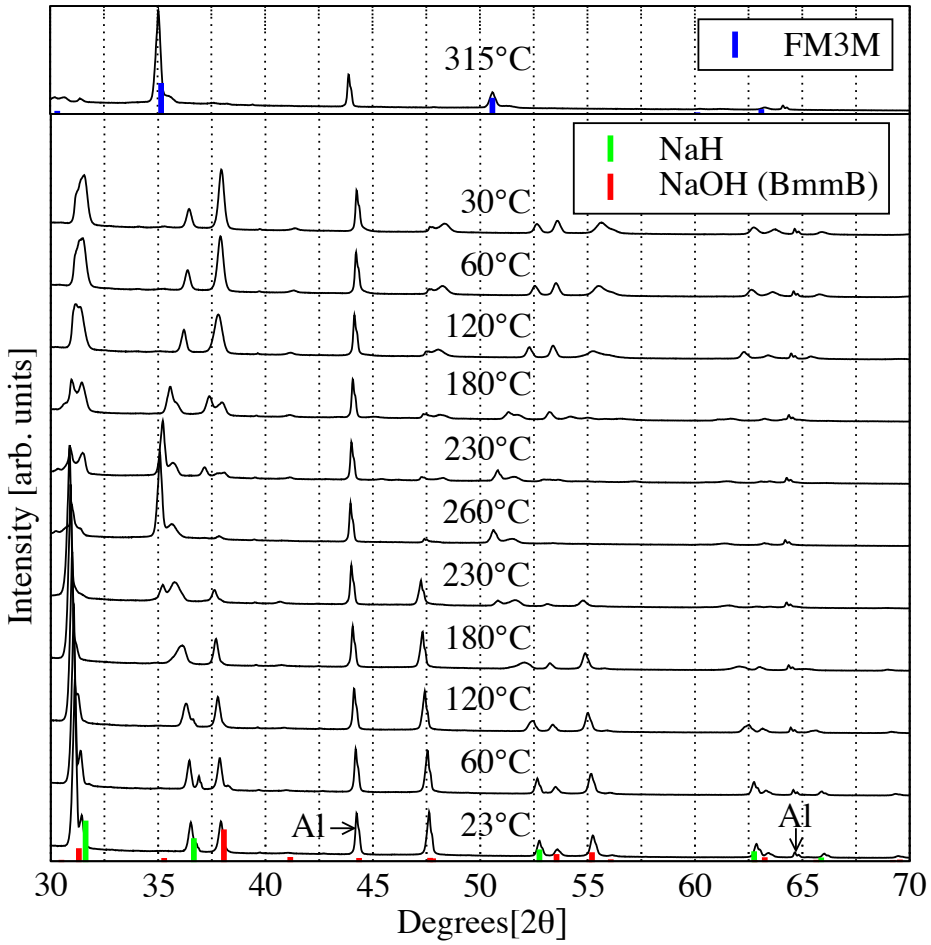

Figure 5.1. In situ X-ray diffraction data of the heating and cooling process for 40 mol % NaH + 60 mol % NaOH sample. The first scan is indicated at 23 °C, and the last scan is indicated at 30 °C. Vertical guidelines (dotted lines) are given to emphasize the peak shifts. The marked Al peaks were generated by the aluminum sample holder.

The NaH lattice parameters were extracted from the in situ X-ray diffraction data by implementing full pattern Rietveld refinement from the general structure analysis

system (GSAS) [108,109]. The NaH lattice expansion and unit cell volume expansion of NaH in the 40 mol % NaH + 60 mol % NaOH sample are compared to that of pure NaH in Figure 5.2. The comparison shows that NaH in the 40 mol % NaH + 60 mol % NaOH

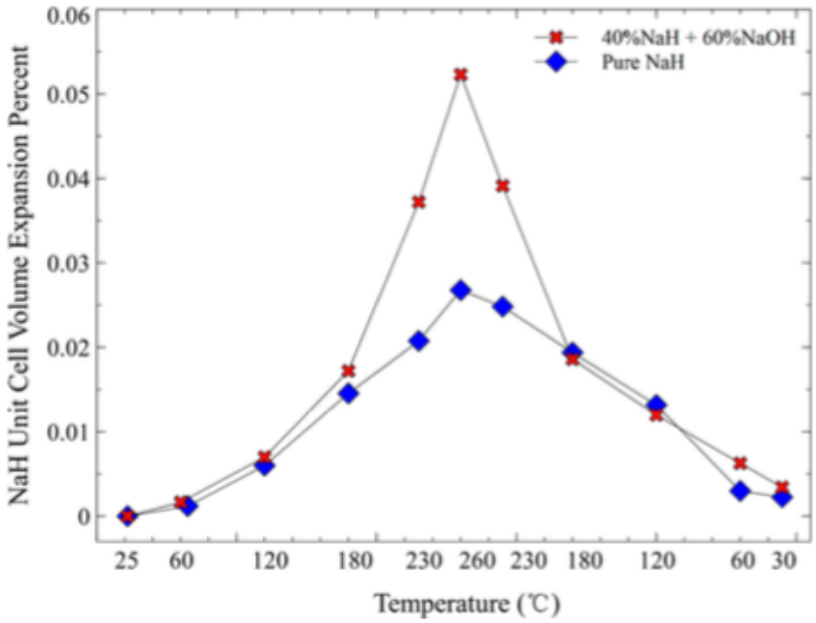

Figure 5.2. Cell volumes via XRD for pure NaH and a 40 mol % NaH + 60 mol % NaOH mixture as a function of temperature during a heating and cooling cycle between 25 and 260 °C.

sample has a much larger lattice expansion than pure NaH when heated using the same process. Also, the lattice expansion is not linear. The two-point coefficients of linear expansion, calculated using room temperature and the highest temperature point, for pure NaH and NaH in the 40 mol % NaH + 60 mol % NaOH sample are 37×10^{-6}/°C and 72×10^{-6}/°C, respectively. The massive volume expansion of the NaH in the 40 mol % NaH + 60 mol % NaOH sample is evidently due to the formation of solid solution on heating.

5.3. STUDY CONCLUSIONS

In this work the solid solubility of the NaH/NaOH system was investigated over a range of compositions. The findings indicate necessary modifications of the NaH/NaOH phase diagram to allow for the existence of fcc β phase solid solutions in the NaH rich region at temperatures above 260 °C. When solid solution formation occurs in the NaH/NaOH system, the phase transitions in NaOH are concomitant with mixing and the high temperature structure is single phase fcc before melting. This combination of phase transitions and mixing is fully reversible on cooling. Phase transition to the single phase fcc structure is accompanied by a large volume increase of the NaH unit cell, likely from NaOH entering the NaH lattice. Upon cooling NaH and NaOH begin to phase separate, though due to sluggish kinetics at low temperature the process is not complete.

6. CONCLUSIONS

In the work presented, the surface functionalization of nanoporous carbon scaffolds with nitrogen heteroatoms was explored as a way to alter the hydrogenation properties of metal hydrides confined in the scaffold with relation to the modifications achieved from nanoconfinement in a base non-functionalized carbon scaffold with similar physical properties. Carbon scaffolds with two distinct pore structures from reported literature methods were used in the study [67,68,71,73,74]. Namely, (1) nitrogen-functionalized/non-functionalized NPC-type carbon with cylindrical nanopores arranged in a 2D hexagonal geometry, produced from a soft-templated processes [67,68]. (2) Nitrogen functionalized/non-functionalized CMK-3 type carbon with slit-like pores nanocast from SBA-15 hard silica templates [71,73,74]. Nitrogen sorption measurements indicated the synthesized carbon scaffolds possess ordered mesostructures with high surface areas and pore volumes consistent with reported literature values. X-ray photoelectron spectroscopy studies revealed nitrogen in the carbon scaffold was present in four different bonding environments identified as pyridinic, pyrollic, graphitic, and oxidized nitrogen. In both the NNPC and NCMK-3 scaffolds pyridinic and pyrollic nitrogen dominated the spectra, combined accounting for >66% and >87% of the nitrogen detected for NNPC and NCMK-3 respectively across all the different scaffolds measured in this work.

Together with XPS, TPD and hydrogen desorption kinetics measurements of confined $LiBH_4$ demonstrated functionalizing the surface of the carbon scaffolds with nitrogen can stabilize the release of diborane and kinetically stabilize the decomposition of $LiBH_4$ to higher temperatures. In particular, the results demonstrate nitrogen heteroatoms on the surface of the carbon scaffold strongly influence the interface with infiltrated $LiBH_4$, increasing the activation energy for hydrogen desorption by 30 kJ/mol and increasing the diborane release temperature by ~30 °C. XPS data shows that a large fraction of the nitrogen is pyridinic, strongly suggesting that the lone pair of electrons is able to effectively solvate BH_3 groups on a surface layer. QENS studies of the confined $LiBH_4$ systems support the concept that nitrogen present on the scaffold surface may

influence the interfacial hydride layer, where an Arrhenius analysis indicated higher $[BH_4]^-$ reorientational activation energies for $LiBH_4$ confined in the nitrogen-functionalized scaffolds.

An isothermal Arrhenius analysis of confined $NaAlH_4$ yielded measured hydrogen desorption activation energies of 20 kJ/mol or more lower for $NaAlH_4$ in the nitrogen-functionalized scaffold, suggesting the presence of nitrogen has a significant influence on the desorption process. Hydrogen cycling measurements indicate that hydrogen can be reversibly stored within all the scaffolds examined, with a reversible storage capacity up to 3 wt% H_2 after 3 cycles. During the hydrogen desorption process, the majority of hydrogen is not released until higher temperatures for $NaAlH_4$ confined in nitrogen-functionalized scaffolds, despite the significantly lower measured activation energies. This indicates the existence of a rate-limiting step for desorption that may be linked to the level of nitrogen doping in the scaffolds and the onset of $NaAlH_4$ melting.

In situ x-ray diffraction studies of the solid solubility in the NaH/NaOH system determined phase transitions in NaOH are concomitant with mixing and the high temperature structure is single phase fcc before melting. This combination of phase transitions and mixing is fully reversible on cooling. Phase transition to the single phase fcc structure is accompanied by a large volume increase of the NaH unit cell, likely from NaOH entering the NaH lattice. The findings demonstrate oxygen impurities leading to the presence of OH^- units can induce changes to the hydrogen sorption properties of metal hydride systems containing NaH (ex. $NaAlH_4$).

In all, this work indicates surface functionalized nanoporous carbon scaffolds provide a method of altering the hydrogen sorption properties of confined metal hydrides in addition to the modification obtained from nanoconfinement alone in a non-functionalized scaffold. Here nitrogen-functionalization of carbon scaffolds was investigated for this purpose, but the method can easily be modified to include other heteroatoms, allowing the electronic nature of the scaffold to be tuned for the desired application.

APPENDIX A.

FULL PUBLISHED PAPER CONTAINING STUDY IN SECTION 5

DENSITY FUNCTIONAL THEORY OF MH-MOH SOLID SOLUBILITY (M = ALKALI) AND EXPERIMENTS IN NaH-NaOH

Gang Wang,[†] C. L. Carr,[†] Dongxue Zhao,[†] E. G. Sorte,[‡] Tim Ellis-Caleo,[‡] M. S. Conradi,[‡] R. C. Bowman, Jr.,[§] and E. H. Majzoub[*,†]

[†]Center for Nanoscience, and Department of Physics and Astronomy, University of Missouri-St. Louis, St. Louis, Missouri 63121, United States

[‡]Department of Physics, Washington University in St. Louis, St. Louis, Missouri 63130, United States

[§]RCB Hydrides, LLC, 117 Miami Avenue, Franklin, Ohio 45005, United States

First published in the *Journal of Physical Chemistry C* (March 2015)

ABSTRACT

We present first-principles solubility calculations of H^-/$[OH]^-$ mixing in binary alkali metal hydrides MH and their corresponding hydroxides MOH, for M ={Li, Na, K, Rb, Cs}. Solid solubility in the MH−MOH system may play an important role in solid-phase reactions involving the MH system, including for example many aluminum-based complex hydrides of the alkali metals, such as $NaAlH_4$ and $LiAlH_4$. Our results indicate that the available cell volume for H^- and OH^- groups correlates strongly with mixing, and MOH is soluble in MH for M ={Na, K, and Rb} where available volumes for H^- and OH^- anions differ by less than about 15%, very similar to a Hume−Rothery type rule for intermetallics. The predicted mixing temperatures for the K and Rb systems are lower than for the Na system, in part because of the similarity in MH and MOH primitive cell volumes. Critical temperature diagrams for the formation of solid solution MH−MOH mixtures as a function of MOH concentration are calculated using a free energy minimization in the grand canonical ensemble. Differential scanning calorimetry and in situ X-ray diffraction measurements of the $NaH_{1-x}(OH)_x$ system are presented for a range

of compositions ($0.3 \leq x \leq 1.0$). As the temperature is raised, the polymorphic phase transitions present in NaOH occur concomitantly with H^-/OH^- mixing, eventually forming a single-phase cubic structure; the behavior is fully reversible on cooling. Finally, the formation of solid solution MH/MOH reduces the decomposition temperature of $NaH_{1-x}(OH)_x$ to lower temperatures than pure NaH while increasing the stability in the KH and RbH systems.

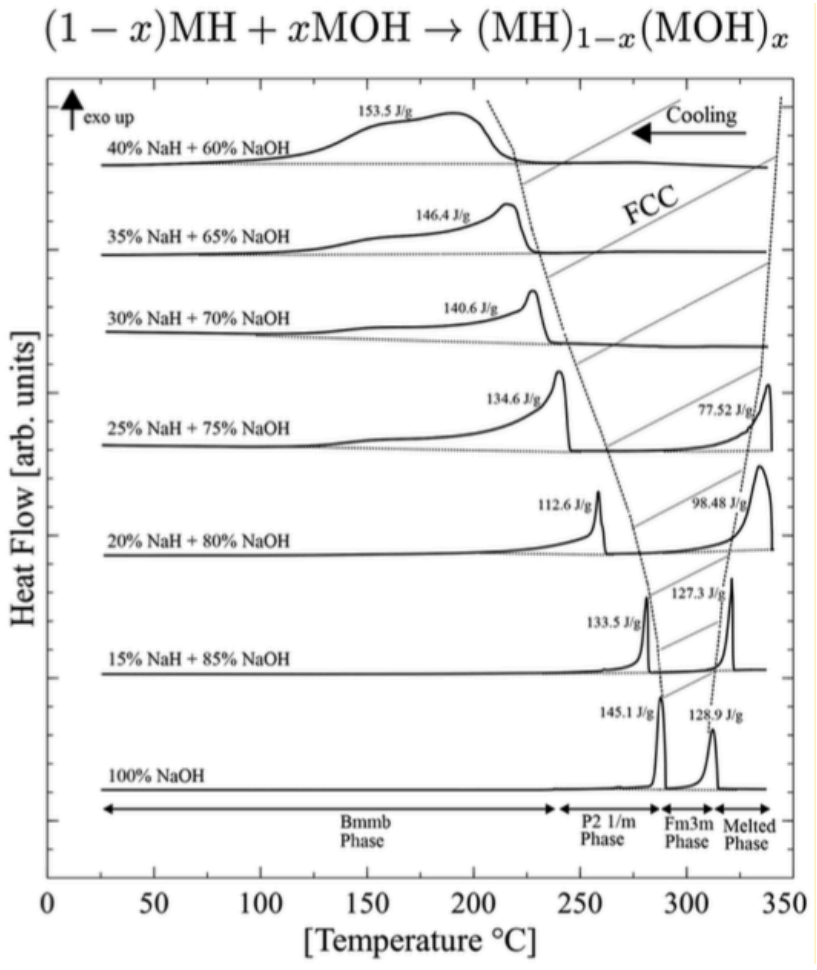

Table of Contents Image from Published Paper

INTRODUCTION

Diffusion of hydrogen and the rapid mass transport of metal species are important for many complex anionic hydrogen storage materials. In particular, sodium aluminum hydride ($NaAlH_4$) decomposes in two steps, resulting in phase separated Na_3AlH_6 + Al, and NaH + Al, respectively. This system reversibly absorbs hydrogen with the addition of a few mol % of transition metal dopant [1]. While extensive theories of mass transport have been developed [2,3], they do not consider the effect of impurities such as oxygen/hydroxide that are unavoidable in practical applications. The family of alkali metal alanates that are of interest in the hydrogen storage community also includes $LiAlH_4$, because of its large reversible hydrogen wt %, and $KAlH_4$, which is evidently reversible without the need for a catalyst [4]. Alanate reversibility could be influenced by residual oxygen contamination via faster diffusion and mass transport of M in an MH/MOH solid solution phase. Our results indicate that the similarity in cell volume available to H^- and OH^- anions in the MH and MOH lattices, respectively, strongly influences the onset of mixing and may provide a partial explanation of this behavior.

The objective of this work is to more fully understand the solid solution formation in alkali metals and alkali metal hydroxides that may be relevant for solid state reactions, including but not limited to metal hydrides. In previous work, we investigated mixing in the NaH/NaOH system, with a focus on the NaH-rich side of the pseudobinary NaH/NaOH phase diagram [5] and demonstrated that thermal activation alone was unable to account for ^{1}H NMR line narrowing with increasing temperature in a 10 mol % NaOH sample. Further, differential scanning calorimetry was indicative of a phase transition. This paper presents a comprehensive density functional theory (DFT) investigation of the enthalpy of mixing of MOH in MH where M ={Li, Na, K, Rb, and Cs}. We present these results via the calculation of critical temperatures for the onset of mixing of MH and MOH, *at fixed MH/MOH ratios*, i.e., we calculate the onset of mixing for the reaction $(1 - x)\mathrm{MH} + x\mathrm{MOH} \rightarrow \mathrm{MH}_{1-x}(\mathrm{OH})_x$. We make no attempt to calculate the full pseudobinary phase diagram because of the difficulty introduced by the many soft modes that appear in structures containing OH^- groups, where the potential energy surface for OH^- rotations is relatively flat. Because we calculate the enthalpy of mixing at fixed concentration and

ignore partially segregated possibilities, e.g., yMH + $MH_{1-z}(OH)_z$, our critical temperatures represent *lower bounds* for the onset of mixing.

In this work, we also present an experimental study of the NaH/NaOH pseudobinary phase diagram over a limited composition range and compare our findings with predictions obtained from the computational study and previous work. In the early studies by Mikheeva et al. [6], the hydroxide-rich sides of the pseudobinary NaH/NaOH and KH/KOH phase diagrams were experimentally investigated. Their work demonstrated restricted regions of solid solution formation in the NaH/ NaOH system. The authors determined there exists two regions of solid solution phases: the α phase solid solution consisting of H^- substitution on OH^- sites in orthorhombic (B*mm*b) NaOH and the β phase solid solution consisting of H^- substitution on OH^- sites in fcc NaOH. The phase diagram shows the region of the α phase solution forms up to 27 and 32 mol % NaH at room temperature and 200 °C, respectively. The region of the β phase solution is shown to exist up to 36 and 75 mol % NaH at 240 and 450 °C respectively. Between the α and β regions there is a very small region that contains both α and β phase solid solutions. Outside these regions mixtures of α + NaH and β + NaH are present where the dividing line is at roughly 225 °C. There is no solubility shown for NaOH on the NaH-rich side of the phase diagram in the Mikheeva work [6].

Because of its importance in hydrogen storage reactions, we study extensively the hydride-rich side of the phase diagrams, where our computational work shows that a solid solution *can form* for sample compositions containing less than 41 and 50 mol % hydroxide in the NaH/NaOH and KH/KOH systems, respectively. The extreme reactivity of KOH prevented us from collecting experimental data for this system, and we focused experimentally on the study of the NaH/NaOH system.

The manuscript is organized as follows. In the second section we introduce our computational methods and construction of the solid-solution supercells used in our DFT calculations. In the third section we discuss our experimental methods. The fourth section presents the main results obtained in this work.

COMPUTATIONAL METHODS

All density functional theory (DFT) calculations were performed using the Vienna ab initio simulation package (VASP) [7,8]. Standard projector augmented wave (PAW) pseudopotentials were used along with the PW91 [9,10] generalized gradient approximation (GGA) for the exchange correlation. The cutoff energy was 600 eV for all calculations with an electronic convergence criterion of 10^{-6} eV. Atomic coordinate and cell parameter relaxations were completed until the forces on the ions were less than 0.005 eV/Å. Frozen phonon calculations were performed in the harmonic approximation using the linear response capability in VASP 5, and the phonon frequencies were used to calculate finite temperature free energies.

Gas-phase energy of hydrogen was calculated by placing one H_2 molecule in a 20×20×20 $Å^3$ cell, using only the Γ point (k = 0). Cubic F$m\bar{3}m$ 2×2×2 supercells of MH, M={Li, Na, K, Rb, and Cs} were chosen to simulate the hydrides. Monkhorst−Pack grids were used for Brillouin zone integration [11]. Supercell sizes and the space groups of the crystal structures are listed in Table S1 (Supporting Information). K-point meshes are listed in Table S2. To improve the physical accuracy of the calculations, successively larger supercells were chosen to reproduce the experimentally measured entropies.

MH and MOH Crystal Structures and Construction of Supercells. Our DFT calculations of the solubility focused on the MH-rich side of the phase diagram; therefore, supercells of mixed MH/MOH were constructed by starting from a 2×2×2 supercell of cubic MH and substituting oxygen atoms in one of six octahedral positions around the hydrogen atoms, along the coordinate axes, to obtain a composition of $[MH_{1-x}(OH)_x]$. The initial O−H bond length was placed at 0.88 Å. The oxygen atom positions were randomized using a simulated annealing algorithm (SA) [12]. The energy functional (cost function) used was the total electrostatic energy:

$$E = \sum_{i \neq j} \frac{e_i e_j}{r_{ij}} \quad (1)$$

where e_i and e_j are the reference charges of elements *i* and *j*. The idealized reference charges for M, H, and O were +1, +1, and −2, respectively, and r_{ij} is the distance between the elements *i* and *j*. For the purposes of this SA application, it is not important that the assigned atomic charges be correct. All randomized solid-solution structures were fully relaxed using the conjugate gradient algorithm in VASP. By use of periodic boundary conditions in the SA simulations, the Coulomb interaction was calculated within a radius of one unit cell dimension centered on every atom. Standard SA protocol compares the reference energies of an existing configuration (E_1) and a new configuration (E_2). All downhill moves are accepted, and uphill moves are accepted with a Boltzmann probability of $e^{-(E_2-E_1)/T}$ if $E_2 > E_1$, where T represents the annealing reference temperature [12]. We used an exponential annealing schedule with $T_n = T_i e^{-[(1/N)\ln(T_i/T_f)]n}$ where $T_i = 100$ was the initial temperature parameter and $T_f = 1\times10^{-3}$ was the final parameter. We used $N = 30$ temperature steps, where *n* refers to the *n*th step.

Solid-Solubility Calculations. The solubility of MOH in MH where M ={Li, Na, K, Rb, and Cs} can be studied by investigating the reaction:

$$(1\text{-}x)\text{MH} + x\text{MOH} \rightarrow \text{MH}_{(1\text{-}x)}(\text{OH})_x \tag{2}$$

where $0 < x < 1$. The compound $\text{MH}_{(1\text{-}x)}(\text{OH})_x$ is favorable when the free energy, F, of the compound is less than the sum of the free energies of MOH and MH:

$$\Delta F = F[\text{MH}_{(1\text{-}x)}(\text{OH})_x] - xF(\text{MOH}) - (1\text{-}x)F(\text{MH}) < 0 \tag{3}$$

The standard expression for the Helmholtz free energy of a solid as a function of temperature is given by:

$$F = U_0 + \sum_r \left[\frac{1}{2}\hbar\omega_r + k_B T \ln(1 - e^{-\hbar\omega_r/(k_B T)})\right] - TS_{conf} \tag{4}$$

where U_0 is the electronic total energy of a crystal from the geometric optimization using DFT, k_B is Boltzmann's constant, ω_r values are the (harmonic) phonon frequencies derived via the linear response method in VASP, and $\sum_r (½)\, \hbar\omega_r$ is the zero point energy (ZPE) representing the atomic vibrations at absolute zero. S_{conf} denotes the configurational entropy. Random occupancy of a binary mixture was evaluated using the standard expression:

$$S_{conf} = -Nk_B[x \ln(x) + (1-x) \ln(1-x)] \quad (5)$$

with $x = [OH^-]$ and $1\text{-}x = [H^-]$, and N is the number of formula units.

In the solid solubility calculations, the critical soluble temperature (T_c) is obtained when $\Delta F(T_c, x) = 0$. As discussed above, we calculate T_c for the case of phase segregation into pure MH + MOH only. The enthalpy change at the critical temperature can be calculated from dF = dH – TdS = 0:

$$\Delta H = T[S(T,MH_{(1-x)}(OH)_x) - xS(T, MOH) - (1-x)S(T,MH)] \quad (6)$$

The formation of the solid solution is endothermic when $\Delta H > 0$.

We also include in our calculations the decomposition of the MH/MOH mixtures that results in the release of hydrogen gas. In these calculations, the Gibbs' free energy minimizations were performed using the grand canonical linear programming method (GCLP) [l3], assuming a H_2 reservoir, to account for decomposition and hydrogen release at P = 1 bar H_2. The chemical potential of H_2 can be evaluated with the following expression.

$$\mu = U_0 + F_v(T) + F(T,p) \quad (7)$$

Here U_0 is the electronic energy of a hydrogen molecule evaluated by the first-principles calculations of a hydrogen molecule in a large volume-conserved cell. $F_v(T)$ is the vibrational free energy. F(T,p) contains the translational and rotational motions, along

with the interactions between hydrogen molecules. The last term was taken from the experimental entropy of hydrogen under standard conditions [l4].

EXPERIMENTAL METHODS

NaH (95 wt %) was purchased from Sigma-Aldrich and used as received. NaOH (97 wt %) was purchased from Fisher Chemical and was dried at 300 °C under dynamic vacuum for 12 h in order to remove any remaining water. No hydrates were visible in X-ray diffraction or nuclear magnetic resonance measurements after drying [5]. All samples were prepared and handled in an Ar atmosphere glove box with oxygen and H_2O levels below 1ppm. All NaH/NaOH samples were hand mixed with mortar and pestle in our glove box for approximately 5 min prior to calorimetry or X-ray diffraction measurements. All mixtures are given in molar percent.

Differential scanning calorimetry (DSC) was performed on a TA Instruments Q2000 series analyzer. About 6 mg of sample was loaded in an aluminum pan with a hermetically sealed lid in an Ar glove box. The sample was heated from 25 °C to a maximum of 340 °C and then cooled to 25 °C at a rate of 5 °C /min using flowing nitrogen gas.

The in situ powder X-ray diffraction (XRD) was performed on a Rigaku Ultima IV diffractometer using the standard Bragg-Brentano scattering geometry and Cu K_α radiation. The NaH/NaOH samples were placed in a rectangular aluminum sample holder and sealed with thin adhesive Kapton tape during preparation in the glovebox. The Kapton tape provides an airtight seal up to about 300 °C. Powder samples were compacted in the sample holder for better thermal transfer than a loose powder would provide. The aluminum XRD sample holder was heated with a Dale 20 W power resistor fastened to the bottom surface. The sample temperature was maintained using an Omega Autotune controller, and the holder temperature was measured with type-K thermocouples. The samples were heated from room temperature up to 260 °C, and the XRD spectra were recorded in roughly 30-50 °C temperature intervals from 22 to 260 °C and again on cooling. For a few of the compositions, the samples were heated a second time to a temperature of 325 °C and cooled. XRD spectra were recorded at 325 °C and

again at room temperature. A range from 30° to 70° of 2θ was used for all scans. The step size was 0.02° 2θ, with a scanning speed of 1.5°/min.

Attempts were made to investigate the KH/KOH system, but strong reactivity of these samples with our Kapton tape and aluminum sample holders for XRD and DSC prevented the collection of reliable data. Further, it is generally observed that as one goes down the alkali metal group, the more reactive is the metal. Given the high reactivity of our KH/KOH samples with our sample holder materials, we did not attempt experiments with RbH/RbOH.

RESULTS AND DISCUSSION

Not surprisingly, crystal structures of the alkali hydrides and their hydroxides share many features. The structures of MH for M ={Li, Na, K, Rb, and Cs} all have the $Fm\bar{3}m$ space group [15]. The known structures of the hydroxides tend toward this cubic symmetry at high temperature presumably because of rapid rotation of the OH^- units except for LiOH that remains in *P*4/*nmm* up to 473 °C [16]. NaOH exhibits polymorphism starting with the low temperature structure in $Bmmb$ until 241 °C. Between 241 and 295 °C, NaOH has the spacegroup $P2_1/m$, and the structure above 295 °C is $Fm\bar{3}m$ [16]. The low temperature structure of KOH is $P2_1/m$ until 244 °C at which point it transforms to $Fm\bar{3}m$ [16]. The low temperature structure of RbOH is $Cmc2_1$ until −8 °C and is $P2_1/m$ from −8 to 235 °C. Above 235 °C, it is $Fm\bar{3}m$ [16]. The structure of CsOH at temperatures below −39 °C is *Pmnb*, above which it becomes $Bmmb$, transforming to $Fm\bar{3}m$ above 225 °C [16].

For the purpose of calculating the free energies and critical temperatures of mixing, we use the fully relaxed, ground-state structures obtained at T = 0 K. As mentioned above, DFT relaxation of literature structures for the alkali metal hydroxides often results in symmetry breaking due to the presence of soft modes. In nature, anharmonic effects at finite temperature likely stabilize these modes; recall our calculations treat phonon modes in the harmonic approximation. For example, DFT relaxation of the LiOH supercell using the literature structure in symmetry P4/*nmm* will break this symmetry, resulting in a structure with no symmetry (P1). Phonon vibrational

frequencies calculated for supercells of the remaining hydroxides (NaOH, KOH, RbOH, and CsOH) all contained imaginary modes. The method of mode following [17] was used to attain stable structures for all hydroxides. The resulting space groups are listed in Table S1. The differences in the DFT-calculated total energies from these relaxations provide an estimated error of about ±80 °C for the calculated critical temperatures, T_c.

LiH/LiOH System. The LiH/LiOH system is uninteresting in that any mixture of LiH and LiOH is predicted via our GCLP calculations to decompose with the release of hydrogen gas before formation of a solid solution phase. The mixture of LiH and LiOH is predicted to release H_2 through the reaction

$$LiH + LiOH \rightarrow Li_2O + H_2 \quad (8)$$

with an enthalpy change of −18.28 kJ/mol H_2 at T = 0 K. Forbidding the reaction in eq 8, the enthalpy of mixing was calculated for the composition $Li_{32}H_{31}OH$, even though the composite crystal is evidently unfavorable against H_2 formation. The solid solution would form at 708 °C with an enthalpy of 219 J/g (1.86 kJ/mol reaction), well above the predicted critical temperature for eq 8. Numerous experimental studies are consistent with these findings in that only the LiH, LiOH, Li_2O, and $LiOH·H_2O$ have been observed for this system under various conditions [18−23].

NaH/NaOH System. The calculated cell volume of cubic NaH is 28.02 $Å^3$/f.u., and the cell volume of stable mode-followed B*mm*b NaOH (in space group C*mc*2_1) is 30.48 $Å^3$/f.u. Figure 1 shows the DFT-relaxed unit cell volume ratio of $MH_{(1-x)}(OH)_x$ to MH for $0 \leq x \leq 1$. The black circles represent $NaH_{(1-x)}(OH)_x$. The volume increases with the increase of NaOH concentration (x) from NaH to NaOH. This is expected as the crystal shifts from NaH-like to NaOH-like and is consistent with the larger cell volume of pure NaOH.

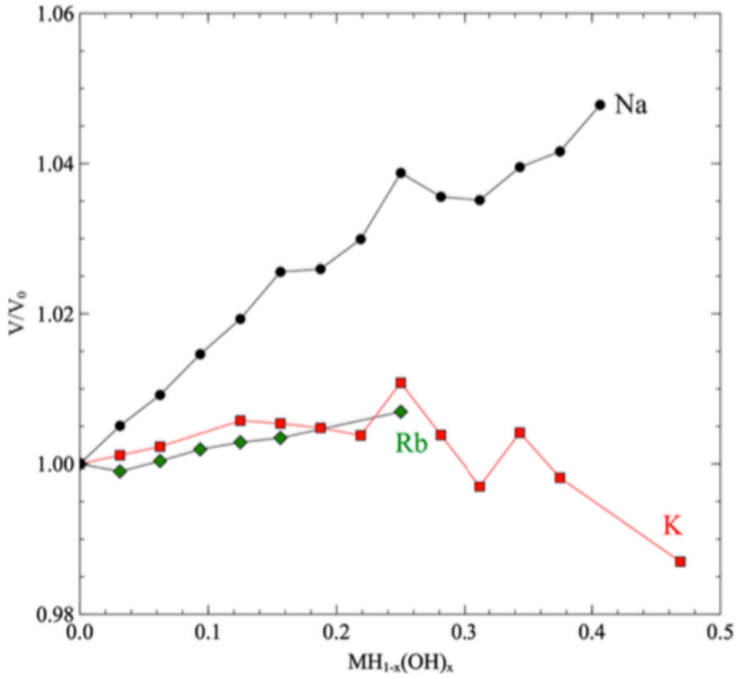

Figure 1. Relaxed crystal volume expansions as a function of MOH concentration; M = Na (black circle), K (red square), Rb (green diamond).

Figure 2 shows the hydride rich side of the calculated critical temperature diagram for the NaH/NaOH system, which was not explored in Mikheeva's work. Below the green curve is where NaOH and NaH are phase separated. The green curve represents the calculated critical temperatures above which the solid solution is favorable:

$$(1\text{-}x)\mathrm{NaH} + x\mathrm{NaOH} \rightarrow \mathrm{NaH}_{(1\text{-}x)}(\mathrm{OH})_x \qquad (9)$$

Table S3 shows the critical temperature and enthalpy for eq 9 for different NaH/NaOH ratios. The data indicate that formation of the solution is endothermic above the critical temperature and also show that the critical temperature increases with the increase of hydroxide concentration x. The solution is predicted to be stable until x =

0.41, above which the two-phase mixture *decomposes before mixing* according to the following reaction.

$$NaH + NaOH \rightarrow Na_2O + H_2 \quad (10)$$

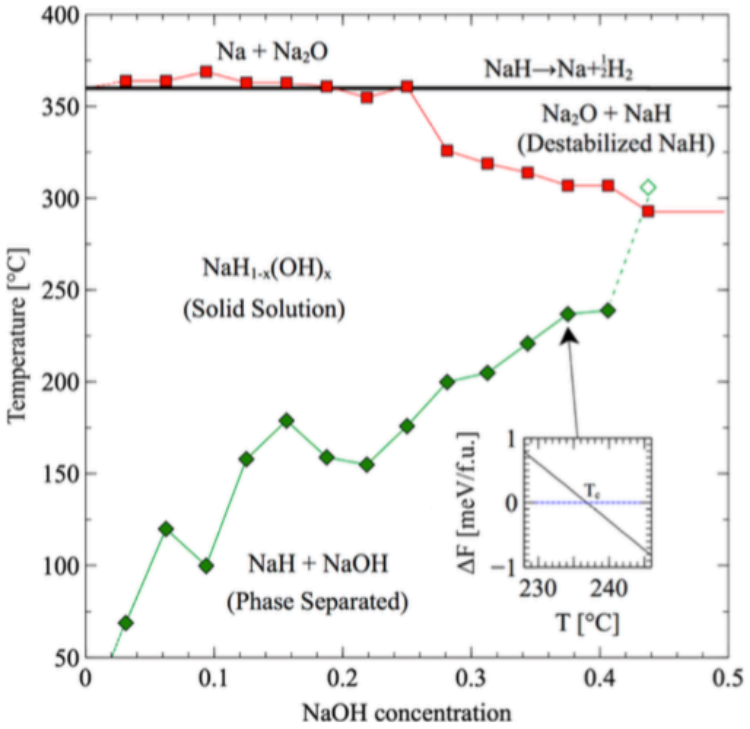

Figure 2. Critical temperatures for mixing and decompositions in the NaH/NaOH system: green, critical temperature; red, decomposition of solid solution; black, decomposition of NaH at P = 1 bar of H_2. Inset illustrates critical temperature.

This reaction is predicted to occur around 293 °C with an enthalpy of about 59 kJ/mol H_2 when $x > 0.41$. In Figure 2, the region between the green and red curves is where only the solid solution exists. The red curve represents the decomposition of the solid solution. At concentrations below about $x = 0.25$, the solid solution decomposes at essentially the same temperature as that of pure NaH, represented by the black line. At

concentrations larger than $x = 0.25$, the decomposition temperature of the solid solution decreases, forming a new region containing Na_2O and NaH. This region extends above the red curve up to the black line that represents the decomposition of pure NaH. Solid solution decomposition occurs as

$$NaH_{(1-x)}(OH)_x \rightarrow (1- 2x)NaH + xNa_2O + xH_2 \quad (11)$$

Reactions such as the mixing and decomposition shown in Figure 2 represent the free energy only and ignore kinetics. The free energy critical temperatures are a lower bound; if the reaction had no kinetic barrier, it would proceed as soon as thermodynamically feasible. In addition, the physical accuracy of DFT reaction enthalpies provides only rough estimates of the critical solution temperatures. As the decomposition curve (red in Figure 2) and the solid-solution/phase-segregation curve (green in Figure 2) approach each other at large OH^- concentrations, the actual physical behavior will be strongly influenced by the kinetic barriers. Our experiments show that the solid solution is evidently stable to higher temperatures at compositions $x > 0.44$ in contrast to our DFT calculations which show decomposition above $x = 0.44$, before formation of the solid solution.

Perhaps most interestingly, for concentrations above about $x = 0.25$, the solid solution has a lower temperature of decomposition and hydrogen desorption than does pure NaH as shown in Table S3. The DFT-calculated decomposition of pure NaH is around 360 °C with an enthalpy of 91 kJ/mol H_2:

$$2NaH \rightarrow 2Na + H_2 \quad (12)$$

NaOH-Rich Compositions. The NaOH-rich side of the critical temperature figure was investigated using an 8 formula unit cell in space group $P2_1/m$ for NaOH, for compositions $Na_8(OH)_7H$, $Na_8(OH)_6H_2$, and $Na_8(OH)_5H_3$. These cells were constructed by removing 1, 2, and 3 oxygen atoms from the $P2_1/m$ NaOH structure, since the mixing takes place at higher temperatures where NaOH is in the $P2_1/m$ space group. The mixed

structures were optimized keeping the $P2_1/m$ symmetry and cell volume fixed but allowing the atomic coordinates to relax. The results (not shown) indicate that our selected mixed compounds $Na_8(OH)_7H$ and $Na_8(OH)_6H_2$ are favorable at and above −246 and −31 °C, respectively, but find that $Na_8(OH)_5H_3$ is unfavorable. This means that NaOH and NaH prefer to phase-separate at low temperature at a NaH content between 25 and 38 mol %, in agreement with Mikheeva et al. [6]. The enthalpy changes calculated at the experimentally observed temperatures (see DSC data) were calculated as 81 J/g at 275 °C for $Na_8(OH)_7H$ (12.5 mol % NaH) which is considerably lower than our 15 mol % NaH experimental value of 133.5 J/g determined from DSC. This is due to the experimental value being a combination of the solution enthalpy and the phase transition of NaOH from $Fm\bar{3}m$ to $P2_1/m$. However, we find an enthalpy of 142 J/g at 230 °C for $Na_8(OH)_6H_2$ in excellent agreement with our present DSC experimental value of 134.6 J/g for 25 mol % NaH (see below).

KH/KOH System. The red squares in Figure 1 show the DFT-relaxed unit cell volume expansion for $KH_{(1-x)}(OH)_x$, $0 \leq x \leq 1$. The calculated volume of cubic KH is 45.97 $Å^3$/f.u., while the volume of our stable KOH structure is 42.59 $Å^3$/f.u. The calculated volume of KOH in the experimental structure, space group $P2_1/m$, is 47.10 $Å^3$/f.u., and the calculated volume of KOH in the experimental structure in space group $Fm\bar{3}m$ is 46.23 $Å^3$/f.u. The volumes are similar; however, the volume of the mode-followed stable KOH structure is 7.3% smaller than the volume of KH. The calculated cell volumes in the solid solution phase hold roughly steady for KOH concentrations up to about 25 mol % and then begin to decrease.

Mixing in the potassium system is more favorable than in the sodium system, as the predicted temperatures for solution formation and the magnitude of the endothermic enthalpy changes are lower, as shown in Figure 3. The green curve represents the calculated critical temperature of solution formation, with the reaction

$$(1\text{-}x)\mathrm{KH} + x\mathrm{KOH} \rightarrow \mathrm{KH}_{(1-x)}(\mathrm{OH})_x \qquad (13)$$

Table S4 contains the critical temperature of solution formation and their corresponding enthalpy changes as well as the decomposition temperature of the solid solution. Similar to the sodium system, the critical temperature increases as the concentration of KOH is increased. The calculated critical temperatures are quite low, ranging from below 0 °C up to 70 °C.

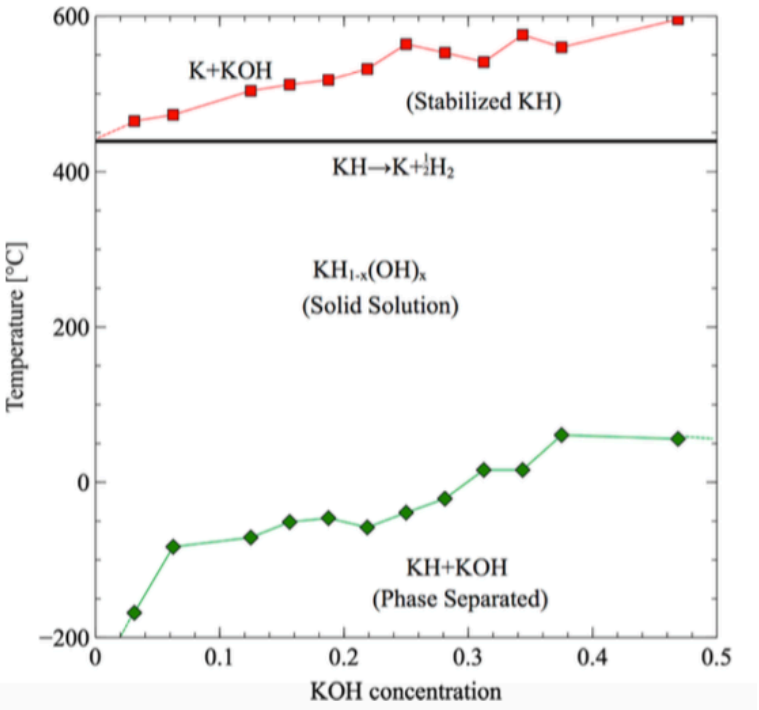

Figure 3. Critical temperatures for mixing and decompositions in the KH/KOH system: green, critical temperature; red, decomposition of solid solution; black, decomposition of KH at P = 1 bar of H_2.

However, because of a lack of kinetic barriers in our calculations, experimentally observed mixing may take place at higher temperatures.

The black line represents the DFT-calculated decomposition temperature for pure KH with an enthalpy of 91 kJ/mol H_2.

$$2KH \rightarrow 2K + H_2 \quad (14)$$

In contrast to the sodium system, upon mixing of KH/KOH, the solution is stable above the decomposition temperature of pure KH. The red curve is the predicted decomposition of the solution:

$$KH_{(1-x)}OH_{(x)} \rightarrow (1-x)K + xKOH + \frac{(1-x)}{2}H_2 \quad (15)$$

Evidently, KOH stabilizes KH in the entire range we investigated, and the stabilization is strengthened as the concentration of KOH increases.

RbH/RbOH System. The green diamonds in Figure 1 indicate the volume expansion of $RbH_{1-x}(OH)_x$ supercells as function of OH^- concentration (x). The volume increases with the increase of RbOH concentration. Figure 4 shows the critical temperatures for mixing in the RbH/RbOH system, which is similar to KH/KOH system. The decomposition temperature of the solution is higher than the pure hydride decomposition temperature of 339 °C. Therefore, similar to the potassium system, formation of the solid solution phase stabilizes RbH to higher temperature. Table S5 contains the solid solution critical temperatures and the corresponding enthalpies as well as the decomposition of the solid solution. The critical temperature and enthalpy of mixing are very low, indicating that the solution is even more favorable than in the Na and K systems.

CsH/CsOH System. The cesium system, like lithium, does not indicate the formation of a solid solution phase. CsH decomposes before the mixture can form a solution:

$$2CsH \rightarrow 2Cs + H_2 \quad (16)$$

The decomposition was predicted to occur at 423 °C, and it is an endothermic reaction, the enthalpy of which is 77 kJ/mol H_2.

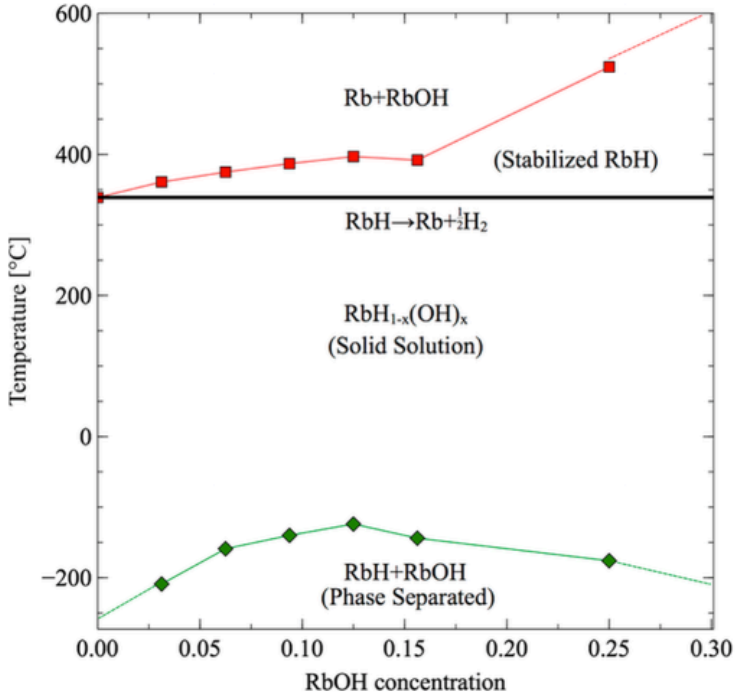

Figure 4. Critical temperatures for mixing and decompositions in the RbH/RbOH system: green, critical temperature; red, decomposition of solid solution; black, decomposition of RbH.

Cell Volumes in the MH/MOH System. Table 1 shows the available anion volumes and cation radii for the alkali monohydrides or hydroxides. All the structures of hydrides are $Fm\bar{3}m$, and the structures of MOH (V_{cal}) are taken from the mode-followed structures of B*mm*b MOH, which are *P*1 for LiOH, KOH, and CsOH, C*m*C2_1 for NaOH, and *Pc* for RbOH. The available anionic volumes were derived as $V_{cal} = V_{unitcell} - V_{cation}$, from our calculated volumes of the crystal minus the corresponding cation volume. Only a small portion of the resulting volume is physically available to the anion. However, it

provides a reliable metric for the ability of the MH and MOH to form a solid solution phase. The table illustrates that the soluble systems (Na, K, and Rb) have similar H^- and OH^- available anionic volumes, while the insoluble systems (Li and Cs) have large differences in their respective available anionic volumes (see column ΔV_{cal}). These findings are somewhat analogous to the Hume−Rothery rules where valence and relative size determine metal−metal solid solution mixing tendencies.

DSC and in Situ XRD Results for the NaH/NaOH System. Differential scanning calorimetry (DSC) and in situ X-ray diffraction were used to investigate mixing in the NaH/NaOH system. Figure 5 shows DSC scans over a range of molar ratios of NaH/NaOH. These samples were first heated up to 340 °C, and the DSC data were collected during the cooling process. In agreement with Mikheeva's phase diagram, the melting point of the mixture moves to higher temperature with increasing NaH content.

Table 1. Available Anion Volumes for H^- and OH^- Determined from Standard Cation Radii in MH and MOH Systems[a]

metal	r[cation] (Å)	$V_{cal}[H^-]$ (Å^3)	$V_{cal}[OH^-]$ (Å^3)	ΔV_{cal} (%)
Li	0.68	14.79	27.14	83.50
Na	0.98	24.19	26.66	10.21
K	1.33	36.12	32.74	-9.36
Rb	1.48	35.92	35.53	-1.09
Cs	1.67	46.75	38.66	-17.30

[a]Cation radii were taken from Kittel [24]. V_{cal} is the calculated volume for the anions and is described in the text.

At the same time, the two phase transitions of NaOH move to lower temperature and merge together with the NaH/NaOH phase-separation process. For the 40 mol % NaH + 60 mol % NaOH composition, this process takes place over a wide temperature range from 240 to 60 °C. Calculated enthalpies on the NaOH-rich side of the phase diagram are

in agreement with the DSC data as we indicated in the paragraph above on NaOH-rich compositions.

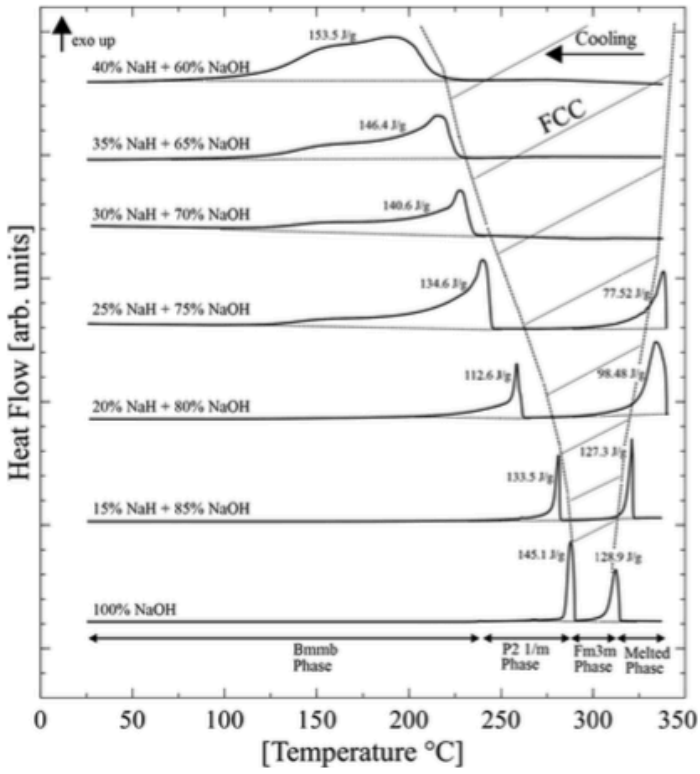

Figure 5. Differential scanning calorimetry (DSC) data of cooling scans. The horizontal dotted lines are guides for the eyes, serving as baselines. The hatched region indicates the approximate boundary of the cubic phase solid solution.

To investigate the dissolution and phase separation process, DSC was performed on a 70 mol % NaH + 30 mol % NaOH sample. The sample was first heated up to 330 °C in order to premelt the mixture. The data were recorded during sample heating up from 25 to 300 °C and then again upon cooling down to 25 °C at a ramp rate of 5 °C/min for

multiple cycles. During the heating and cooling cycles, substantial, repeatable thermal activity occurred around 170 °C as presented in Figure 6. The heating (bottom) curves show an endothermic peak, and the cooling (top) curves show an exothermic peak, which would be as expected for a reversible phase transition. The enthalpy of the reaction was calculated by integrating under the endothermic or exothermic peaks and was roughly 70 J/g at this composition.

In situ X-ray diffraction was performed on multiple NaH/NaOH samples of differing compositions to experimentally investigate the mixing process in the NaH/NaOH system. Figure 7 shows the heating and cooling process of a 40 mol % NaH

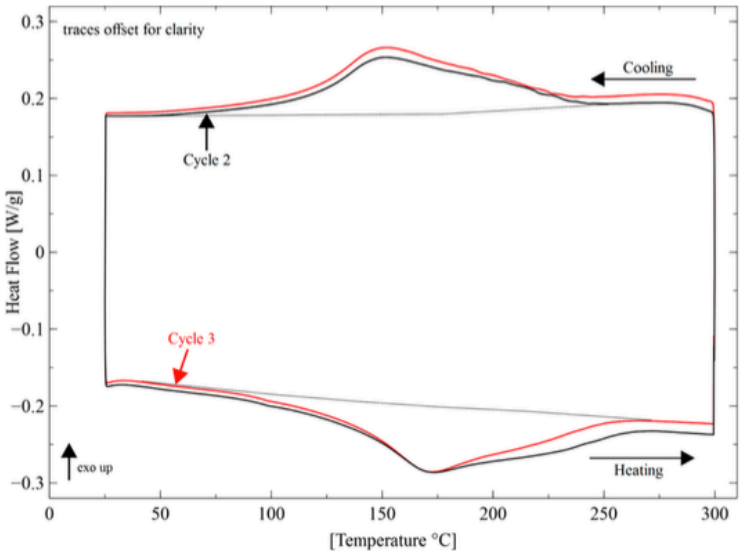

Figure 6. Differential scanning calorimetry (DSC) data for 70 mol % NaH + 30 mol % NaOH. The first cycle (not shown) was heated to 330 °C to premelt the mixture. The subsequent cycles below the melting temperature of NaOH show the reversible behavior. The dotted “baselines” are a guide for the eyes.

+ 60 mol % NaOH sample heated up to 260 °C. At 260 °C the sample is almost completely mixed into a single fcc phase solid solution. As the sample cools, the fcc pha-

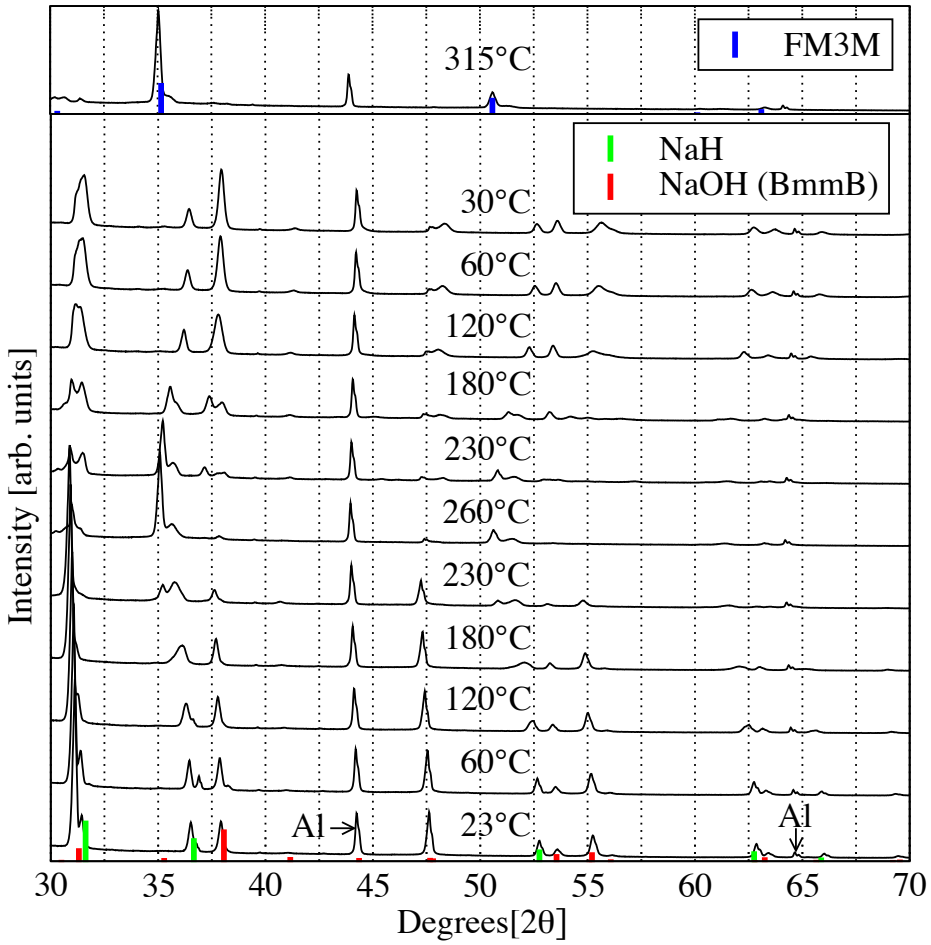

Figure 7. In situ X-ray diffraction data of the heating and cooling process for 40 mol % NaH + 60 mol % NaOH sample. The first scan is indicated at 23 °C, and the last scan is indicated at 30 °C. Vertical guidelines (dotted lines) are given to emphasize the peak shifts. The marked Al peaks were generated by the aluminum sample holder.

se solid solution is still present at 180 °C (but shifted to higher angle), but some of the solid solution has now phase separated into B*mm*b phase NaOH and NaH. As the sample

reaches room temperature, NaH and NaOH are mostly phase separated. Heating and cooling the samples during subsequent cycles showed the same repeatable behavior noted in the DSC measurements. At 315 °C (top panel in Figure 7) the sample *completely mixed* into an fcc structure solid solution. Similar results were obtained for compositions of 90, 70, 50, and 25 mol % NaH, respectively. These results suggest necessary modifications to the phase diagram as presented in Mikheeva's work. The region of fcc β solid solutions should be extended to higher NaH concentrations at temperatures of >260 °C to accommodate hydride rich compositions that continue to form solid solutions. Further, the region where α and β solid solutions exist simultaneously shown in Mikheeva's phase diagram should possibly be extended to include higher NaH concentrations, as the X-ray diffraction data clearly show the existence of the two phases for concentrations outside the allowed region in Mikheeva's diagram. However, sluggish kinetics at lower temperature may be responsible for incomplete phase separation.

The NaH lattice parameters were extracted from the in situ X-ray diffraction data by implementing full pattern Rietveld refinement from the general structure analysis system (GSAS) [25,26]. The NaH lattice expansion and unit cell volume expansion of NaH in the 40 mol % NaH + 60 mol % NaOH sample are compared to that of pure NaH in Figure 8. The comparison shows that NaH in the 40 mol % NaH + 60 mol % NaOH sample has a much larger lattice expansion than pure NaH when heated using the same process. Also, the lattice expansion is not linear. The two-point coefficients of linear expansion, calculated using room temperature and the highest temperature point, for pure NaH and NaH in the 40 mol % NaH + 60 mol % NaOH sample are 37×10^{-6}/°C and 72×10^{-6}/°C, respectively. The massive volume expansion of the NaH in the 40 mol % NaH + 60 mol % NaOH sample is evidently due to the formation of solid solution on heating.

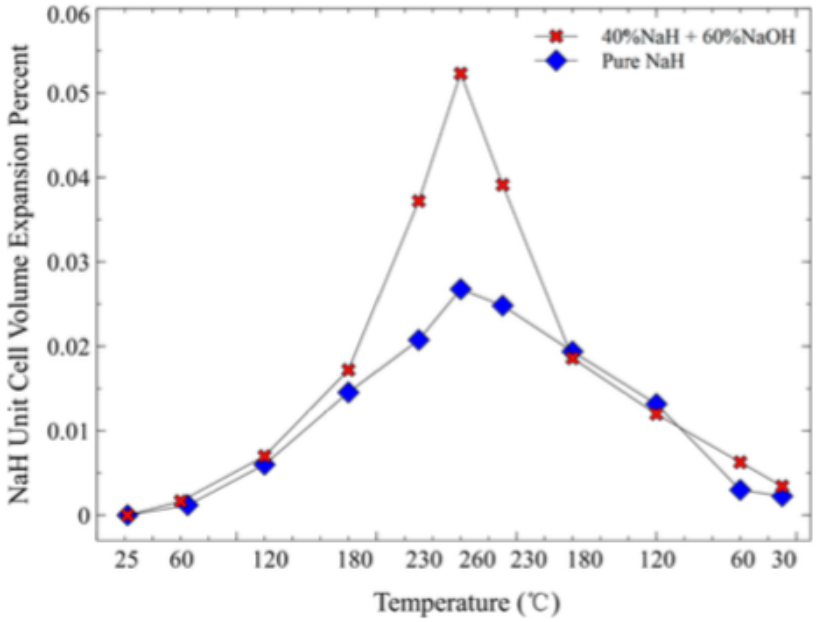

Figure 8. Cell volumes via XRD for pure NaH and 40 mol % NaH + 60 mol % NaOH mixture as a function of temperature during a heating and cooling cycle between 25 and 260 °C.

CONCLUSIONS

The formation of a solid solution in MH/MOH mixtures is governed by the volume difference available for H^- and OH^- anions in their parent phases of MH and MOH, respectively. Mixing occurs when volume differences are less than about 15% with lower critical temperatures for smaller volume differences. Small additions of hydroxide ion in the KH and RbH systems stabilize these hydrides, and the mixtures decompose at temperatures above the pure hydride decomposition temperature. In contrast, small hydroxide addition to NaH tends to lower the decomposition temperature of the mixture. There is no predicted solid solution in the LiH/LiOH and CsH/CsOH systems due to decomposition before mixing. When solid solution formation occurs in the NaH/NaOH system, the phase transitions in NaOH are concomitant with mixing and the high temperature structure is a single phase fcc before melting. This combination of phase transitions and mixing is fully reversible on cooling.

ACKNOWLEDGEMENTS

The authors gratefully acknowledge support from the U.S. Department of Energy, Basic Energy Science, through Grant DE-FG02-ER46256. T.E.-C. acknowledges partial support from Washington University's Office of Undergraduate Research. We thank David Osborn in the Center for Nanoscience for assistance in collecting the in situ XRD and DSC data. We also thank Bruce Burkeen in the University of Missouri St. Louis Research and Development Tech Shop for his work fabricating experimental equipment.

REFERENCES

[1] Bogdanović, B.; Schwickardi, M. Ti-doped $NaAlH_4$ as a Hydrogen-Storage Material-Preparation by Ti-Catalyzed Hydrogenation of Aluminum Powder in Conjunction with Sodium Hydride. *Appl. Phys. A: Mater. Sci. Process.* **2000**, 72, 221−223.

[2] Michel, K.; Ozolins, V. Native Defect Concentrations in $NaAlH_4$ and Na_3AlH_6. *J. Phys. Chem. C* **2011**, 115, 21443−21453.

[3] Michel, K.; Ozolins, V. Vacancy Diffusion in $NaAlH_4$ and Na_3AlH_6. *J. Phys. Chem. C* **2011**, 115, 21465−21472.

[4] Morioka, H.; Kakizaki, K.; Chung, C.; Yamada, A. Reversible Hydrogen Decomposition of $KAlH_4$. *J. Alloys Compd*. **2003**, 353, 310− 314.

[5] Sorte, E. G.; Majzoub, E. H.; Ellis-Caleo, T.; Hammann, B. A.; Wang, G.; Zhao, D.; Bowman, R. C., Jr.; Conradi, M. S. Effects of NaOH in Solid NaH: Solution/Segregation Phase Transition and Diffusion Acceleration. *J. Phys. Chem. C* **2013**, 117, 23575−23581.

[6] Mikheeva, V.; Shkrabkina, M. Solid Solutions in NaOH-NaH and KOH-KH Systems. *Russ. J. Inorg. Chem.* **1962**, 7, 1251−1255.

[7] Kresse, G.; Hafner, J. Ab Initio Molecular Dynamics for Liquid Metals. *Phys. Rev. B* **1993**, 47, 558−561.

[8] Kresse, G.; Furthmüller, J. Efficient Iterative Schemes for ab Initio Total-Energy Calculations Using a Plane-Wave Basis Set. *Phys. Rev. B* **1996**, 54, 11169−11186.

[9] Perdew, J.; Chevary, J.; Vosko, S.; Jackson, K.; Pederson, M.; Singh, D.; Fiolhais, C. Atoms, Molecules, Solids, and Surfaces: Applications of the Generalized Gradient Approximation for Exchange and Correlation. *Phys. Rev. B* **1992**, 46, 6671−6687.

[10] Perdew, J.; Chevary, J.; Vosko, S.; Jackson, K.; Pederson, M.; Singh, D.; Fiolhais, C. Erratum: Atoms, Molecules, Solids, and Surfaces: Applications of the Generalized Gradient Approximation for Exchange and Correlation. *Phys. Rev. B* **1993**, 48, 4978−4978.

[11] Monkhorst, H.; Pack, J. Special Points for Brillouin-Zone Integrations. *Phys. Rev. B* **1976**, 13, 5188−5192.

[12] Kirkpatrick, S.; Gelatt, C., Jr.; Vecchi, M. Optimization by Simulated Annealing. *Science* **1983**, 220, 671−680.

[13] Akbarzadeh, A.; Ozolin, V.; Wolverton, C. First-Principles Determination of Multicomponent Hydride Phase Diagrams: Application to the Li-Mg-N-H System. *Adv. Mater*. **2007**, 19, 3233− 3239.

[14] Giauque, W. The Entropy of Hydrogen and the Third Law of Thermodynamics: The Free Energy and Dissociation of Hydrogen. *J. Am. Chem. Soc.* **1930**, 52, 4816−4831.

[15] Grindy, S.; Meredig, B.; Kirklin, S.; Saal, J.; Wolverton, C. Approaching Chemical Accuracy with Density Functional Calculations: Diatomic Energy Corrections. *Phys. Rev. B* **2013**, 87, 075150.

[16] Gurvich, L.; Bergman, G.; Gorokhov, L.; Iorish, V.; Leonidov, V.; Yungman, V. Thermodynamic Properties of Alkali Metal Hydroxides. Part 1. Lithium and Sodium Hydroxides. *J. Phys. Chem. Ref. Data* **1996**, 25, 1211−1276.

[17] Jensen, F. Locating Transition Structures by Mode Following: A Comparison of Six Methods on the Ar_8 Lennard-Jones Potential. *J. Chem. Phys*. **1995**, 102, 6706−6718.

[18] Kiat, J. M.; Boemare, G.; Rieu, B.; Aymes, D. Structural Evolution of LiOH: Evidence of a Solid−Solid Transformation toward Li_2O Close to the Melting Temperature. *Solid State Commun*. **1998**, 108, 241−245.

[19] Ren, R.; Ortiz, A. L.; Markmaitree, T.; Osborn, W.; Shaw, L. L. Stability of Lithium Hydride in Argon and Air. *J. Phys. Chem. B* **2006**, 110, 10567−10575.

[20] Haertling, C.; Hanrahan, R. J., Jr.; Smith, R. A Literature Review of Reactions and Kinetics of Lithium Hydride Hydrolysis. *J. Nucl. Mater*. **2006**, 349, 195−233.

[21] Haertling, C. L.; Hanrahan, R. J., Jr.; Tesmer, J. R. Hydrolysis Studies of Polycrystalline Lithium Hydride. *J. Phys. Chem. C* **2007**, 111, 1716−1724.

[22] Sifuentes, A.; Stowe, A. C.; Smyrl, N. Determination of the Role of Li_2O on the Corrosion of Lithium Hydride. *J. Alloys Compd*. **2013**, 580, S271−S273.

[23] Yu, P.; Chua, Y. S.; Cao, H.; Xiong, Z.; Wu, G.; Chen, P. Hydrogen Storage over Alkali Metal Hydride and Alkali Metal Hydroxide Composites. *J. Energy Chem.* **2014**, 23, 414−419.

[24] Kittel, C. *Introduction to Solid State Physics*, 5th ed.; John Wiley & Sons, Inc.: New York, 1976.

[25] Toby, B. H. EXPGUI, a Graphical User Interface for GSAS. *J. Appl. Crystallogr*. **2001**, 34, 210−213.

[26] Larson, A.; Von Dreele, R. *General Structure Analysis System (GSAS)*; Los Alamos National Laboratory Report LAUR; Los Alamos National Laboratory: Los Alamos, NM, 2004; pp 86−748.

SUPPORTING INFORMATION

Table S1. Unit Cell Dimensions and Space Group Symmetries for all Structures used in this work

Material	*a* (Å)	*b* (Å)	*c* (Å)	α	β	γ	*V* (Å^3)	Space Group Before Relaxation	Space Group After Relaxation	f.u.
H_2	20	20	20	90	90	90	-	-	-	1
LiH	8.02	8.02	8.02	90	90	90	515.35	$Fm\bar{3}m$	$Fm\bar{3}m$	32
LiOH	7.14	7.14	8.97	89.97	86.53	93.47	455.35	*P*1	*P*1	16
Li_2O	4.63	4.63	4.63	90	90	90	99.4	*P*4*mm*	*P*4*mm*	4
Na	8.41	8.41	8.41	90	90	90	594.19	$Im\bar{3}m$	$Im\bar{3}m$	16
NaH	9.64	9.64	9.64	90	90	90	896.57	$Fm\bar{3}m$	$Fm\bar{3}m$	32
NaOH	6.98	6.78	20.63	90	90	90	975.43	*Bmmb*	$Cmc2_1$	32
Na_2O	5.56	5.56	5.56	90	90	90	172.09	$Fm\bar{3}m$	$Fm\bar{3}m$	4
K	10.55	10.55	10.55	90	90	90	1175.39	$Im\bar{3}m$	$Im\bar{3}m$	16
KH	11.37	11.37	11.37	90	90	90	1471.19	$Fm\bar{3}m$	$Fm\bar{3}m$	32
KOH	8.01	7.98	21.33	90	90	90	1362.97	*Bmmb*	*P*1	32
Rb	11.33	11.33	11.33	90	90	90	1453.86	$Im\bar{3}m$	$Im\bar{3}m$	16

Table S1. Unit Cell Dimensions and Space Group Symmetries for all Structures used in this work (Cont)

RbH	12.07	12.07	12.07	90	90	90	1759.35	$Fm\bar{3}m$	$Fm\bar{3}m$	32
RbOH	8.42	8.46	22.08	90	90.08	90	1571.43	*Bmmb*	*Pc*	32
Cs	12.28	12.28	12.28	90	90	90	1851.64	$Im\bar{3}m$	$Im\bar{3}m$	16
CsH	12.85	12.85	12.85	90	90	90	2120.39	$Fm\bar{3}m$	$Fm\bar{3}m$	32
$Li_{32}H_{31}OH$	8.06	8.06	8.06	90.3	90.3	90.3	523.02	*P*1	*R*3*m*	32
$Na_{32}H_{31}OH$	9.66	9.66	9.66	90.3	90.3	90.3	901.11	*P*1	*P*1	1
$Na_{32}H_{30}(OH)_2$	9.67	9.67	9.67	90.61	90.61	90.61	904.8	*P*1	*P*1	1
$Na_{32}H_{29}(OH)_3$	9.72	9.68	9.68	91	91	91	909.67	*P*1	*P*1	1
$Na_{32}H_{28}(OH)_4$	9.71	9.69	9.71	90.25	91.6	90.25	913.87	*P*1	*P*1	1
$Na_{32}H_{27}(OH)_5$	9.72	9.72	9.72	91.54	91.54	91.54	919.5	*P*1	*P*1	1
$Na_{32}H_{26}(OH)_6$	9.65	9.77	9.76	90.28	90.36	92.17	919.83	*P*1	*P*1	1
$Na_{32}H_{25}(OH)_7$	9.69	9.76	9.78	90.43	91.25	92.02	923.4	*P*1	*P*1	1
$Na_{32}H_{24}(OH)_8$	9.71	9.71	9.71	92.34	92.34	92.34	931.31	*P*1	*P*1	1
$Na_{32}H_{23}(OH)_9$	9.72	9.75	9.82	91.27	91.49	92.84	928.46	*P*1	*P*1	1
$Na_{32}H_{22}(OH)_{10}$	9.87	9.73	9.71	94.3	92.87	89.78	928.06	*P*1	*P*1	1
$Na_{32}H_{21}(OH)_{11}$	9.77	9.76	9.81	91.9	92.41	92.71	932	*P*1	*P*1	1
$Na_{32}H_{20}(OH)_{12}$	9.78	9.87	9.72	94.99	90.47	92.7	933.87	*P*1	*P*1	1
$Na_{32}H_{19}(OH)_{13}$	9.76	9.83	9.84	92.77	91.89	93.53	939.43	*P*1	*P*1	1
$K_{32}H_{31}OH$	11.38	11.38	11.38	90.27	90.27	90.27	1472.88	*P*1	*R*3*m*	1
$K_{32}H_{30}(OH)_2$	11.38	11.38	11.38	90.55	90.55	90.55	1474.56	*P*1	*R*3*m*	1
$K_{32}H_{28}(OH)_4$	11.41	11.37	11.41	90.21	91.44	90.21	1479.67	*P*1	*Cm*	1
$K_{32}H_{27}(OH)_5$	11.39	11.39	11.39	90.49	90.49	90.49	1479.11	*P*1	$C3_4$	1
$K_{32}H_{26}(OH)_6$	11.33	11.43	11.42	91.79	90.37	90.29	1478.24	*P*1	*P*1	1
$K_{32}H_{25}(OH)_7$	11.36	11.4	11.41	91.66	90.93	90.31	1476.77	*P*1	*P*1	1
$K_{32}H_{24}(OH)_8$	11.42	11.42	11.42	92.09	92.09	92.09	1487.08	*P*1	*P*1	1
$K_{32}H_{23}(OH)_9$	11.36	11.38	11.43	92.31	91.14	91.02	1476.85	*P*1	*P*1	1
$K_{32}H_{22}(OH)_{10}$	11.42	11.36	11.35	89.74	92.51	93.86	1466.77	*P*1	*P*1	1
$K_{32}H_{21}(OH)_{11}$	11.4	11.37	11.41	92.28	91.82	91.6	1477.31	*P*1	*P*1	1
$K_{32}H_{20}(OH)_{12}$	11.36	11.45	11.35	93.02	89.73	94.55	1468.47	*P*1	*P*1	1
$K_{32}H_{19}(OH)_{15}$	11.38	11.43	11.28	89.78	87.53	97.98	1452.06	*P*1	*P*1	1
$Rb_{32}H_{31}OH$	12.07	12.07	12.07	90.24	90.24	90.24	1757.58	*P*1	*R*3*m*	1
$Rb_{32}H_{30}(OH)_2$	12.07	12.07	12.07	90.48	90.48	90.48	1760.02	*P*1	*R*3*m*	1
$Rb_{32}H_{29}(OH)_3$	12.14	12.05	12.05	90.38	90.79	90.79	1762.75	*P*1	*Cm*	1
$Rb_{32}H_{28}(OH)_4$	12.1	12.05	12.1	90.17	91.25	90.17	1764.42	*P*1	*Cm*	1
$Rb_{32}H_{27}(OH)_5$	12.09	12.09	12.09	90.4	90.4	90.4	1765.44	*P*1	*R*3	1
$Rb_{32}H_{24}(OH)_8$	12.11	12.11	12.11	91.89	91.89	91.89	1771.55	*P*1	*P*1	1

Table S2. K-point Meshes, Total Energies, Vibrational Energies and Entropies for all Structures

Material	k-point	U_E (eV)	ZPE (eV)	S_{conf} (eV/K)	S_c (J/mol/K)	S_e (J/mol/K)
H_2	2x2x2	-6.80	0.27	-	130.70	130.70
LiH	2x2x2	-197.66	7.16	-	17.78	24.70
LiOH	2x2x2	-240.41	6.91	-	39.98	42.81
Li_2O	4x4x4	-57.75	0.89	-	33.88	37.90
Na	4x4x4	-20.89	0.25	-	45.04	51.00
NaH	2x2x2	-164.94	5.09	-	37.02	40.00
NaOH	2x2x2	-441.13	12.56	-	58.00	64.46
Na_2O	6x6x6	-45.66	0.49	-	68.46	73.00
K	4x4x4	-16.67	0.19	-	50.23	64.20
KH	2x2x2	-156.25	4.04	-	47.61	66.90
KOH	2x2x2	-431.45	11.98	-	70.86	79.00
Rb	2x2x2	-14.87	0.11	-	63.35	69.50
RbH	2x2x2	-150.16	3.49	-	61.02	-
RbOH	2x2x2	-424.17	11.52	-	119.32	84.10
Cs	2x2x2	-13.79	0.08	-	70.18	82.80
CsH	2x2x2	-147.85	3.06	-	75.00	-
$Li_{32}H_{31}OH$	2x2x2	-205.86	7.28	-	20.18	-
$Na_{32}H_{31}OH$	2x2x2	-173.35	5.25	0.00038	39.18	-
$Na_{32}H_{30}(OH)_2$	2x2x2	-181.77	5.46	0.00064	41.13	-
$Na_{32}H_{29}(OH)_3$	2x2x2	-190.20	5.65	0.00086	43.41	-
$Na_{32}H_{28}(OH)_4$	2x2x2	-198.66	5.86	0.00104	44.45	-
$Na_{32}H_{27}(OH)_5$	2x2x2	-207.01	6.05	0.00120	46.68	-
$Na_{32}H_{26}(OH)_6$	2x2x2	-215.71	6.29	0.00133	47.14	-
$Na_{32}H_{25}(OH)_7$	2x2x2	-224.27	6.50	0.00145	48.22	-
$Na_{32}H_{24}(OH)_8$	2x2x2	-232.44	6.65	0.00155	51.33	-
$Na_{32}H_{23}(OH)_9$	2x2x2	-241.33	6.97	0.00164	50.23	-
$Na_{32}H_{22}(OH)_{10}$	2x2x2	-249.98	7.22	0.00171	50.73	-
$Na_{32}H_{21}(OH)_{11}$	2x2x2	-258.43	7.47	0.00177	52.38	-
$Na_{32}H_{20}(OH)_{12}$	2x2x2	-266.99	7.70	0.00182	53.17	-
$Na_{32}H_{19}(OH)_{13}$	2x2x2	-275.55	7.89	0.00186	54.15	-
$K_{32}H_{31}OH$	2x2x2	-164.70	4.19	0.00038	1626.16	-
$K_{32}H_{30}(OH)_2$	2x2x2	-173.16	4.41	0.00064	1681.41	-
$K_{32}H_{28}(OH)_4$	2x2x2	-190.13	4.82	0.00104	1805.78	-
$K_{32}H_{27}(OH)_5$	2x2x2	-198.64	5.05	0.00120	1846.11	-
$K_{32}H_{26}(OH)_6$	2x2x2	-207.20	5.27	0.00133	1877.75	-

Table S2. K-point Meshes, Total Energies, Vibrational Energies and Entropies for all Structures (Cont)

$K_{32}H_{25}(OH)_7$	2x2x2	-215.77	5.50	0.00145	1919.05	-
$K_{32}H_{24}(OH)_8$	2x2x2	-224.14	5.66	0.00155	1999.59	-
$K_{32}H_{23}(OH)_9$	2x2x2	-232.78	5.95	0.00164	1996.80	-
$K_{32}H_{22}(OH)_{10}$	2x2x2	-241.35	6.24	0.00171	2003.50	-
$K_{32}H_{21}(OH)_{11}$	2x2x2	-249.77	6.41	0.00177	2073.20	-
$K_{32}H_{20}(OH)_{12}$	2x2x2	-258.31	6.69	0.00182	2078.82	-
$K_{32}H_{19}(OH)_{15}$	2x2x2	-284.11	7.43	0.00191	2151.89	-
$Rb_{32}H_{31}OH$	2x2x2	-158.16	3.67	0.00038	2054.21	-
$Rb_{32}H_{30}(OH)_2$	2x2x2	-167.05	3.88	0.00064	2126.15	-
$Rb_{32}H_{29}(OH)_3$	2x2x2	-175.54	4.07	0.00086	2189.45	-
$Rb_{32}H_{28}(OH)_4$	2x2x2	-184.01	4.28	0.00104	2242.71	-
$Rb_{32}H_{27}(OH)_5$	2x2x2	-192.50	4.50	0.00120	2303.77	-
$Rb_{32}H_{24}(OH)_8$	2x2x2	-217.98	5.10	0.00155	2527.74	-

Table S3. The Solution Temperatures, Decomposition Temperatures and Enthalpies for the NaH/NaOH System

Material	T_c (°C)	ΔH_1 (J/g)	T_d (°C)
$Na_{32}H_{31}OH$	69	22	364
$Na_{32}H_{30}(OH)_2$	120	46	364
$Na_{32}H_{29}(OH)_3$	100	67	369
$Na_{32}H_{28}(OH)_4$	158	84	363
$Na_{32}H_{27}(OH)_5$	179	114	363
$Na_{32}H_{26}(OH)_6$	159	104	361
$Na_{32}H_{25}(OH)_7$	155	108	355
$Na_{32}H_{24}(OH)_8$	176	153	361
$Na_{32}H_{23}(OH)_9$	200	128	326
$Na_{32}H_{22}(OH)_{10}$	205	123	319
$Na_{32}H_{21}(OH)_{11}$	221	143	314
$Na_{32}H_{20}(OH)_{12}$	237	146	307
$Na_{32}H_{19}(OH)_{13}$	239	152	307

Table S4. The Solution Temperatures, Decomposition Temperatures and Enthalpies for the KH/KOH System

Material	T_c (°C)	ΔH_1 (J/g)	T_d (°C)
$K_{32}H_{31}OH$	-168	5	465
$K_{32}H_{30}(OH)_2$	-83	15	473
$K_{32}H_{28}(OH)_4$	-71	26	504
$K_{32}H_{27}(OH)_5$	-51	32	512
$K_{32}H_{26}(OH)_6$	-46	33	518
$K_{32}H_{25}(OH)_7$	-58	33	532
$K_{32}H_{24}(OH)_8$	-39	46	564
$K_{32}H_{23}(OH)_9$	-21	45	553
$K_{32}H_{22}(OH)_{10}$	16	49	541
$K_{32}H_{21}(OH)_{11}$	16	58	576
$K_{32}H_{20}(OH)_{12}$	61	64	560
$K_{32}H_{19}(OH)_{15}$	56	62	596

Table S5. The Solution Temperatures, Decomposition Temperatures and Enthalpies for the RbH/RbOH System

Material	T_c (°C)	ΔH_1 (J/g)	T_d (°C)
$Rb_{32}H_{31}OH$	-209	1.4	361
$Rb_{32}H_{30}(OH)_2$	-158	4.5	375
$Rb_{32}H_{29}(OH)_3$	-140	7.1	387
$Rb_{32}H_{28}(OH)_4$	-124	9.4	397
$Rb_{32}H_{27}(OH)_5$	-144	9.1	418
$Rb_{32}H_{24}(OH)_8$	-176	10	524

APPENDIX B.

MODIFICATIONS TO THE RESIDUAL GAS ANALYSIS MASS SPECTROMETER

RGA-MS Safety Shut Down System

In the event of a mains power failure or loss of cooling water flow the RGA-MS safety circuit is designed to protect the system turbo pumps from damage. Figure 1 shows an electrical schematic for the safety shut down system. In the event of a mains failure or

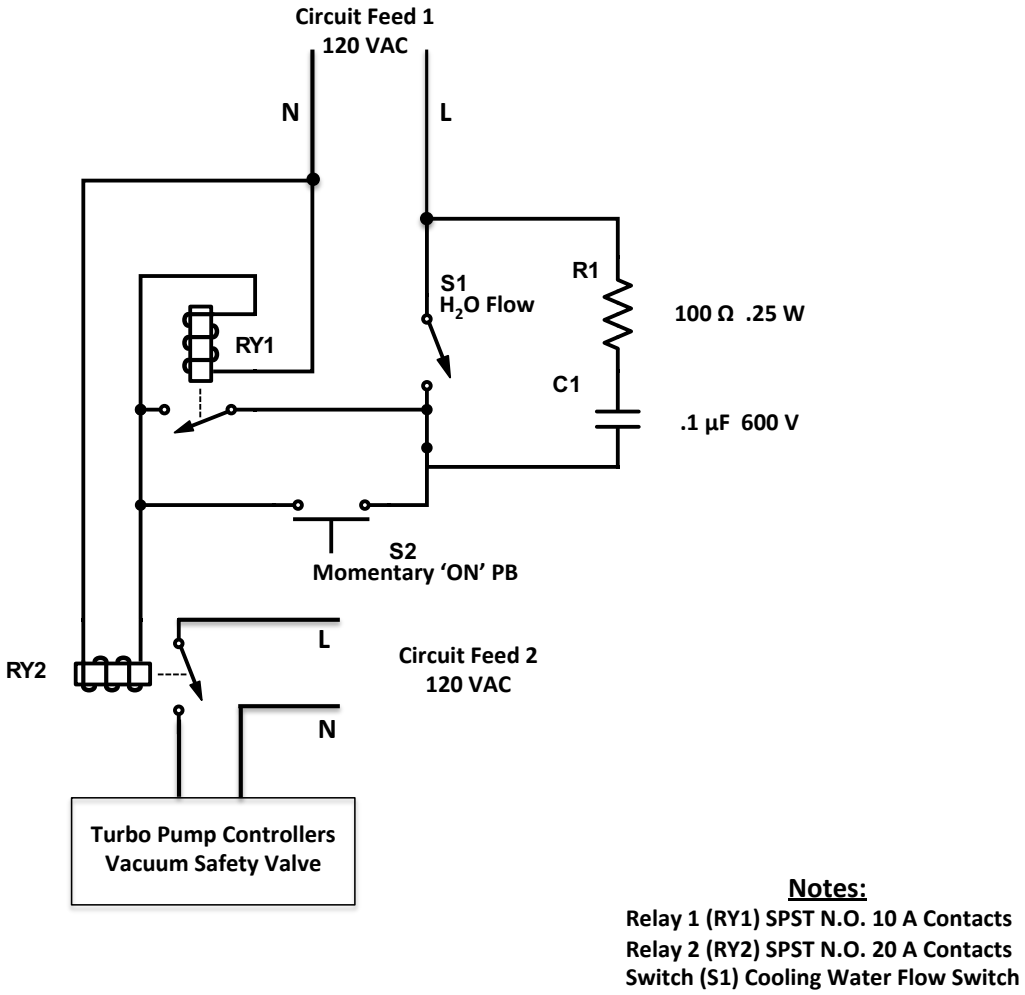

Figure 1. Electrical schematic for RGA-MS safety shut down system.

loss of sufficient cooling water flow the relay 1 contacts open, cutting the feed to the relay 2 coil, opening the power supply feed to the vacuum safety valve and turbo pump controllers. With loss of power the vacuum safety valve closes, isolating the HV lower chamber from the roughing pump to prevent the back flow of air and oil vapor into the chamber and to maintain a sufficiently low pressure within the chamber as the turbo pump decelerates to a stop. A DC voltage is supplied to a safety valve for the UHV chamber (not shown) through its respective controller, which performs an automatic venting/shutdown routine for the top UHV chamber. Due to an internal capacitive supply voltage, when the AC power supply to the upper turbo pump controller is interrupted the controller remains on for a short period of time sufficient to allow the shut down routine to be executed. Upon restoral of the mains and/or cooling water flow the system requires a manual reset, which allows the operator to determine if the turbo pumps can be safely restarted. The operator should ensure the pressure within the chambers is sufficiently low (~1.0 E-4 Torr) to facilitate the starting of the turbo pumps. ***Note: The lower turbo pump controller features a latching push button ('Pumping Unit') that remains in the 'ON' position once depressed. The operator should ensure the 'Pumping Unit' button is out (Not Depressed) before resetting the safety shut down circuit.***

To reset the safety shut down circuit first ensure the RGA-MS system is safe to start (As noted above and in the RGA OPERATING MANUAL), then depress the manual restart switch and release (Switch S2 in Figure 1). Momentarily depressing the switch supplies line voltage to the relay 1 coil closing the relay 1 contacts. Since line voltage is switched through these contacts and run to the relay 1 coil the contacts remain latched when switch S2 is released. Upon loss of line voltage at the relay 1 coil from a mains or water flow failure the relay 1 contacts open and thus cannot reclose without a manual intervention.

RGA-MS High Temperature Sample Stage Upgrade

An upgrade of the RGA-MS sample stage and heating components was performed to allow TPD studies at temperatures in excess of 450 °C, increase the longevity of the heating system components to minimize equipment downtime, and allow the sample

temperature to be increased at a linear rate during experiments. In addition, the power supply system/temperature controller was refitted with a more durable solid-state relay (SSR) and semiconductor fuse protection circuit. The old system featured a heater block and thermocouple fixed in place inside the vacuum chamber. Samples were loaded by inserting samples prepared in TA Instruments Tzero pans into a removable insert that fit into the heater block. Temperature was recorded by a thermocouple in contact with the heater block, but not the insert. A second thermocouple inserted in a sample pan filled with glass beads was used to calibrate the sample temperature as a function of the heater block temperature for different linear temperature controller ramp rates (1, 2, 4, and 8 °C/min). This design had three immediate shortcomings: 1.) sample temperature was a non-linear function of the controller temperature, 2.) the size/mass of the heater block sample insert was large compared to the sample pans, requiring extra energy to heat the actual sample and 3.) heat transfer had to occur at the interface between the heater block/insert and insert/sample. The new design overcomes these problems by incorporating a removable heater block. No insert is required as the small sample pans can now be loaded directly into the heater block. As a result, the heater block's physical dimensions could be reduced. Heaters conforming to the new dimensions with the ability to increase the power output by 33% were selected. A thermocouple well, lined with an insulated insert was incorporated into the block, insulating the sides of the 1/16" sheathed thermocouple from the heating block except at the thermocouple tip inserted directly next to the sample pan. Due to the small mass of the sample pans compared to the heater block and the tight tolerance of the pan well it is a good approximation to assume the block and sample temperature in vicinity of the thermocouple tip are the same in the new design. Figure 2 shows the sample temperature as a function of time for a 4 °C/min programmed controller ramp rate with the old/new designs. An idealized 4 °C/min slope trace is shown for reference. There is a small deviation from the idealized ramp rate at the start of a TPD run with the new design, but is a large improvement over the old design. As a result of the new design's heat transfer efficiency less time is required to achieve the desired final sample temperature, thus reducing the overall heater load during TPD. Figure 3 shows the new heater block assembly before installation in the vacuum chamber. Once installed

in the chamber the length of the heater wires and removable thermocouple allow the heater block to be accessed from a 6” conflat flange at the front of the chamber (dashed blue lines in Figure 3). Locating washers on the heater block support ensure proper heater block placement during TPD runs.

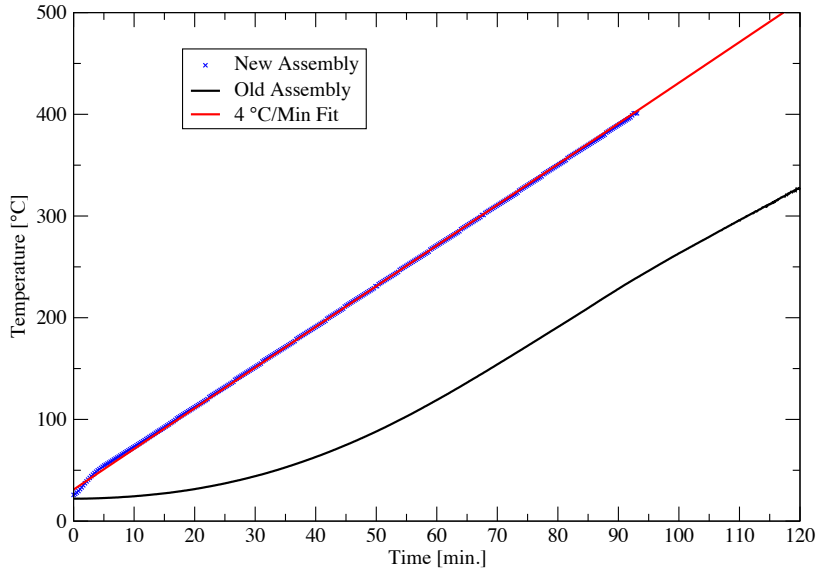

Figure 2. A comparison of the sample temperature as a function of time for the new and old sample heating stages. An idealized trace with a 4 °C/min slope is shown for reference.

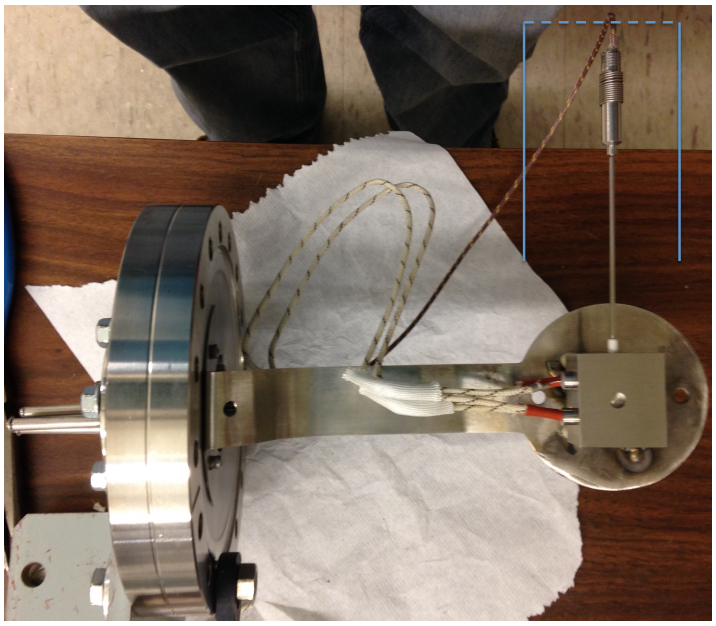

Figure 3. View from above of the new heater block assembly before installation. Once installed, the operator accesses the sample stage from a 6" conflat (w/viewport) at the front (dashed blue lines) of the access chamber. Solid blue lines indicate the orientation of the stage to the access port.

PID Controller Settings Determined From Tuning Routine

Cycle Time:	0.2 s
Proportional Band:	74
Integral Time:	8.8 s
Derivative Time:	38 s
Derivative Approach Control:	5
Derivative Sensitivity:	1.0

REFERENCES

[1] BP p.l.c. BP Energy Outlook 2017 Edition. 2017.

[2] Alanne, K.; Cao, S. Zero-Energy Hydrogen Economy (ZEH_2E) for Buildings and Communities Including Personal Mobility. *Renewable Sustainable Energy Rev.* **2017**, *71*, 697–711.

[3] Acar, C.; Dincer, I.; Naterer, G. F. Review of Photocatalytic Water-Splitting Methods for Sustainable Hydrogen Production: Review: Photocatalysis for Sustainable Hydrogen. *Int. J. Energy Res.* **2016**, *40*, 1449–1473.

[4] Grochala, W.; Edwards, P. P. Thermal Decomposition of the Non-Interstitial Hydrides for the Storage and Production of Hydrogen. *Chem. Rev.* **2004**, *104*, 1283–1316.

[5] Zhang, F.; Zhao, P.; Niu, M.; Maddy, J. The Survey of Key Technologies in Hydrogen Energy Storage. *Int. J. Hydrogen Energy* **2016**, *41*, 14535–14552.

[6] Stetson, N. Hydrogen Storage Overview. *Proceedings of the 2016 US DOE Hydrogen and Fuel Cells Program Annual Merit Review* **2016**.

[7] Dincer, I. Green Methods for Hydrogen Production. *Int. J. Hydrogen Energy* **2012**, *37*, 1954–1971.

[8] Laguna-Bercero, M. A. Recent Advances in High Temperature Electrolysis Using Solid Oxide Fuel Cells: A Review. *J. Power Sources* **2012**, *203*, 4–16.

[9] Bicer, Y.; Dincer, I.; Zamfirescu, C. Effects of Various Solar Spectra on Photovoltaic Cell Efficiency and Photonic Hydrogen Production. *Int. J. Hydrogen Energy* **2016**, *41*, 7935–7949.

[10] Bermel, P.; Yazawa, K.; Gray, J. L.; Xu, X.; Shakouri, A. Hybrid Strategies and Technologies for Full Spectrum Solar Conversion. *Energy Environ. Sci.* **2016**, *9*, 2776–2788.

[11] Durbin, D. J.; Malardier-Jugroot, C. Review of Hydrogen Storage Techniques For On Board Vehicle Applications. *Int. J. Hydrogen Energy* **2013**, *38*, 14595–14617.

[12] Hwang, H. T.; Varma, A. Hydrogen Storage for Fuel Cell Vehicles. *Curr. Opin. Chem. Eng.* **2014**, *5*, 42–48.

[13] Züttel, A. Materials for Hydrogen Storage. *Mater. Today* **2003**, *6*, 24–33.

[14] Ahluwalia, R. K.; Hua, T. Q.; Peng, J.-K.; Lasher, S.; McKenney, K.; Sinha, J.; Gardiner, M. Technical Assessment of Cryo-Compressed Hydrogen Storage Tank Systems for Automotive Applications. *Int. J. Hydrogen Energy* **2010**, *35*, 4171–4184.

[15] Jack G. Calvert. Glossary of Atmospheric Chemistry Terms. *Pure & Appl. Chem.* **1990**, *62*, 2167–2219.

[16] Ströbel, R.; Garche, J.; Moseley, P. T.; Jörissen, L.; Wolf, G. Hydrogen Storage by Carbon Materials. *J. Power Sources* **2006**, *159*, 781–801.

[17] Wang, L.; Yang, R. T. Hydrogen Storage on Carbon-Based Adsorbents and Storage at Ambient Temperature by Hydrogen Spillover. *Catal. Rev.* **2010**, *52*, 411–461.

[18] Yürüm, Y.; Taralp, A.; Veziroglu, T. N. Storage of Hydrogen in Nanostructured Carbon Materials. *Int. J. Hydrogen Energy* **2009**, *34*, 3784–3798.

[19] Cai, J.; Bennici, S.; Shen, J.; Auroux, A. The Influence of Metal- and N-Species Addition in Mesoporous Carbons on the Hydrogen Adsorption Capacity. *Mater. Chem. Phys.* **2015**, *161*, 142–152.

[20] Wang, L.; Yang, R. T. New Sorbents for Hydrogen Storage by Hydrogen Spillover – a Review. *Energy Environ. Sci.* **2008**, *1*, 268–279.

[21] Wang, L.; Yang, R. T. Hydrogen Storage Properties of N-Doped Microporous Carbon. *J. Phys. Chem. C* **2009**, *113*, 21883–21888.

[22] Jia, Y.; Sun, C.; Shen, S.; Zou, J.; Mao, S. S.; Yao, X. Combination of Nanosizing and Interfacial Effect: Future Perspective for Designing Mg-Based Nanomaterials for Hydrogen Storage. *Renewable Sustainable Energy Rev.* **2015**, *44*, 289–303.

[23] Sakintuna, B.; Lamaridarkrim, F.; Hirscher, M. Metal Hydride Materials for Solid Hydrogen Storage: A Review. *Int. J. Hydrogen Energy* **2007**, *32*, 1121–1140.

[24] Webb, C. J. A Review of Catalyst-Enhanced Magnesium Hydride as a Hydrogen Storage Material. *J. Phys. Chem. Solids* **2015**, *84*, 96–106.

[25] Dornheim, M.; Doppiu, S.; Barkhordarian, G.; Boesenberg, U.; Klassen, T.; Gutfleisch, O.; Bormann, R. Hydrogen Storage in Magnesium-Based Hydrides and Hydride Composites. *Scr. Mater.* **2007**, *56*, 841–846.

[26] Liu, T.; Wang, C.; Wu, Y. Mg-Based Nanocomposites with Improved Hydrogen Storage Performances. *Int. J. Hydrogen Energy* **2014**, *39*, 14262–14274.

[27] Jacob, I.; Bereznitsky, M.; Mogilyanski, D. In Pursuit of Light Intermetallic Hydrides. *J. Alloys Compd.* **2015**, *645*, S524–S528.

[28] Bogdanović, B.; Schwickardi, M. Ti-Doped Alkali Metal Aluminium Hydrides as Potential Novel Reversible Hydrogen Storage Materials. *J. Alloys Compd.* **1997**, *253*, 1–9.

[29] Bogdanović, B.; Brand, R. A.; Marjanović, A.; Schwickardi, M.; Tölle, J. Metal-Doped Sodium Aluminium Hydrides as Potential New Hydrogen Storage Materials. *J. Alloys Compd.* **2000**, *302*, 36–58.

[30] Dymova, T. N.; Dergachev, Y. M.; Sokolov, V. A.; Grechanaya, N. A. Dissociation Pressure of $NaAlH_4$: And Na_3AlH_6 : *Dokl. Akad. Nauk SSSR* **1975**, *224*, 591–592, Engl. 556–557.

[31] Dymova, T. N.; Eliseeva, N. G.; Bakum, S. I.; Dergachev, Y. M. Direct Synthesis of Alkali Metal Aluminum Hydrides In the Melt. *Dokl. Akad. Nauk SSSR* **1974**, *215*, 1369–1372, Engl. 256–259.

[32] Zidan, R. A.; Takara, S.; Hee, A. G.; Jensen, C. M. Hydrogen Cycling Behavior of Zirconium and Titanium–zirconium-Doped Sodium Aluminum Hydride. *J. Alloys Compd.* **1999**, *285*, 119–122.

[33] Gross, K. J.; Guthrie, S.; Takara, S.; Thomas, G. In-Situ X-Ray Diffraction Study of the Decomposition of $NaAlH_4$. *J. Alloys Compd.* **2000**, *297*, 270–281.

[34] Jensen, C. M.; Gross, K. J. Development of Catalytically Enhanced Sodium Aluminum Hydride as a Hydrogen-Storage Material: *Appl. Phys. A: Mater. Sci. Process.* **2001**, *72*, 213–219.

[35] Sandrock, G.; Gross, K.; Thomas, G. Effect of Ti-Catalyst Content on the Reversible Hydrogen Storage Properties of the Sodium Alanates. *J. Alloys Compd.* **2002**, *339*, 299–308.

[36] Gross, K. J.; Thomas, G. J.; Jensen, C. M. Catalyzed Alanates for Hydrogen Storage. *J. Alloys Compd.* **2002**, *330*, 683–690.

[37] Züttel, A.; Wenger, P.; Rentsch, S.; Sudan, P.; Mauron, P.; Emmenegger, C. $LiBH_4$ a New Hydrogen Storage Material. *J. Power Sources* **2003**, *118*, 1–7.

[38] Züttel, A.; Rentsch, S.; Fischer, P.; Wenger, P.; Sudan, P.; Mauron, P.; Emmenegger, C. Hydrogen Storage Properties of $LiBH_4$. *J. Alloys Compd.* **2003**, *356-357*, 515–520.

[39] Miwa, K.; Ohba, N.; Towata, S.; Nakamori, Y.; Orimo, S. First-Principles Study on Lithium Borohydride $LiBH_4$. *Phys. Rev. B* **2004**, *69* 245120.

[40] Vajo, J. J.; Skeith, S. L.; Mertens, F. Reversible Storage of Hydrogen in Destabilized $LiBH_4$. *J. Phys. Chem. B* **2005**, *109*, 3719–3722.

[41] Orimo, S.; Nakamori, Y.; Kitahara, G.; Miwa, K.; Ohba, N.; Towata, S.; Züttel, A. Dehydriding and Rehydriding Reactions of $LiBH_4$. *J. Alloys Compd.* **2005**, *404-406*, 427–430.

[42] Miwa, K.; Ohba, N.; Towata, S.; Nakamori, Y.; Orimo, S. First-Principles Study on Copper-Substituted Lithium Borohydride, $(Li_{1-x}Cu_x)BH_4$. *J. Alloys Compd.* **2005**, *404-406*, 140–143.

[43] Au, M.; Jurgensen, A. Modified Lithium Borohydrides for Reversible Hydrogen Storage. *J. Phys. Chem. B* **2006**, *110*, 7062–7067.

[44] Mauron, P.; Buchter, F.; Friedrichs, O.; Remhof, A.; Bielmann, M.; Zwicky, C. N.; Züttel, A. Stability and Reversibility of $LiBH_4$. *J. Phys. Chem. B* **2008**, *112*, 906–910.

[45] Stasinevich, D. S.; Egorenko, G. A. Thermographic Investigation of Alkali Metal and Magnesium Tetrahydroborates at Pressures up to 10 Atm. *Russ. J. Inorg. Chem.* **1968**, *13*, 341–343.

[46] Kostka, J.; Lohstroh, W.; Fichtner, M.; Hahn, H. Diborane Release from $LiBH_4$ /Silica-Gel Mixtures and the Effect of Additives. *J. Phys. Chem. C* **2007**, *111*, 14026–14029.

[47] Liu, X.; Peaslee, D.; Jost, C. Z.; Majzoub, E. H. Controlling the Decomposition Pathway of $LiBH_4$ via Confinement in Highly Ordered Nanoporous Carbon. *J. Phys. Chem. C* **2010**, *114*, 14036–14041.

[48] Liu, X.; Peaslee, D.; Jost, C. Z.; Baumann, T. F.; Majzoub, E. H. Systematic Pore-Size Effects of Nanoconfinement of $LiBH_4$: Elimination of Diborane Release and Tunable Behavior for Hydrogen Storage Applications. *Chem. Mater.* **2011**, *23*, 1331–1336.

[49] Au, M.; Jurgensen, A. R.; Spencer, W. A.; Anton, D. L.; Pinkerton, F. E.; Hwang, S.-J.; Kim, C.; Bowman, R. C. Stability and Reversibility of Lithium Borohydrides Doped by Metal Halides and Hydrides. *J. Phys. Chem. C* **2008**, *112*, 18661–18671.

[50] Ozolins, V.; Majzoub, E. H.; Wolverton, C. First-Principles Prediction of Thermodynamically Reversible Hydrogen Storage Reactions in the Li-Mg-Ca-B-H System. *J. Am. Chem. Soc.* **2009**, *131*, 230–237.

[51] Hwang, S.-J.; Bowman, R. C.; Reiter, J. W.; Rijssenbeek; Soloveichik, G. L.; Zhao, J.-C.; Kabbour, H.; Ahn, C. C. NMR Confirmation for Formation of $[B_{12}H_{12}]^{2-}$ Complexes during Hydrogen Desorption from Metal Borohydrides. *J. Phys. Chem. C* **2008**, *112*, 3164–3169.

[52] Ohba, N.; Miwa, K.; Aoki, M.; Noritake, T.; Towata, S.; Nakamori, Y.; Orimo, S.; Züttel, A. First-Principles Study on the Stability of Intermediate Compounds of $LiBH_4$. *Phys. Rev. B* **2006**, *74* 075110.

[53] Gross, A. F.; Vajo, J. J.; Van Atta, S. L.; Olson, G. L. Enhanced Hydrogen Storage Kinetics of $LiBH_4$ in Nanoporous Carbon Scaffolds. *J. Phys. Chem. C* **2008**, *112*, 5651–5657.

[54] Baldé, C. P.; Hereijgers, B. P. C.; Bitter, J. H.; Jong, K. P. de. Sodium Alanate Nanoparticles – Linking Size to Hydrogen Storage Properties. *J. Am. Chem. Soc.* **2008**, *130*, 6761–6765.

[55] Wu, H.; Zhou, W.; Wang, K.; Udovic, T. J.; Rush, J. J.; Yildirim, T.; Bendersky, L. A.; Gross, A. F.; Van Atta, S. L.; Vajo, J. J.; et al. Size Effects on the Hydrogen Storage Properties of Nanoscaffolded $Li_3BN_2H_8$. *Nanotechnology* **2009**, *20*, 204002.

[56] Stephens, R. D.; Gross, A. F.; Van Atta, S. L.; Vajo, J. J.; Pinkerton, F. E. The Kinetic Enhancement of Hydrogen Cycling in $NaAlH_4$ by Melt Infusion into Nanoporous Carbon Aerogel. *Nanotechnology* **2009**, *20*, 204018.

[57] Gao, J.; Adelhelm, P.; Verkuijlen, M. H. W.; Rongeat, C.; Herrich, M.; van Bentum, P. J. M.; Gutfleisch, O.; Kentgens, A. P. M.; de Jong, K. P.; de Jongh, P. E. Confinement of $NaAlH_4$ in Nanoporous Carbon: Impact on H_2 Release, Reversibility, and Thermodynamics. *J. Phys. Chem. C* **2010**, *114*, 4675–4682.

[58] Adelhelm, P.; Gao, J.; Verkuijlen, M. H. W.; Rongeat, C.; Herrich, M.; van Bentum, P. J. M.; Gutfleisch, O.; Kentgens, A. P. M.; de Jong, K. P.; de Jongh, P. E. Comprehensive Study of Melt Infiltration for the Synthesis of $NaAlH_4$/C Nanocomposites. *Chem. Mater.* **2010**, *22*, 2233–2238.

[59] Liu, X.; Peaslee, D.; Majzoub, E. H. Tailoring the Hydrogen Storage Properties of $Li_4BN_3H_{10}$ by Confinement into Highly Ordered Nanoporous Carbon. *J. Mater. Chem. A* **2013**, *1*, 3926–3931.

[60] Kresge, C. T.; Leonowicz, M. E.; Roth, W. J.; Vartuli, J. C.; Beck, J. S. Ordered Mesoporous Molecular Sieves Synthesized by a Liquid-Crystal Template Mechanism. *Nature* **1992**, *359*, 710–712.

[61] Beck, J. S.; Vartuli, J. C.; Roth, W. J.; Leonowicz, M. E.; Kresge, C. T.; Schmitt, K. D.; Chu, C. T. W.; Olson, D. H.; Sheppard, E. W.; McCullen, S. B.; et al. A New Family of Mesoporous Molecular Sieves Prepared with Liquid Crystal Templates. *J. Am. Chem. Soc.* **1992**, *114*, 10834–10843.

[62] Huo, Q.; Margolese, D. I.; Ciesla, U.; Feng, P.; Gier, T. E.; Sieger, P.; Leon, R.; Petroff, P. M.; Schüth, F.; Stucky, G. D. Generalized Synthesis of Periodic Surfactant/Inorganic Composite Materials. *Nature* **1994**, *368*, 317–321.

[63] Firouzi, A.; Atef, F.; Oertli, A. G.; Stucky, G. D.; Chmelka, B. F. Alkaline Lyotropic Silicate−Surfactant Liquid Crystals. *J. Am. Chem. Soc.* **1997**, *119*, 3596–3610.

[64] Lehn, J.-M. Perspectives in Supramolecular Chemistry—From Molecular Recognition Towards Molecular Information Processing and Self-Organization. *Angew. Chem. Int. Ed. Engl.* **1990**, *29*, 1304–1319.

[65] Zhao, D.; Feng, J.; Huo, Q.; Melosh, N.; Fredrickson, G. H.; Chmelka, B. F.; Stucky, G. D. Triblock Copolymer Syntheses of Mesoporous Silica with Periodic 50 to 300 Angstrom Pores. *Science* **1998**, *279*, 548–552.

[66] Meng, Y.; Gu, D.; Zhang, F.; Shi, Y.; Cheng, L.; Feng, D.; Wu, Z.; Chen, Z.; Wan, Y.; Stein, A.; et al. A Family of Highly Ordered Mesoporous Polymer Resin and Carbon Structures from Organic–Organic Self-Assembly. *Chem. Mater.* **2006**, *18*, 4447–4464.

[67] Liu, R.; Shi, Y.; Wan, Y.; Meng, Y.; Zhang, F.; Gu, D.; Chen, Z.; Tu, B.; Zhao, D. Triconstituent Co-Assembly to Ordered Mesostructured Polymer–Silica and Carbon–Silica Nanocomposites and Large-Pore Mesoporous Carbons with High Surface Areas. *J. Am. Chem. Soc.* **2006**, *128*, 11652–11662.

[68] Song, Y.; Li, L.; Wang, Y.; Wang, C.; Guo, Z.; Xia, Y. Nitrogen-Doped Ordered Mesoporous Carbon with a High Surface Area, Synthesized through Organic-Inorganic Coassembly, and Its Application in Supercapacitors. *ChemPhysChem* **2014**, *15*, 2084–2093.

[69] Wei, J.; Zhou, D.; Sun, Z.; Deng, Y.; Xia, Y.; Zhao, D. A Controllable Synthesis of Rich Nitrogen-Doped Ordered Mesoporous Carbon for CO_2 Capture and Supercapacitors. *Adv. Funct. Mater.* **2013**, *23*, 2322–2328.

[70] Zhai, X.; Song, Y.; Liu, J.; Li, P.; Zhong, M.; Ma, C.; Wang, H.; Guo, Q.; Zhi, L. In-Situ Preparation of Boron-Doped Carbons with Ordered Mesopores and Enhanced Electrochemical Properties in Supercapacitors. *J. Electrochem. Soc.* **2012**, *159*, E177–E182.

[71] Jun, S.; Joo, S. H.; Ryoo, R.; Kruk, M.; Jaroniec, M.; Liu, Z.; Ohsuna, T.; Terasaki, O. Synthesis of New, Nanoporous Carbon with Hexagonally Ordered Mesostructure. *J. Am. Chem. Soc.* **2000**, *122*, 10712–10713.

[72] Joo, S. H.; Choi, S. J.; Oh, I.; Kwak, J.; Liu, Z.; Terasaki, O.; Ryoo, R. Ordered Nanoporous Arrays of Carbon Supporting High Dispersions of Platinum Nanoparticles. *Nature* **2001**, *412*, 169–172.

[73] Vinu, A.; Ariga, K.; Mori, T.; Nakanishi, T.; Hishita, S.; Golberg, D.; Bando, Y. Preparation and Characterization of Well-Ordered Hexagonal Mesoporous Carbon Nitride. *Adv. Mater.* **2005**, *17*, 1648–1652.

[74] Vinu, A. Two-Dimensional Hexagonally-Ordered Mesoporous Carbon Nitrides with Tunable Pore Diameter, Surface Area and Nitrogen Content. *Adv. Funct. Mater.* **2008**, *18*, 816–827.

[75] Wang, D.-W.; Li, F.; Chen, Z.-G.; Lu, G. Q.; Cheng, H.-M. Synthesis and Electrochemical Property of Boron-Doped Mesoporous Carbon in Supercapacitor. *Chem. Mater.* **2008**, *20*, 7195–7200.

[76] Bo, X.; Guo, L. Ordered Mesoporous Boron-Doped Carbons as Metal-Free Electrocatalysts for the Oxygen Reduction Reaction in Alkaline Solution. *Phys. Chem. Chem. Phys.* **2013**, *15*, 2459–2465.

[77] Brinks, H. W.; Hauback, B. C.; Srinivasan, S. S.; Jensen, C. M. Synchrotron X-Ray Studies of $Al_{1-y}Ti_y$ Formation and Re-Hydriding Inhibition in Ti-Enhanced $NaAlH_4$. *J. Phys. Chem. B* **2005**, *109*, 15780–15785.

[78] Fichtner, M. Properties of Nanoscale Metal Hydrides. *Nanotechnology* **2009**, *20*, 204009.

[79] Vajo, J. J. Influence of Nano-Confinement on the Thermodynamics and Dehydrogenation Kinetics of Metal Hydrides. *Curr. Opin. Solid State Mater. Sci.* **2011**, *15*, 52–61.

[80] Mason, T.; Majzoub, E. H. Effects of a Carbon Surface Environment on the Decomposition Properties of Nanoparticle $LiBH_4$: A First-Principles Study. *J. Phys. Chem. C* **2014**, *118*, 8852–8858.

[81] Brinker, C. J.; Lu, Y.; Sellinger, A.; Fan, H. Evaporation-Induced Self-Assembly: Nanostructures Made Easy. *Adv. Mater.* **1999**, *11*, 579–585.

[82] Nagarajan, R. Amphiphilic Surfactants and Amphiphilic Polymers: Principles of Molecular Assembly. In *Amphiphiles: Molecular Assembly and Applications*; Nagarajan, R., Ed.; American Chemical Society: Washington, DC, 2011; Vol. 1070, pp 1–22.

[83] Wang, Y.; Wang, X.; Antonietti, M.; Zhang, Y. Facile One-Pot Synthesis of Nanoporous Carbon Nitride Solids by Using Soft Templates. *ChemSusChem* **2010**, *3*, 435–439.

[84] Kruk, M.; Jaroniec, M.; Ko, C. H.; Ryoo, R. Characterization of the Porous Structure of SBA-15. *Chem. Mater.* **2000**, *12*, 1961–1968.

[85] Lu, A.-H.; Schüth, F. Nanocasting: A Versatile Strategy for Creating Nanostructured Porous Materials. *Adv. Mater.* **2006**, *18*, 1793–1805.

[86] Embs, J. P.; Juranyi, F.; Hempelmann, R. Introduction to Quasielastic Neutron Scattering. *Z. Phys. Chem.* **2010**, *224*, 5–32.

[87] Liu, X.; Majzoub, E. H.; Stavila, V.; Bhakta, R. K.; Allendorf, M. D.; Shane, D. T.; Conradi, M. S.; Verdal, N.; Udovic, T. J.; Hwang, S.-J. Probing the Unusual Anion Mobility of $LiBH_4$ Confined in Highly Ordered Nanoporous Carbon Frameworks via Solid State NMR and Quasielastic Neutron Scattering. *J. Mater. Chem. A* **2013**, *1*, 9935–9941.

[88] Verdal, N.; Udovic, T. J.; Rush, J. J.; Liu, X.; Majzoub, E. H.; Vajo, J. J.; Gross, A. F. Dynamical Perturbations of Tetrahydroborate Anions in $LiBH_4$ due to Nanoconfinement in Controlled-Pore Carbon Scaffolds. *J. Phys. Chem. C* **2013**, *117*, 17983–17995.

[89] Remhof, A.; Mauron, P.; Züttel, A.; Embs, J. P.; Łodziana, Z.; Ramirez-Cuesta, A. J.; Ngene, P.; de Jongh, P. Hydrogen Dynamics in Nanoconfined Lithiumborohydride. *J. Phys. Chem. C* **2013**, *117*, 3789–3798.

[90] Suwarno; Ngene, P.; Nale, A.; Eggenhuisen, T. M.; Oschatz, M.; Embs, J. P.; Remhof, A.; de Jongh, P. E. Confinement Effects for Lithium Borohydride: Comparing Silica and Carbon Scaffolds. *J. Phys. Chem. C* **2017**, *121*, 4197–4205.

[91] Carr, C. L.; Majzoub, E. H. Surface-Functionalized Nanoporous Carbons for Kinetically Stabilized Complex Hydrides through Lewis Acid–Lewis Base Chemistry. *J. Phys. Chem. C* **2016**, *120*, 11426–11432.

[92] Udovic, T. J.; Brown, C. M.; Leão, J. B.; Brand, P. C.; Jiggetts, R. D.; Zeitoun, R.; Pierce, T. A.; Peral, I.; Copley, J. R. D.; Huang, Q.; et al. The Design of a Bismuth-Based Auxiliary Filter for the Removal of Spurious Background Scattering Associated with Filter-Analyzer Neutron Spectrometers. *Nucl. Instrum. Methods A* **2008**, *588*, 406–413.

[93] Meyer, A.; Dimeo, R. M.; Gehring, P. M.; Neumann, D. A. The High-Flux Backscattering Spectrometer at the NIST Center for Neutron Research. *Rev. Sci. Instrum.* **2003**, *74*, 2759–2777.

[94] Copley, J. R. D.; Cook, J. C. The Disk Chopper Spectrometer at NIST: A New Instrument for Quasielastic Neutron Scattering Studies. *Chem. Phys.* **2003**, *292*, 477– 485.

[95] Azuah, R. T.; Kneller, L. R.; Qiu, Y.; Tregenna-Piggott, P. L.; Brown, C. M.; Copley, J. R.; Dimeo, R. M. DAVE: A Comprehensive Software Suite for the Reduction, Visualization, and Analysis of Low Energy Neutron Spectroscopic Data. *J. Res. Natl. Inst. Stand. Technol.* **2009**, *114*, 341–358.

[96] Paul, R. L.; Şahin, D.; Cook, J. C.; Brocker, C.; Lindstrom, R. M.; O'Kelly, D. J. NGD Cold-Neutron Prompt Gamma-Ray Activation Analysis Spectrometer at NIST. *J. Radioanal. Nucl. Chem.* **2015**, *304*, 189–193.

[97] Mitchell, P. C. H.; Ramirez-Cuesta, A. J.; Parker, S. F.; Tomkinson, J. Inelastic Neutron Scattering in Spectroscopic Studies of Hydrogen on Carbon-Supported Catalysts-Experimental Spectra and Computed Spectra of Model Systems. *J. Mol. Struct.* **2003**, *651-653*, 781–785.

[98] Hoang, K.; Van de Walle, C. G. Mechanism for the Decomposition of Lithium Borohydride. *Int. J. Hydrogen Energy* **2012**, *37*, 5825–5832.

[99] Lohstroh, W.; Fichtner, M. Rate Limiting Steps of the Phase Transformations in Ti-Doped $NaAlH_4$ Investigated by Isotope Exchange. *Phys. Rev. B* **2007**, *75*, 184106.

[100] Borgschulte, A.; Züttel, A.; Hug, P.; Barkhordarian, G.; Eigen, N.; Dornheim, M.; Bormann, R.; Ramirez-Cuesta, A. J. Hydrogen–deuterium Exchange Experiments to Probe the Decomposition Reaction of Sodium Alanate. *Phys. Chem. Chem. Phys.* **2008**, *10*, 4045–4055.

[101] Michel, K. J.; Ozoliņš, V. Native Defect Concentrations in $NaAlH_4$ and Na_3AlH_6. *J. Phys. Chem. C* **2011**, *115*, 21443–21453.

[102] Michel, K. J.; Ozoliņš, V. Vacancy Diffusion in $NaAlH_4$ and Na_3AlH_6. *J. Phys. Chem. C* **2011**, *115*, 21465–21472.

[103] Sorte, E. G.; Bowman, R. C.; Majzoub, E. H.; Verkuijlen, M. H. W.; Udovic, T. J.; Conradi, M. S. Mobile Species in $NaAlH_4$. *J. Phys. Chem. C* **2013**, *117*, 8105–8113.

[104] Ivancic, T. M.; Hwang, S.-J.; Bowman, R. C.; Birkmire, D. S.; Jensen, C. M.; Udovic, T. J.; Conradi, M. S. Discovery of A New Al Species in Hydrogen Reactions of $NaAlH_4$. *J. Phys. Chem. Lett.* **2010**, *1*, 2412–2416.

[105] Sorte, E. G.; Majzoub, E. H.; Ellis-Caleo, T.; Hammann, B. A.; Wang, G.; Zhao, D.; Bowman, R. C.; Conradi, M. S. Effects of NaOH in Solid NaH: Solution/Segregation Phase Transition and Diffusion Acceleration. *J. Phys. Chem. C* **2013**, *117*, 23575–23581.

[106] Wang, G.; Carr, C. L.; Zhao, D.; Sorte, E. G.; Ellis-Caleo, T.; Conradi, M. S.; Bowman, R. C.; Majzoub, E. H. Density Functional Theory of MH–MOH Solid Solubility (M = Alkali) and Experiments in NaH–NaOH. *J. Phys. Chem. C* **2015**, *119*, 8062–8069.

[107] Mikheeva, V.; Shkrabkina, M. Solid Solutions in NaOH-NaH and KOH-KH Systems. *Russ. J. Inorg. Chem.* **1962**, 7, 1251−1255.

[108] Toby, B. H. EXPGUI, a Graphical User Interface for GSAS. *J. Appl. Crystallogr*. **2001**, 34, 210−213.

[109] Larson, A.; Von Dreele, R. *General Structure Analysis System (GSAS)*; Los Alamos National Laboratory Report LAUR; Los Alamos National Laboratory: Los Alamos, NM, 2004; pp 86−748.

VITA

Christopher Lee Carr was born and raised in Massachusetts. In May 2012 he graduated *Magna Cum Laude* from Southern Illinois University Edwardsville with a Bachelor of Science degree in Physics. For his graduate studies, Christopher attended the University of Missouri St. Louis, where in May 2014 he received a Master of Science degree in Physics. Christopher received a Ph.D. in Physics, awarded jointly by Missouri University of Science and Technology and the University of Missouri St. Louis in May 2018.

While pursing his graduate degrees, Christopher was the co-author of 3 peer-reviewed journal articles on metal hydride based hydrogen storage research. He presented "Surface-Functionalized Nanoporous Carbons for Kinetically Stabilized Complex Hydrides through Lewis Acid-Lewis Base Chemistry" at the TMS 146th Annual Meeting 2017 in San Diego, California. Christopher was awarded fellowships from the NASA Missouri Space Grant Consortium, and the NSF Integrative Graduate Education Research Traineeship.